Fabrication and Characterization of Nanostructures from Self-assembled Block Copolymers

By

Joy Cheng

M.S., Chemistry (1998)
National Taiwan University

B.S., Chemistry (1996)
National Taiwan University

Submitted to the Department of Materials Science and Engineering in Partial Fulfillment of the Requirement for the Degree of

Doctor of Philosophy in Materials Science and Engineering

at the
Massachusetts Institute of Technology

June 2003

© 2003 Massachusetts Institute of Technology
All rights reserved

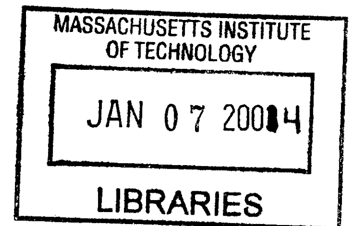

Signature of Author....................................
Department of Materials Science and Engineering
May 2, 2003

Certified by.......................................
Caroline A. Ross
Associate Professor of Materials Science and Engineering
Thesis Supervisor

Accepted by..
Harry L. Tuller
Professor of Ceramics and Electronic Materials
Chair, Department Committee on Graduate Student

ARCHIVES

Fabrication and Characterization of Nanostructures from Self-assembled Block Copolymers

by

Joy Cheng

Submitted to the Department of Materials Science and Engineering
On May 2, 2003 in Partial Fulfillment of the Requirement for the
Degree of Doctor of Philosophy in Materials Science and Engineering

ABSTRACT

Nanoscale magnetic dot arrays have attracted considerable interest, both for fundamental studies of micromagnetism and for possible applications in high-density magnetic data storage. Self-assembled block copolymers provide an alternative nanolithography technique to fabricate large-area nanomagnet arrays. Block copolymer thin films that micro-phase separate into periodic domains can be used as templates to define arrays of close-packed nanostructure, using a series of etching steps. Using polystyrene-polyferrocenyldimethyl- silane (PS-PFS), large-area polymer dots, silica dots and magnetic dots with periods of 56 nm were made using a series of plasma etching steps. Magnetometry techniques are used to characterize the bulk magnetic behavior of the dot arrays of Co, NiFe and pseudo spin valve structures. These dot arrays show strong magnetostatic interaction between the dots and within the dots.

The self-assembly process is simple and low cost, however, the block copolymers typically have uncontrolled defects and lack long-range order. A topographically patterned substrate is used to guide the phase-separation in a subsequently deposited block copolymer film. The lateral dimensions of the patterns in the substrates, and interfacial interactions, are key factors in the ordering mechanism. Well-ordered block copolymer structures can be achieved under proper confinement conditions. In addition, the position of the polymer microdomains and defects in the array such as dislocations can be purposefully controlled by the design of the topographical guiding features. Combining topographic confinement with block copolymer lithographic methods will enable large-area ordered functional dot arrays to be made for various applications.

Thesis Supervisor: Caroline A. Ross
Title: Associate Professor of Materials Science and Engineering

TABLE OF CONTENTS

1 INTRODUCTION 11

1.1 Overview.. 11
1.2 Patterned Media for High-Density Magnetic Data Storage....................... 12
1.3 Magnetic Properties of Particle Arrays... 15
1.4 Self-assembled Block Copolymers... 17
1.5 Templated Self-assembly.. 20
1.6 Contents.. 22

2 MATERIALS AND EXPERIMENTAL METHODS.................................25

2.1 Block Copolymer Templates..25
2.1.1 Block copolymers as Lithographic Templates....................................25
2.1.2 PFS Homopolymer and PFS-containing Block Copolymers.......................27
2.1.3 PFS-containing Block Copolymers as Lithographic Templates....................29
2.1.4 Preparation of PS-PFS Block Copolymer Thin Films..............................31
2.2 Pattern Transfer Techniques...35
2.2.1 Plasma Process..35
2.2.2 Pattern Transfer Process and Conditions – Reactive Ion etching.................36
2.2.3 Ion-beam Etching for Patterning Magnetic Materials...............................39
2.3 Fabrication of Topographical Substrates..41
2.4 Magnetic Characterization...44
2.4.1 Vibrating sample magnetometer (VSM)...44
2.4.2 Alternating Gradient Magnetometer (AGM)..45
2.4.3 Sweep-rate Dependent Coercivity..46
2.4.4 ΔM Plots...47

3 FABRICATION OF MAGNETIC PARTICLE ARRAYS USING BLOCK COPOLYMER LITHOGRAPHY.. 51

3.1 Etching PS-PFS Thin Films in Oxygen Plasma.....................................52
3.2 Pattern Transfer from Block Copolymer Masks to Tungsten Hard Masks... 57

3.3 Ion-Beam Etching Process for Patterning Magnetic Thin Films..............61

4 PROPERTIES OF MAGNETIC DOT ARRAYS.....................................67

4.1 Magnetic Dot Arrays from Block Copolymer Lithography....................67
4.2 Hysteresis Loops of Single-layer Dot Arrays....................................69
4.3 Scan-rate dependent Hysteresis of Single-layer Dot Arrays....................74
4.4 Magnetic Behavior of Two-layer Dot Arrays....................................77

5 TEMPLATED SELF-ASSEMBLY OF BLOCK COPOLYMERS ---USING TOPOGRAPHICAL TEMPLATES.......................................83

5.1 Templated Self-assembly of Block Copolymers....................................84
5.2 Block Copolymers on a Flat Surface..85
5.3 Block Copolymers on a Grooved Substrates......................................88
5.3.1 Annealing of Block Copolymers on Grating Substrates...........................88
5.3.2 SF 91/21 Thin Films in the Grooves...89
5.3.3 SF 32/10 Thin Films in the Grooves...92
5.4 Analysis of Ordered Block Copolymer Thin Films in Grooves....................96
5.4.1 Topographically-induced Ordering of Block Copolymer Thin Films..............96
5.4.2 Defect Formation in Block Copolymer Arrays.......................................99

6 CONCLUSIONS AND FUTURE WORKS.......................................105

6.1 Conclusions...105
6.2 Future Works...106

LIST OF FIGURES

1. INTRODUCTION

Figure 1.1 Conventional thin film magnetic recording media and patterned media..........13
Figure 1.2 Fabrication steps for making patterned media lithographically....................14
Figure 1.3 Energy of an isolated Stoner-Wohlfarth particle..15
Figure 1.4 Morphologies of PS-PI diblock copolymers..18
Figure 1.5 Orientation of PS-PMMA lamellar thin film at two wetting conditions...........19

2. MATERIALS AND EXPERIMENTAL METHODS

Figure 2.1 Chemical structure of polyferrocenyldimethylsilane (PFS)..........................22
Figure 2.2 Chemical structure of PS-PFS block copolymer.......................................23
Figure 2.3 Phase diagram of PS-PFS copolymers..24
Figure 2.4 AFM images of morphologies of IF 36/12 thin film of different thickness........25
Figure 2.5 Schematic of the arrangement of the polymer chains in polymer thin film........32
Figure 2.6 SEM micrographs of a 42 nm thick SF 32/10 thin film on silica substrate.........33
Figure 2.7 SEM micrographs of a 48 nm thick SF 32/10 thin film on silica substrate.........34
Figure 2.8 Basic mechanisms for plasma etching...36
Figure 2.9 Multilayers for pattern transfer from block copolymer to magnetic layer.........37
Figure 2.10 Interference lithography and Lloyd's mirror set up..................................42
Figure 2.11 SEM micrographs of Fabrication of grating substrates..............................43
Figure 2.12 Schematics of VSM and AGM..44
Figure 2.13 Scan-rate (pulse width) dependent coercivity..46
Figure 2.14 ΔM deviations of α-Fe metal particles at different packings........................48

3. FABRICATION OF MAGNETIC PARTICLE ARRAYS USING BLOCK COPOLYMER LITHOGRAPHY

Figure 3.1 Structure of PS-PFS thin film before / after O_2-RIE.................................52
Figure 3.2 XPS spectrum of PFS homopolymer thin film before and after O_2-RIE process.53
Figure 3.3 Index of refraction of polymers vs. O_2-RIE etching time............................54
Figure 3.4 SEM micrographs of O_2-RIE etched PS-PFS copolymers...........................56
Figure 3.5 Fabrication process of the Co dot array using block copolymer lithography......58
Figure 3.6 SEM micrographs of the intermediate stages of lithographic processing..........59
Figure 3.7 The saturation magnetization (Ms) vs. ion-beam etching time......................62
Figure 3.8 SEM micrographs of the W-capped Co dot array made by ion-beam etching.....62
Figure 3.9 In-plane coercivity and remaining magnetization in ion-beam etching process...63
Figure 3.10 SEM micrographs of NiFe dots and PSV dots....................................... 64

4. PROPERTIES OF MAGNETIC DOT ARRAYS

Figure 4.1 SEM cross-section micrographs of Co dot arrays....68
Figure 4.2 The in-plane hysteresis loops of single-layer Co and NiFe arrays....69
Figure 4.3 SEM micrographs and aspect ratio /size distribution of the Co dots....70
Figure 4.4 The switching field distribution of single-layer Co and NiFe arrays....72
Figure 4.5 Switching field distribution, coercivity and interaction field of dot arrays....72
Figure 4.6 ΔM plots of 5 nm thick and 15 nm thick Co arrays....73
Figure 4.7 Scan-rate dependent coercivity of Co and NiFe arrays....75
Figure 4.8 Switching volume and physical volume of the Co and NiFe arrays....76
Figure 4.9 The energy barrier, of Co and NiFe arrays....76
Figure 4.10 Schematic and SEM micrographs of PSV dots....77
Figure 4.11 Hysteresis loop of unpatterned and patterned PSV film....78
Figure 4.12 Scan-rate dependent coercivity of PSV dot arrays....79
Figure 4.13 GMR curve of PSV dot arrays....80

5 TEMPLATED SELF-ASSEMBLY OF BLOCK COPOLYMERS

Figure 5.1 Schematic of the arrangement of the polymer chains in polymer thin film....85
Figure 5.2 Plan-view SEM micrographs for SF91/21 and SF33/10....86
Figure 5.3 Pair distribution function of SF 91/21 and SF 32/10....86
Figure 5.4 SEM micrographs of PS/PFS 32/10 polymer films on patterned substrates....89
Figure 5.5 SEM micrographs of SF 91/21 films in various grooves....91
Figure 5.6 Schematic of the polymer chains of SF 91/21 near sidewalls....92
Figure 5.7 SEM micrographs SF 32/10 films in various grooves....93
Figure 5.8 SEM micrographs of ordered polymer and ordered silica nanostructures....94
Figure 5.9 SF 32/10 in a groove: SEM, schematic and quantized row in a groove....97
Figure 5.10 SF 32/10 in a groove: row spacing and size distribution....99
Figure 5.11. SF 32/10 in a groove: point defect and dislocation generation....101

Acknowledgements

Over the past five years, there are too many to thank. First, I thank my advisor, professor Caroline Ross. You have given me the perfect balance between guidance and freedom and allowed me to pursue research into the direction that interested me most. Through your mentoring, I have become a better and more independent researcher. Without your unlimited support and patience, this work would have been impossible.

An enormous amount of credit belongs to my thesis committee members, professor Caroline Ross, professor Henry (Hank) Smith and professor Edwin (Ned) Thomas. This committee provided a perfect blending of magnetism, lithography and polymers and fostered conversation among these fields. To Caroline, thank you for bringing a layman like me into the magic world of magnetism. To Hank, thank you for sharing your enthusiasm and vision of nanofabrication. To Ned, thank you for your insightful opinions, boundless imagination and all your help on the polymers. It's been an eye-opening experience for me to work with such amazing thesis committee members and I truly appreciate your inputs and encouragements over these years.

I have been fortunate to be a member in Professor Ross' group because this group is gentle and fun. Many thanks to Maya Farhoud, Minha Hwang, Doug Twisselmann, Mitsuhiro Shima, Yaowu Hao, Fernando Castano, Zil Lyons, Temar Tepper, Wonjoon Jung, Pete Chamber and Gabrielle Joseph for sharing your experience and life with me. You made learning about magnetism and fabrications more interesting and enjoyable. I have learned many things about the electron spin, magnetization reversal as well as things about kindness, patience and persistence.

During the course of my Ph. D., I had privilege of working closely with students and staffs in Professor Thomas' group and NanoStructure Lab (NSL). Many thanks to Vanessa Chan, Choelmin Park, Tao Deng and Sam Ha for teaching me the ABC of polymer science and working on various projects together with me. I want to thank Mike Walsh, Tim Savas, Jimmy Carter, Jim Daley and Mark Mondol in NSL for sharing your extensive knowledge and expertise about the fabrications. ☺

I have been grateful to Professor Julius Vancso at University Twente whose many members of his research group generously synthesized all the ferrocenylsilane homopolymers and block copolymers used in this dissertation. Specially, I would like to thank Rob Lammertink, Mark Hempenius & Igor Korczagin for their synthetic prowess.

I am indebted to all the people who have been a part of my scientific development. I can only name a few here. I would like to thank Professor Chung-Yuan Mou in Chemistry department at National Taiwan University for showing me an enchanting world of physics and chemistry and teaching me to appreciate the nature in a scientific way. I am thankful to Dr. Ta-Chau Chang in Institute of Atoms and Molecules, Taiwan, for introducing me to the lab and fascinating research world eleven years ago.

I have been fortunate to be surround by great friends and elders. Ching-Ying, Hong-Ren, Jung-Sheng, Big brother, Jessica, Fumei, Jason, pastor Chung and Mrs. Chung. Thank you for accepting me as what I am and riding with me through the ups and the downs.

I am thankful for being in a wonderful family. I am eternally grateful to Dad and Mom, for your unconditional and everlasting care and love. Being your daughter is the best gift I can ever think of. Thank you for always being there for me. For my husband, Francis, thank you for being my best friend and best buddy in my life. Finally, I would like to thank God, the creator of atoms, molecules, the earth, and universe, for all the nature wonders, great mentors, friends and family.

Oh Lord my God when I in awesome wonder
Consider all the worlds thy hands have made
I see the stars, I hear the rolling thunder
Thy power throughout the universe displayed
Then sings my soul, my Savior God, to Thee,
"How great Thou art, how great Thou art."

From "How great Thou art"
by Carl Boberg in Swedish, in 1886
translated by Stuart Hine in 1933

Chapter 1

INTRODUCTION

1.1 Overview

Due to the miniaturization of electronic, optoelectronic and magnetic devices, nanometer-scale patterning of materials at low cost is an important objective of current science and technology. Electronic circuits often require the fabrication of intricate, complicated structures, but it is sufficient to simple, repeating structures in many devices. Various applications of nanoscale periodic patterning include the fabrication of high-density magnetic recording devices[1-3], the synthesis of DNA electrophoresis media [4], and high-capacity capacitors [5]. One promising route for patterning simple nanostructures is the use of self-assembled systems.

Block copolymers are a prominent example of self-assembled materials as they form a large variety of well-ordered microdomain structures with molecular dimensions. Depending on the length and interaction of the different blocks, typical repeating distances range from 10 nm to 100 nm. In the past decade, thin films of block copolymers have attracted increasing interest in the area of nanotechnology. With suitable preparation, a thin film of a block copolymer can be converted into a self-organized template for fabricating various nanostructures with periodic order on the nanometer scale [6].

Much research has been done to fabricate nanoscale magnetic element arrays both for fundamental studies of micromagnetism and possible applications in high-density magnetic data storage as patterned media [2]. It would be interesting to combine self-assembly methods with the fabrication of nanoscale magnetic elements. This project started from the idea of making magnetic nanostructures using block copolymers as a self-organized lithographic template. Our ultimate goal is to develop a simple and low-cost route to fabricate large-area magnetic elements with long-range order and precise positions. Background information and possible schemes to achieve this goal are presented in this chapter. This chapter serves as a general introduction to the important topics, including patterned media, properties of magnetic nanostructures, block copolymers and process tools.

1.2 Patterned Media for High-Density Magnetic Data Storage

The areal density of hard disks has been increasing at 60% per year (10-fold in 5 years) since early 1990s, and lab demonstrations of 100 Gbits/in^2 were presented in 2002 [7]. Following this trend, the recording density will reach 500 Gbits/in^2 in three years. The increase of data density and data rate have generally been achieved by scaling to make the read-write head smaller, the medium thinner and higher in coercivity, and the head-medium spacing smaller. The performance of the medium is limited by noise originating from the granular microstructure of the thin film, so there has been a trend to decrease the grain size. However, this trend is limited by thermal instability (superparamagnetism) of the grains comprising the medium. If the grains are too small, thermal energy can change the magnetization of the grain, with consequent loss of the recorded signal. Superparamagnetism has been predicted to occur at a density of around 200 Gbits/in^2 and, therefore, considerable efforts have been made in improving thermal stability of recording medium and designing alternative methods for data storage. Patterned media is one of the potential methods to circumvent thermal instability and advance high-density data storage.

Magnetic thin films for current recording media are made of a polycrystalline alloy of Co, Cr, and Pt with additional B or Ta to enhance grain-boundary segregation of non-magnetic elements. Each ~ 10 nm diameter grain behaves like single-domain particle and is weakly exchange-coupled with other grains (Figure 1.1a). A bit cell containing one to two hundred grains is recorded by magnetizing these grains either parallel or anti-parallel to the track direction. Both minimizing bit size and keeping a reasonable signal to noise ratio require grain size reduction. Therefore, reducing the grain volume, V, is one of the key ingredients in scaling up data density. However, a typical design rule for a recording medium based on the criteria for 10 year thermal stability requires that the magnetic energy KV of the grain to be larger than 40 times the room-temperature thermal energy k_BT (where K is magnetic anisotropy, k_B is Boltzmann's constant and T is the temperature). Therefore, there is a lower limit for minimum grain size and this conventional scaling approach is limited in maximum data density by thermal instability [8].

Patterned magnetic media offers the possibility of higher data density than conventional media. For patterned media, the bit positions are lithographically defined and each bit is a single magnetic domain, with uniaxial magnetic anisotropy so that the magnetization points in one of only two directions at remanence, representing 1 bit of data (Figure 1.1b). Unlike continuous thin film media, the grains within a patterned element are coupled so that the entire element behaves as a single magnetic domain. In patterned media, very high densities

can be achieved because the thermal stability criteria now refer to the volume and anisotropy of the entire magnetic element, rather than the individual grains of which it is composed [1-3].

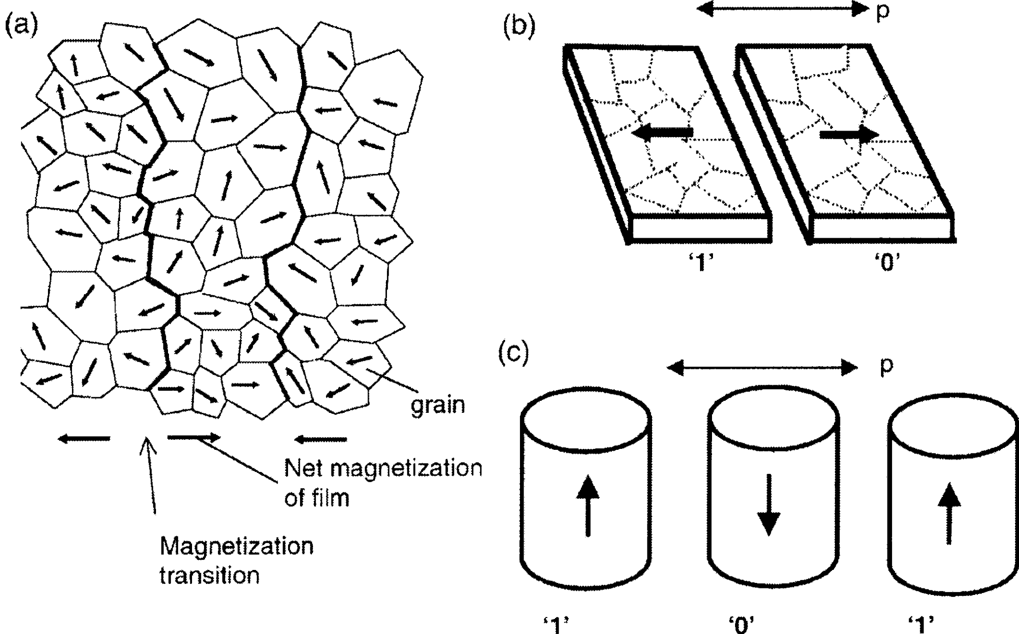

Figure 1.1 (a) Conventional thin film medium, consisting of exchange-decoupled grains. Bit cells are represented by the transitions between oppositely magnetized regions. (b) A patterned medium with in-plane magnetization. They can be polycrystalline or single crystal. (c) A patterned medium with perpendicular magnetization. Binary 1 and 0 are shown. [Ref 9]

Magnetic element arrays with deep submicron feature sizes are too small to fabricate using conventional optical lithography. Instead, a range of nanolithography techniques have been used to make prototype structures, including interference lithography [9], x-ray lithography [10] and nanoimprint lithography [11]. The pattern can be transferred to magnetic materials by an additive or subtractive process. In an additive process, magnetic material is deposited through a lithographically-defined template by electrodeposition or evaporation, followed by liftoff or removal of the template (figure 1.2a and figure 1.2b). In a subtractive process, a continuous thin film of magnetic material is deposited before patterning and then is etched to form discrete magnetic elements (Figure 1.2c).

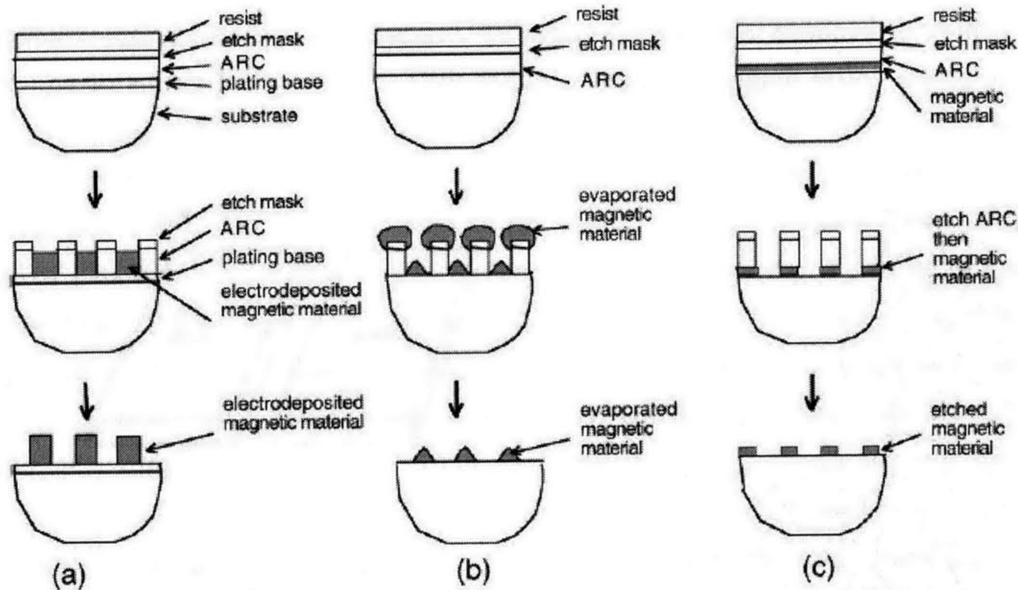

Figure 1.2 Fabrication steps for making patterned media lithographically. (a) A template of holes is prepared, and then magnetic material is electrodeposited into the holes. (b) A template of holes is prepared, and then magnetic material is evaporated on the template. The template is dissolved to leave an array of tapered particles. (c) A magnetic material is deposited, then a template of dots is prepared on top of the film to act as an etch mask. The exposed film is then removed by ion-beam etching. [Ref 9]

In addition to lithography techniques, several nonlithographic methods have been developed for making magnetic particle arrays. One example is the use of anodized alumina films as templates for electroplating of magnetic materials. The resulting aluminum oxide contains closed-packed pores with pore size and pore spacing controlled by the anodization conditions. Various magnetic nanowire arrays with period from 40 nm and above have been made by this method [12]. Magnetic nanoparticle arrays also can be made by chemical synthesis from solution. For instance, uniform 4-nm face-centered-tetragonal (fct) $Fe_{52}Pt_{48}$ nanocrystals form self-organized superlattice structures for magnetic recording media. The size and magnetic properties of these nanocrystals can be tuned by the chemical composition, process temperature and annealing time [13].

Compared with non-lithographic methods, which rely on various self-assembly mechanisms, magnetic particle arrays made using lithographic methods have better spatial control. At large scales (hundreds of nanometers), the lithographic process offers long-range order and the precise registry of magnetic dots, which are the key attributes to enable the recording head to address a single bit of the patterned media correctly. On the

other hand, in the sub-50 nm region, it becomes more difficult to make identical nanostructures by lithography. Ideally, in patterned media, each magnetic bit should behave in the same way. However, the variance in magnetic elements arising from the lithographic process leads to a distribution of magnetic properties and magnetic behavior. Instead, some self-assembled materials provide a route to produce particle arrays with very narrow size distribution, which is necessary for patterned media. Therefore, in this project we will try to combine the advantage of lithographic methods and self-assembly mechanisms to fabricate nanostructures with good long-range ordering and uniformity.

1.3 Magnetic Properties of Particle Arrays

There are two important volume parameters characterizing the magnetic particle array. One is the physical volume of a magnetic particle, V_P, and the other is the switching volume of the magnetic particle, V, which is the activated volume for describing magnetization reversal behavior. This section will discuss the thermal stability issue, the correlation between physical volume and switching volume of the magnetic particles and the measurement of switching volume and particle interaction in the arrays.

We first consider an assembly of isolated, non-interacting uniaxial single domain particles. Under this condition, the Stoner-Wohlfarth coherent rotation model [14] can be used to simplify the problem. Although it neglects coupling and nonuniform magnetization reversal, this model still gives good insight into thermal stability in the recording media.

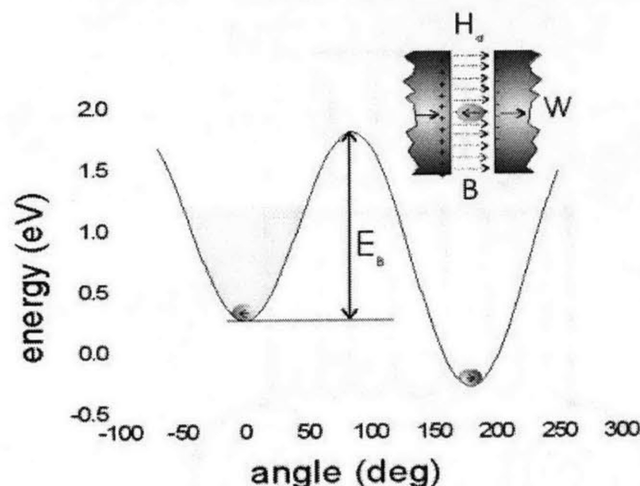

Figure 1.3 Energy of an isolated Stoner-Wohlfarth particle. [Ref 15]

Figure 1.3 shows the energy of an isolated elliptical Stoner-Wohlfarth particle with respect to the angle between the easy axis of the particle and the field. The energy barrier between the two stable states is field dependent,

$$E = V[K \sin^2 \theta + HMs \cos(\theta - \phi)]$$

The switching volume (V), magnetic anisotropy energy (K) and saturation magnetization (M_S) are the properties of particles, while θ and ϕ describe the orientation of particle with respect to the applied magnetic field (H). Switching volume (V) is the unit volume of magnetic moments that switch together in magnetization reversal and may be different from physical volume (V_p), the actual volume of the particle. The magnetic anisotropy energy (K) depends on the material, crystallography and shape of the magnetic particle. θ is the angle between magnetization and field direction and ϕ is the angle between the easy axis and magnetic field. The energy barrier is the difference between the maximum and minimum energy. The following expression gives the field-dependent energy barrier height,

$$E_B = KV(1 - \frac{H}{H_0})^{\frac{1}{n}} \ldots\{1\}$$

where H_0 is the anisotropy field (H_0=2xK/Ms) at which field the energy barrier is zero. From the above equation, one may see that the energy barrier is KV at zero applied field and the energy barrier decreases if there is a demagnetizing interaction among the particles. The geometric factors n and x are related to the spatial arrangement of magnetic particles. For instance, n = 0.5 and x = 1 if particles are isolated and the applied field is along the easy axis direction.

The thermal stability of a particle ensemble depends on the relative ratio of magnetic energy barrier and thermal energy. At finite temperatures, thermal fluctuations may act to assist in overcoming the reversal barrier, E_B. According to the Arrhenius-Neel model, the magnetization of the ensemble, M(t), decreases exponentially with time t:

$$M(t) = M(t = 0)e^{\frac{-t}{\tau}} \ldots\{2\}$$

where the relaxation time τ is related to the barrier energy E_B and thermal attempt frequency f_0:

$$\frac{1}{\tau} = f_0 e^{\frac{-E_B}{k_B T}} \ldots\{3\}$$

where the thermal attempt frequency f_0 sets the timescale for temperature-assisted decay. f_0 $=10^9$ is commonly used. Thus it becomes possible to define the superparamagnetic effect by arbitrarily letting the relaxation time τ =100 secs, which is roughly the time required to measure the remanence. No coercivity would be observed in a typical measurement if the relaxation time were less than 100 secs. Therefore, one obtains that if $E_B > 25\ k_B T$ the

system behaves ferromagnetically, and if $E_B < 25\ k_BT$ the system is superparamagnetic [16]. In magnetic data storage, the retained magnetization needs to last for a longer time. Charap defined a stable magnetic recording media as one which could hold 95% magnetization over 10 years [17] and the storage barrier requirement for thermal stability criterion is $E_B > 43\ k_BT$. In a hard disk, the presence of demagnetizing fields lowers the energy barrier and thus increases the required stability ratio to $E_B > 60\ k_BT$.

Assuming the switching volume equals the physical volume of the magnetic particle, the minimal stable isolated particle diameter, D_P, of 60 k_BT criterion, and the critical diameter for observing superparamagnetism in an isolated particle, D_S, can be roughly estimated for different magnetic materials. Table 1.1 lists the critical diameters for CoPtCr, Co and FePt particles.

Material	K_U (10^7erg/cm^3)	M_S (emu/cm^3)	D_P (60k_BT) (nm)	D_S (25k_BT) (nm)
$Co_{71}Cr_{17}Pt_{12}$	0.2	298	20.8	15.6
Co	0.45	1400	16	12
FePt	6.6-10	1140	5.6-6.6	4.2-5.0

(D_P and D_S values are derived without considering demagnetizing field.)

Table 1.1 Important parameters for CoPtCr, Co and FePt particles.

Assuming a 60 k_BT criterion, a square-packed Co particle system with 16 nm particle diameter and 32 nm spacing results in a density of 600 GParticle/in^2 and a FePt particle system with 6nm particle diameter and 12 nm spacing, gives a density of 4.2×10^{12} particle/in^2. Therefore, the high thermal stability of the grains in a discrete magnetic particle system raises the upper limit of data density considerably beyond that expected in conventional media.

1.4 Self-assembled Block Copolymers

Block copolymers consist of chemically distinct macromolecules covalently linked to form a single chain. The different blocks are frequently incompatible; owing to the mutual repulsion, the blocks tend to phase segregate into different microdomains. The spatial extent of the domains is limited by the constraint imposed by the chemical connectivity of

the blocks. Area minimization at the interface takes place due to high interfacial energy between two blocks. As a result of minimizing free energy, self-organization of a periodic structure occurs on the nanometric length scale. Depending on the length, connectivity, and mutual interaction of the different blocks, the microdomains can form as body-centered-cubic spheres, an ordered bicontinuous double diamond (or double gyroid) structure, hexagonally packed cylinders and alternating lamellae [18]. Figure 1.4 demonstrates various morphologies of polystyrene (PS) -*b*- polyisoprene (PI) block copolymers as a function of the volume fraction of polystyrene.

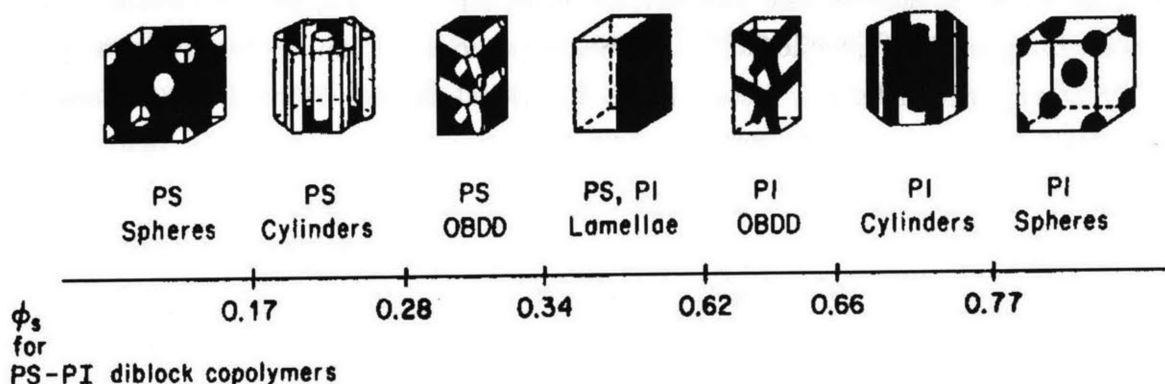

Figure 1.4 Morphologies of PS-PI diblock copolymers. [Ref 18]

The beauty of using block copolymers as the building blocks for nanostructures is that the domain size, period, symmetry and composition of block copolymers can be designed and experimentally controlled. In the bulk, the structures and properties of block copolymers are determined by molecular parameters including the overall degree of polymerization N, the volume fraction of A /B component, and the A-B segment-segment interaction (Flory-Huggins) parameter χ. The first two factors can be regulated through chemical synthesis and the interaction parameter is determined by the selection of the A-B monomer pair. The product $N\chi$ can be regarded as a measure of the degree of segregation. The strong segregation limit corresponds to $N\chi \gg 10$. In this region, microdomains of A and microdomains of B are well separated and the period for the microdomain scales as $N^{2/3}\chi^{1/6}$. The sizes and periods of these microdomain structures are governed by the chain dimensions and are typically on the order of tens of nm.

Many applications, including patterned media, require 2-D periodic nanostructures. Block copolymers spontaneously form repeating nanometer-scale patterns over a large area as well as 3-D structures in the bulk phase. In a thin film, the presence of a substrate and free surface introduces additional driving forces for structure formation and results in changes in domain dimensions or phase transitions due to preferential segregation of one block at the

substrate or surface [19]. Therefore, three important issues need to be considered for block copolymer thin films.

First, polymer films are sensitive to the surface. Polymer films with high interfacial energy and low viscosity quickly dewet from substrate surface and cannot form a uniform film with stable morphology. In order to have stable and uniform block copolymer thin film for subsequent lithography steps, surface compatibility between thin film and substrate is very important.

Second, the surface tension between substrate and each block of the polymer sets the boundary condition for microdomain orientation of the block copolymer [19,20]. Figure 1.5 shows two structures formed from a lamellar polystyrene (PS) -b- polymethylmethacrylate (PMMA) thin film due to different surface boundary conditions. PS is present at both at the air surface and the substrate in figure 1.5a. Figure 1.5b shows that nonpreferential boundary conditions can lead to perpendicular orientation of lamellae. Similar behaviors were observed in cylindrical block copolymers.

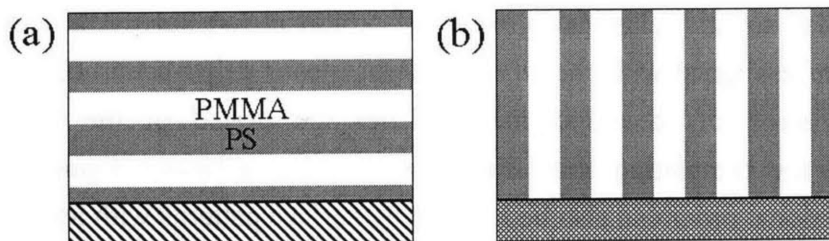

Figure 1.5 Orientation of PS-PMMA lamellar thin film at (a) preferential wetting, (b) non-preferential wetting condition.

Third, block copolymer thin films typically are less ordered than the bulk copolymers. However, long-range positional order and orientation of the microdomains is vital to many nanostructure applications. A block copolymer thin film is typically a "polycrystalline structure" consisting of randomly oriented polymer "grains". A grain is a region where microdomains form a structure with translational symmetry. The typical "grain size" or correlation length of an ordered region is in the order of hundreds of nanometers to a micron depending on the process conditions, surface interactions and the degree of polymerization N, and interaction parameter χ of block copolymers. Therefore, enhancing mobility of polymer molecules, reducing surface pinning [21] and extended thermal annealing time help to increase the grain size of a copolymer thin film [22].

1.5 Templated Self-assembly

Many practical applications require nanostructures with long-range positional order. For patterned magnetic media, precise positions of the magnetic dots are important so that the recording head can address every single bit. Self-assembled systems, by themselves, typically lack long-range order and contain a large population of uncontrolled defects. The nanostructures of block copolymer thin films typically are short-range ordered, randomly oriented and contain uncontrollable defects. There is therefore an interest in developing methods for making long-range ordered structures from these self-assembled systems.

There have been several attempts to guide self-assembly in order to create structures that otherwise would not spontaneously form. An electric fields have been used to guide the orientation of cylindrical block copolymers [23]. Mesoscopic silica can be oriented in channels using capillary force [24]. Directional solidification with a temperature gradient provides the control of the cylinder orientation of block copolymers [25]. In addition to controlling the orientation of the self-assembled system, spatial confinement or chemical surface patterns can be used to precisely control the positions of nanostructures. For example, similar to the classical growth of epitaxial crystal films, lamellar block copolymers can be aligned with chemically heterogeneous stripe-patterned substrates when the domain spacing of the copolymer matches the period of the substrates [26]. In graphoepitaxy, the templating thin film growth using substrate topographic features, long-range positional order can also be induced by surface patterns with length scales larger than the domain spacing or lattice parameter of the self-assembled system [27]. Well ordered crystals, liquid crystals, lamellar block copolymers have been achieve with this method [27,28]. Graphoepitaxy is of particular interest because such templated self-assembly makes it possible to control the locations of nanoscale features using considerably coarser substrate features, producing hierarchical structures. Patterned substrates have been employed to improve the in-plane order of PS-PVP (polyvinylpyridine) thin films to form "single crystal" nanostructures with very low defect levels over lengths of up to 5 μm [29].

Combining bottom-up process such as block copolymer lithography with top-down process templated self-assembly methods would allow nanostructures to be lithographically fabricated in precise positions on a substrate. In this thesis, we present a graphoepitaxy method for orienting self-assembled block copolymers using substrates patterned by interference lithography over areas of several cm^2. Ordered nanostructures of other materials can be made from an ordered block copolymer by pattern transfer. In this system, features within the templating pattern can deliberately introduce defects and dislocations in

the domain array. Studies of assembly in block copolymers templated by patterned substrates illustrate the power of the templating process in its ability to tailor the spacing of a self-assembled structure and to engineer the location of defects, which enables the design of precisely patterned hierarchical structures for a variety of applications.

1.6 Contents

The ultimate goal of this project is to develop a simple and low-cost method to fabricate large-area magnetic elements with long-range order and precise positions using self-assembled block copolymers. Each chapter in the thesis presents a part of our attempt to accomplish this goal.

Chapter 2 of this thesis covers the materials and experimental methods. This includes properties of PFS-containing block copolymers, pattern transfer techniques, fabrication of topographical substrates for templating self-assembly, and magnetic characterization tools and methods. Considerations regarding the use of block copolymers as templates are discussed. This chapter also describes the conditions for plasma etching in pattern transfer, using reactive-ion-etching and ion-beam etching. In addition, magnetometers and methods for studying magnetic particle arrays are explained in this chapter. The fabrication of magnetic nanostructures form block copolymers is described in chapter 3. A sphere-morphology PFS-PS thin film is converted to nanopillars using oxygen plasma under optimized conditions. Co, NiFe and pseudo-spin-valve dot arrays are made from polymer mask and the subsequent patterning of a silica/tungsten/magnetic stack. The ion-milling process is also optimized especially for patterning magnetic nanostrucutres. In chapter 4, magnetic characterization is performed on the magnetic dot arrays. The activation volumes and interparticle interaction of magnetic particles are interpreted form sweep-rate dependent coercivity and ΔM plots. Magnetic dot arrays with different volume and composition are compared. Although magnetic dot arrays can be successfully made using block copolymer lithography, these arrays contain many defects and lack long-range ordering, which is not desired for applications such as patterned media. Chapter 5 describes our work on controlling the self-assembled process using topographical templates. Block copolymers were confined laterally in grooved substrates and form well ordered structures. Detailed studies show that with proper topographical features, we can precisely control the position of each block copolymer microdomain and introduce defects purposefully into arrays. Finally, a conclusion and potential future works are presented in chapter 6.

Reference

1. R.L. White, R.M.H. New, R.F.W. Pease, *IEEE Trans. Magn.* 33, 990 (1997)
2. C. A. Ross, *Ann. Rev. Mater. Res.* **31**, 203 (2001)
3. S. Y.Chou, *Proc. IEEE* **85**, 652 (1997)
4. W. D. Volkmuth and R. H. Austin, *Nature* **358**, 600 (1992)
5. C. T. Black, K. W. Guarini,K. R. Milkove, S. M. Baker, T. P. Russell, M. T. Tuominene, *Appl. Phys. Lett.* **79**, 409 (2001); K. W. Guarini, C. T. Black, K. R. Milkove, R. L. Sandstrom, *J. Vac. Sci. Technol. B* **19**, 2784 (2001); K. W. Guarini, C. T. Black, Y. Zhang, H. Kim, E. M. Sikorski, I. V. Babich, *J. Vac. Sci. Technol. B* **20**, 2788 (2002)
6. M. Park, C. Harrison, P.M. Chaikin, R.A. Register, D.H. Adamson, *Science*, **276**, 1401 (1997)
7. Seagate website. http://www.seagate.com/newsinfo/technology/index.html
8. R.L. White, *J. Magnetism Magn. Mat.* **209**, 1 (2000)
9. T. Savas, M. Farhoud, H. I. Smith, M. Hwang, C. A. Ross, *J. Appl. Phys.* **85**, 6160, (1999); C. A. Ross, H. I. Smith, T. Savas, M. Schattenburg, M. Farhoud, M. Hwang, M. Walsh, M. Abraham, R. Ram, *J. Vac. Sci. Technol. B* **17**, 3168, (1999); M. Farhoud, J. Ferrera, A.J. Lochtefeld, T.E. Murphy, M.L. Schattenburg, J. Carter, C.A. Ross, H.I. Smith, *J. Vac. Sci. Technol. B* **17**, 3182, (1999)
10. F. Rousseaux, D. Decanini, F. Carcenac, E. Cambril, M.F. Ravet, C. Chappert, N. Bardou, B. Bartenlian, P. Veillet, *J. Vac. Sci. Technol. B* **13**, 2787, (1999)
11. W. Wu, B. Cui, X.Y. Sun, W. Zhang, L. Zhuang, L. S. Kong, S. Y. Chou, *J. Vac. Sci. Technol. B* **16**, 3825, (1998)
12. J. M. Garcia, A. Asenjo, J. Velazquez, D. Garcia, M. Vazquez, et al. *J. Appl. Phys.* **85**, 5480 (1999); R.M. Metzger, V.V. Konovalov, M. Sun, T. Xu, G. Zangari, et al. *IEEE Trans. Magn.* **36**, 30 (2000)
13. S. Sun, C. B. Murray, D. Waller, L. Folk, and A. Moser, *Science* **287**, 1989 (2000)
14. B. D. Cullity, *Introduction to magnetic materials*, 389-390 (1972)
15. D. Weller and A. Moser, *IEEE Trans. Magn.* **35,** 4423 (1999)
16. M. P. Sharrock, *IEEE Trans. Magn.* **35,** 4414 (1999)
17. S. H. Charap, P.L. Lu, Y. He, *IEEE Trans. Magn.* **33,** 978 (1997)
18. F. S. Bates and G. H. Fredrickson, *Annu. Rev. Phys. Chem.* **41**, 525 (1990)
19. M. J. Fasolka and A. M. Mayes, *Ann. Rev. Mater. Res.* **31**, 323 (2001)
20. E. Huang, S. Pruzinsky, T.P. Russell, J. Mays, C.J. Hawker, *Macromol.* **32**, 5299 (1999)

21. C. Harrison, P .M. Chaikin, D. A. Huse, R. A. Register D. H. Adamson, A. Daniel, E. Huanf, P. Mansky, T. P. Russell, C. J. Hawker, D. A. Egolf, I. V. Melnikov and E. Bodenschatz, *Macromol.* **33**, 857 (2000)
22. C. Harrison, D. H. Adamson, Z. Cheng, J. M. Sebastian, S. Sethuraman, D. A. Huse, R. A. Register and P .M. Chaikin, *Science* **290**, 1558 (2000)
23. T. L. Morkved, M. Lu, A. M. Urbas, E. E. Ehrichs, H. M. Jaeger, P. Mansky, T. P. Russell, *Science*, **273**, 931 (1996); T. Thurn-Albrecht, J. Schotter, G. A. Kastle, N. Emley, T. Shibauchi, L. Krusin-Elbaum, K. Guarini, C. T. Black, M. T. Tuominen, T. P. Russell, *Science*, **290**, 2126 (2000)
24. M. Trau, N. Yao, E. kim, Y. Xia, G. M. Whitesides, I. A. Aksay, *Nature* **390**, 674 (1997)
25. C. De Rosa, C. Park, E. L. Thomas, *Nature* **405**, 433 (2000)
26. L. Rockford, M. Mansky, T. P. Russell, M. Yoon, S. G. J. Mochrie, *Phys. Rev. Lett.* 82, 2602 (1999); R. D. Peters, X. M. Yang, P. F. Nealey, *Macromolecules.* **35**, 1822 (2002)
27. H. I. Smith, M. W. Geis, C.V. Thompson, H.A. Atwater, *J. Cryst. Growth* **63**, 527 (1983); T. Kobayashia, K. Takagi, *Appl. Phys. Letts*. **45** 44 (1984); D. C. Flanders, D. C. Shaver, H. I. Smith, *Appl. Phys. Lett*. **32**, 597 (1978)
28. P. Lambooy, T. P. Russell, G. J. Kellogg, A. M. Mayes, P. D. Gallagher, S. K. Satija, *Phys. Rev. Lett.* **72**, 2899 (1994); N. Koneripalli, N. Singh, R. Levicky, F. S. Bates, P. D. Gallagher, S. K. Satija, *Macromolecules.* **28**, 2897 (1995)
29. R. A. Segalman, H. Yokoyama, E. J. Kramer, *Adv. Mater.* **13**, 1152 (2001)

Chapter 2

MATERIALS AND EXPERIMENT METHODS

The self-organizing behavior and the periodic nanostructure of a block copolymer thin film make it ideal as a lithographic template to fabricate nanoscale magnetic particle arrays. This chapter covers basic concepts and background information regarding the fabrication and characterization of magnetic particle arrays made using block copolymers, including consideration of block copolymer templates, pattern transfer techniques, preparation of patterned substrates, and magnetic characterization. The block copolymer templates section includes the considerations of polymer templates and properties of PFS-containing block copolymers. Operation principles and conditions for plasma etching of polymeric materials, oxide, metal and magnetic thin films are discussed in the pattern transfer section. The third section of this chapter describes interference lithography and the fabrication of grating substrates that are used to guide the self-assembly process. Finally, the basic principles of magnetometers and characterization methods such as dynamic coercivity and ΔM plots are introduced in the magnetic characterization section.

2.1 Block Copolymer Templates

Comparing with other conventional nanolithographic, self-assembled block copolymers provide a simple method to make a nanoscale periodic structure. The challenge lies in how to create the lithographic templates from block copolymers effectively and efficiently. In addition to good surface compatibility and process stability of block copolymers, a simple and highly selective process is necessary to convert a flat block copolymer thin film into a template. This section describes the important considerations and provides background information for a block copolymer template, in addition to describing the properties of block copolymers we used in this project.

2.1.1 Block copolymers as Lithographic Templates

In general, the etch selectivity between two blocks depends on the polymer chemistry and etching method. Block copolymers such as PS (polystyrene) -PI (polyisoprene), PS-PB (polybutadiene), PS-PMMA (polymethylmethacrylate), PS-PVP (poly-2-vinylpyridine)

have been used as lithographic templates. Cylinder morphology and sphere morphology polymers are the most common for fabrication of nanostructure arrays because they form simple and periodic structures on a two-dimensional surface. A range of nanostructures including high-density Si dots, metal pillars and quantum dots have been created from these polymers since the late 1990s [1,2,5]. Selectively removing one block from the copolymer and leaving the other block on the surface is an essential step in utilizing block copolymers as templates.

Although the molecular structure is different for the blocks in organic-organic polymers, there is little removal selectivity within these block copolymers. Therefore, it is difficult to take off one block without damaging the structure of other block. In some cases, the selectivity can be enhanced by breaking the backbones of one block. In PS-PI and PS-PB block copolymers, ozone is used to remove PI and PB spheres by cutting the carbon-carbon double bonds in the polymer backbone. After ozone treatment and soaking the polymer film in water, the remaining polymer film contains regularly arranged holes [1]. Deep UV exposure degrades the PMMA domains and simultaneously cross-links the PS matrix in PS-PMMA thin films in which PMMA cylinders are perpendicular to the substrate. Then the degraded PMMA can be removed from the PS matrix using acetic acid [2]. However, these etch methods are complicated and require many steps.

On the contrary, plasma etching provides a simple way to obtain high selectivity and anisotropy. Most organic polymers etch quickly in an oxygen plasma because the hydrocarbon forms volatile species in an oxygen plasma and then are removed by the vacuum system of the plasma etching equipment. Loading inorganic components which are stable in the plasma or form nonvolatile oxide in an oxygen plasma enhances the plasma resistance of polymeric materials [3]. For example, a silylation process combined with chemically amplified resist is often used in top-surface imaging systems [4]. This is accomplished by irradiating the chemically amplified resist thin film to produce hydroxyl-containing film in selective areas and then reacting with a silylating agent (such as Me_2N-$SiMe_3$) to yield the corresponding silylether. The high oxygen-RIE etching selectivity between the organic polymer and the silylether leads to high contract in the resist. An inorganic component can also be loaded selectively into one block in the block copolymer system. For instance, in PS-PVP, gold particles were incorporated into the PVP spheres after loading and reduction reaction. The gold particles in the block copolymers become good resists in the plasma etching for patterning As/InGaAs/GaAs quantum dots and diamond dots [5].

To combine the benefits from self-assembled block copolymer with the high plasma resistance of an inorganic component, efforts have been made to synthesize inorganic-containing self-assembled block copolymers. Polyferrocenyldimethylsilane (PFS) (figure 2.1) is an organometallic polymer containing iron and silicon and offers good etch resistance to oxygen RIE [6]. A combination of an organic block and an organometallic block leads to very high etching selectivity (1:40) between the two blocks and made possible a one-step process to convert block copolymer thin films into topographical nanostructures [7]. Because there are many advantages associated with plasma etch process and inorganic–containing block copolymers, in this project, we will develop a fabrication scheme to make magnetic particle array based on PFS-containing block copolymers combined with plasma etching.

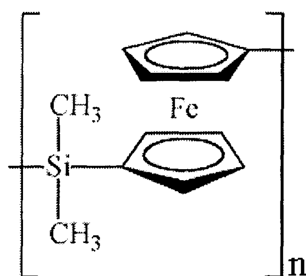

Figure 2.1 Chemical structure of polyferrocenyldimethylsilane (PFS).

2.1.2 PFS Homopolymer and PFS-containing Block Copolymers

Polyferrocenylsilanes are a novel class of transition-metal-containing macromolecules with a backbone that consists of alternating ferrocene and organosilane units. High molecular weight examples of these polymers were first prepared by a ring opening polymerization route [8]. Such a synthetic route allows the control of molecular weight, and gives access to block copolymers with skeletal transition metal atoms, and made it possible to synthesize materials with desired nanostructure and chemical properties [9]. The PFS-containing block copolymers we use in this project were synthesized by Dr. Rob Lammertink, Dr. Mark Hempenius and Mr. Igor Korczagin in Professor G. J. Vancso's group at University Twente.

In order to design the nanostructures of PFS block copolymers for making self-assembled lithographic masks, it is important to know the chemical and physical properties of PFS and the phase behavior of block copolymers made from PFS. PFS is a semi-crystalline polymer with a melting temperature between 110 °C and 145 °C and its glass transition temperature

varies between 26 °C for 10K PFS and 33 °C for very high molecular weight. The density of PFS is 1.44 g/cm^3 (other reports 1.26 g/cm^3) and it can dissolve in many organic solvents such as THF and toluene [8-10]. PFS homopolymers and block copolymers are orange-brown colored, chemically stable at room temperature and may crystallize slowly over time. In general, PFS is an easily handled polymer. To obtain amorphous PFS, which is desired for our purpose, it is necessary to anneal the sample above melting temperature and to quench below the glass transition temperature.

The size, structure and symmetry of the nanostructures formed during phase separation depend on the molecular structures of the block copolymers. The nanostructure can be controlled either by direct synthesis of the block copolymers or by blending homopolymers into block copolymers. Adding homopolymers into block copolymers may lead to an increase of domain size and/ or a phase change. Many PFS-containing block copolymers have been synthesized including PS-PFS, PDMS (polydimethylsiloxane)-PFS, PI-PFS. PS-PFS is one of the most studied block copolymers in this family and its chemical structure is shown in figure 2.2. The morphologies of PS-PFS have been studied using transmission electron microscopy (TEM), small angle X-ray scattering (SAX) and rheology methods [11,12]. Figure 2.3 is the resulting phase diagram of PS-PFS. N_S and N_F are the degree of polymerization (number of repeating unit) of the PS block and PFS block. The total segment-segment interaction for this polymer is $N\chi/k_BT = (N_S+N_F)\ \chi/k_BT$. In this diagram, $(N_S+N_F)/T$, which is proportional to the total segment interaction, is plotted against overall volume fraction of PFS. Neat block copolymer data are given as solid symbols and blended copolymers are displayed as open symbols. The phase diagram of PS-PFS is similar to that of conventional organic-organic block copolymers. The phase transitions between ordered phases are located at 22%, 43%, 65%, 68% and 79% for body-center-cubic spheres (BCC), hexagonal packed cylinders (HEX), alternating lamellae (LAM), double gyroid (DG), HEX, BCC. The dotted lines in figure 2.3 represent these phase boundaries. The squares in the figure display the disordered states.

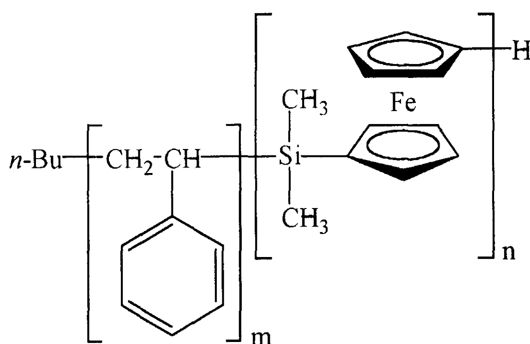

Figure 2.2 Chemical structure of PS-PFS block copolymer.

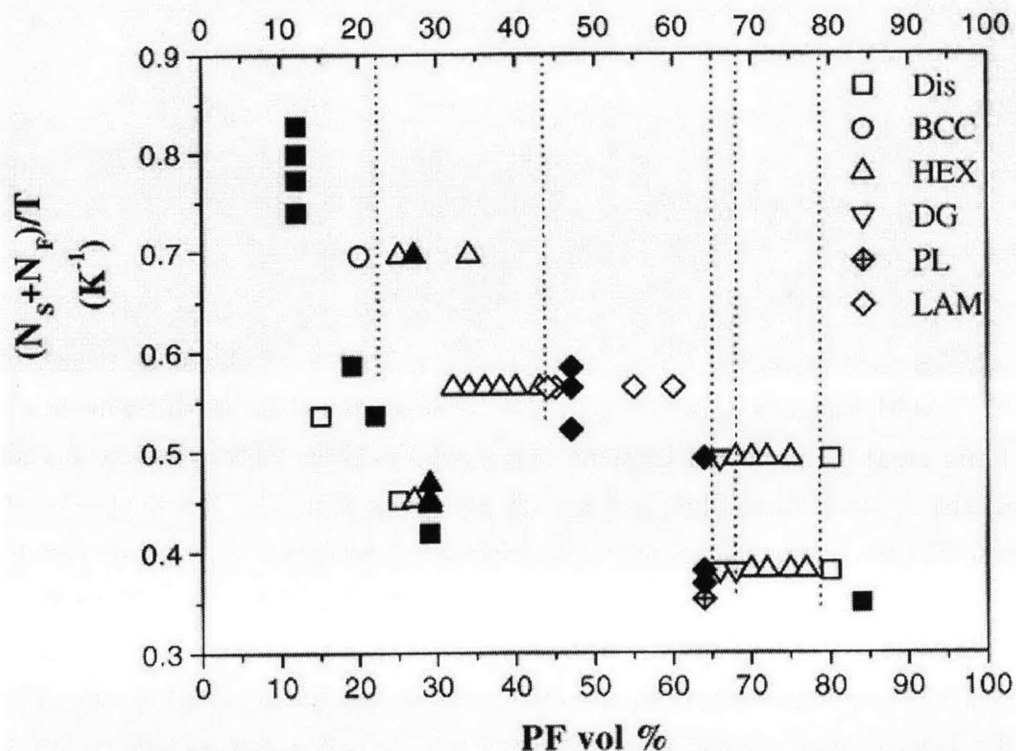

Figure 2.3 Phase diagram of PS-PFS copolymers. [Ref 11]

2.1.3 PFS-containing Block Copolymers as Lithographic Templates

Two-dimensional periodic structures from thin films of perpendicular cylinders or spheres are ideal for making a self-assembled mask. Cylindrical morphology PS-PFS and PI-PFS were spin-cast on silicon wafers to form thin films with various thickness. In thin films of PS-PFS, the orientation of the PFS cylinders is sensitive to the thickness of the film. When the film thickness is close to the domain period plus wetting layer thickness, cylinders lie parallel to the substrate. When the film thickness differs greatly from that value, cylinders became perpendicular to the substrate [11]. PI-PFS followed a similar trend, and highly uniform perpendicular cylinders could be obtained in very thin films. The domain spacing of PI-PFS (36 kg/mole for PI and 12 kg/more for PFS, known as IF 36/12) is 30 nm. Figure 2.4 shows the morphology of IF 36/12 thin films of different thickness. The thicker films have a mixed morphology of parallel and perpendicular cylinders (figure 2.4a and 2.4b). As thickness decreases, more cylinders become perpendicular to the substrate. When the film is thin enough, all cylinders are perpendicular to the substrate as shown in figure 2.4c.

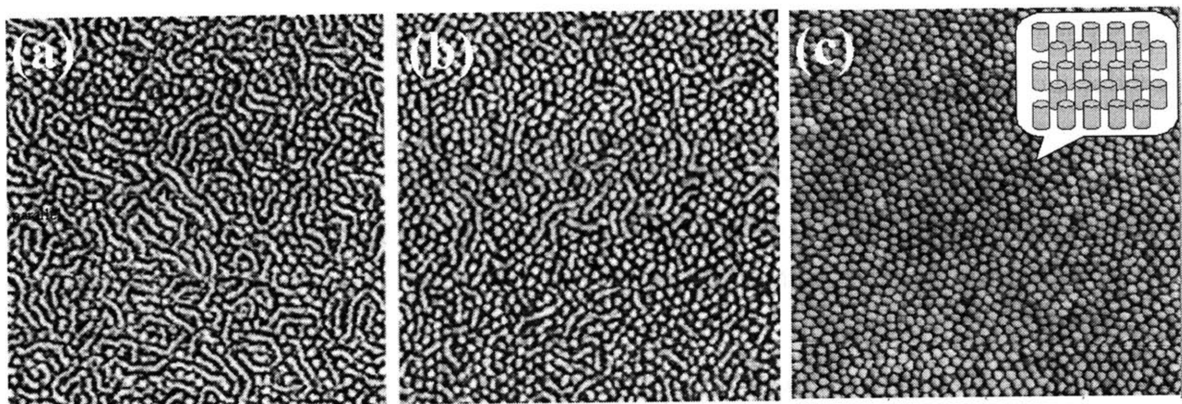

Figure 2.4 AFM images of morphologies of IF 36/12 thin film of different thickness (1 μm X 1 μm area). Unprotected isoprene is removed to show PFS cylinders. (a) 30 nm thick film, (b) 27 nm thick film, and (c) 25 nm thick film. As the thickness of the copolymer thin film decreases, more of the PFS cylinders become perpendicular to the substrates.

Although PI-PFS forms nice perpendicular cylinders and can be converted to nanopillars of PFS on the surface after oxygen plasma treatment, a structure that is desired for block copolymer templates [12], the perpendicular cylindrical morphology of PI-PFS is not stable. In the PI-PFS, the low glass transition temperature (around –60 °C) of the PI and its incompatibility with substrate surfaces limits the stability and structural integrity of the nanostructure. Crystallization of the PFS domains can occur at room temperature, at which temperature the PI block is rubbery, resulting in the destruction of the nanodomains. In addition, annealing to improve the phase-separation and the domain uniformity can lead to reorganization of the nanodomains and dewetting of the film from the substrate [13]. Therefore, in this project, instead of PI-PFS, we use PS-PFS where PS is glassy at room temperature (glass transition temperature of PS is around 100 °C) which leads to a more stable structure.

In addition to the material stability, the morphology of the block copolymer is another important consideration. For some applications, cylinders may be required to achieve high aspect ratio nanostructures. However, for fabrication of nanoparticle arrays, a sphere morphology allows easier processing than a cylindrical morphology because there is only one morphology in the one-dimensional sphere system and it has no out-of-plane orientation with respect to the substrate. According to the consideration of etching selectivity, stability and morphology of block copolymer, **in this project we used sphere-morphology PS-PFS (figure 2.2) for the self-assembled lithographic mask**.

From the PS-PFS phase diagram in figure 2.3, to obtain a sphere-morphology block copolymer, a PFS component less than 22% volume fraction is required. Two sphere-morphology PS-PFS polymers, SF 91/21 (91 kg/mole of PS and 21 kg/mole PFS) and SF 32/10 (32 kg/mole of PS and 10 kg/mole PFS), were chosen to fabricate high-density particle arrays. The thin films of these polymers form hexagonally close-packed PFS spheres embedded in the PS matrix. Sphere density and sphere diameter can be estimated from micrographs. When these spheres are used as templates to form magnetic particles, the particles will typically be single domain. The volume fraction, spacing between the spheres, and sphere density of these two polymers in a monolayer of thin film are summarized in table 2.1.

Polymer	PFS Volume Fraction	Sphere Spacing	Sphere Density
SF 91/21	16 %	56 nm	2.38×10^{11} /in^2
SF 32/10	20 %	29 nm	8.86×10^{11} /in^2

Table 2.1 The basic structural data of PS-PFS block copolymers used in this thesis.

Spherical PS-PFS copolymers were synthesized by sequential anionic polymerization. Polymerization of styrene in ethylbenzene was initiated by n-butyllithium and proceeded for a certain time. After the styrene block formation was complete, 1,1'dimethylsily-ferrocenophane and THF were added for formation of the PFS block. Adding a few methanol drops would terminate the polymerization of PFS. Then the block copolymer was precipitated in methanol and then dried out. The block ratios were calculated form 1H-NMR spectrum and GPC measurements were carried out in THF. The polydispersity of our PS-PFS is less than 1.1, which is ideal for making block copolymer template with narrow size distribution.

2.1.4 Preparation of PS-PFS Block Copolymer Thin Films

The block copolymer was spin-coated on silicon or oxide substrates as a 1-3% (wt/wt) PS-PFS solution in toluene. The thickness of polymer thin film increases with solution viscosity and decreases with spin speed. The thickness of the polymer thin film is determined by ellipsometer. For example, a 1.5% of SF 32/10 solution spun at 2000 rpm gives a 51 nm thick polymer film, while a 60 nm thick film forms from a 1.5% of SF 91/21 solution spun at the same speed, because the viscosity is higher for the polymer solution with higher molecular weight at the same concentration. Spin curves of polymer solutions

give correlations between spin speed and film thickness. The thin films are then annealed for 48 hours to improve ordering of the microdomains of block copolymers. SF 91/21 is annealed at 180°C and SF 32/10 is annealed at 140°C.

To be used as lithographic templates, the polymer thin films need to contain a monolayer of PFS spheres. A 39 nm thick SF 32/10 polymer thin film forms a ~ 10 nm PFS brush layer at the substrate interface and a monolayer (29 nm) of spheres as illustrated in figure 2.5.

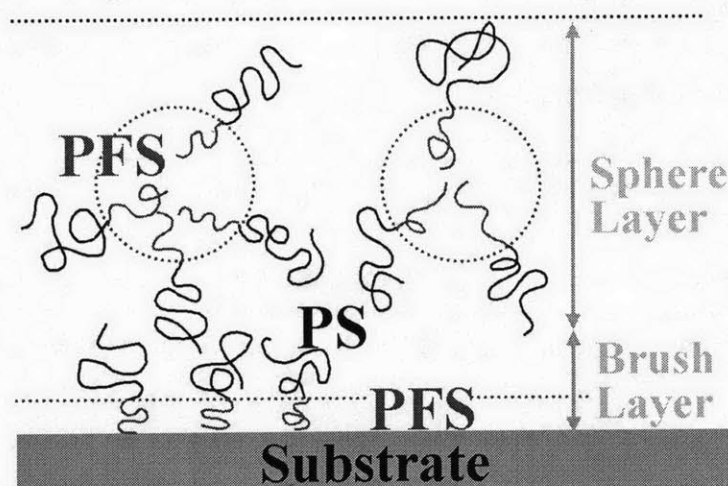

Figure 2.5 Schematic of the arrangement of the polymer chains in the domains and at the silica substrate surface.

Figure 2.6 shows SEM micrographs of the structures of PFS spheres in this 42 nm thick SF 32/10 thin film. The unprotected PS is removed by oxygen plasma to reveal the spatial arrangement of the PFS spheres. This thin film forms uniformly-sized sphere arrays with center-to-center spacing of 29 nm. Such sphere arrays can be used as lithographic templates.

If the polymer film is thicker than the monolayer thickness, one monolayer and some sections of a second layer are formed after annealing as holes and islands. Figure 2.7 shows SEM micrographs of a 48 nm thick SF 32/10 thin film. The one-layer region (hole) and two-layer region (island) are randomly distributed on the surface. The total area covered by the two-layer region on the substrate can be determined by the average thickness of the film. Fewer two-layer regions are present when the thickness of the film is closer to a monolayer thick. In two-layer region, the spheres of the second layer are mostly present in the dips of the first layer as shown in figure 2.7b. These irregular structures are undesired for lithographic applications. Therefore, it is important to control the thickness of the polymer thin film so that uniform sphere arrays can be obtained.

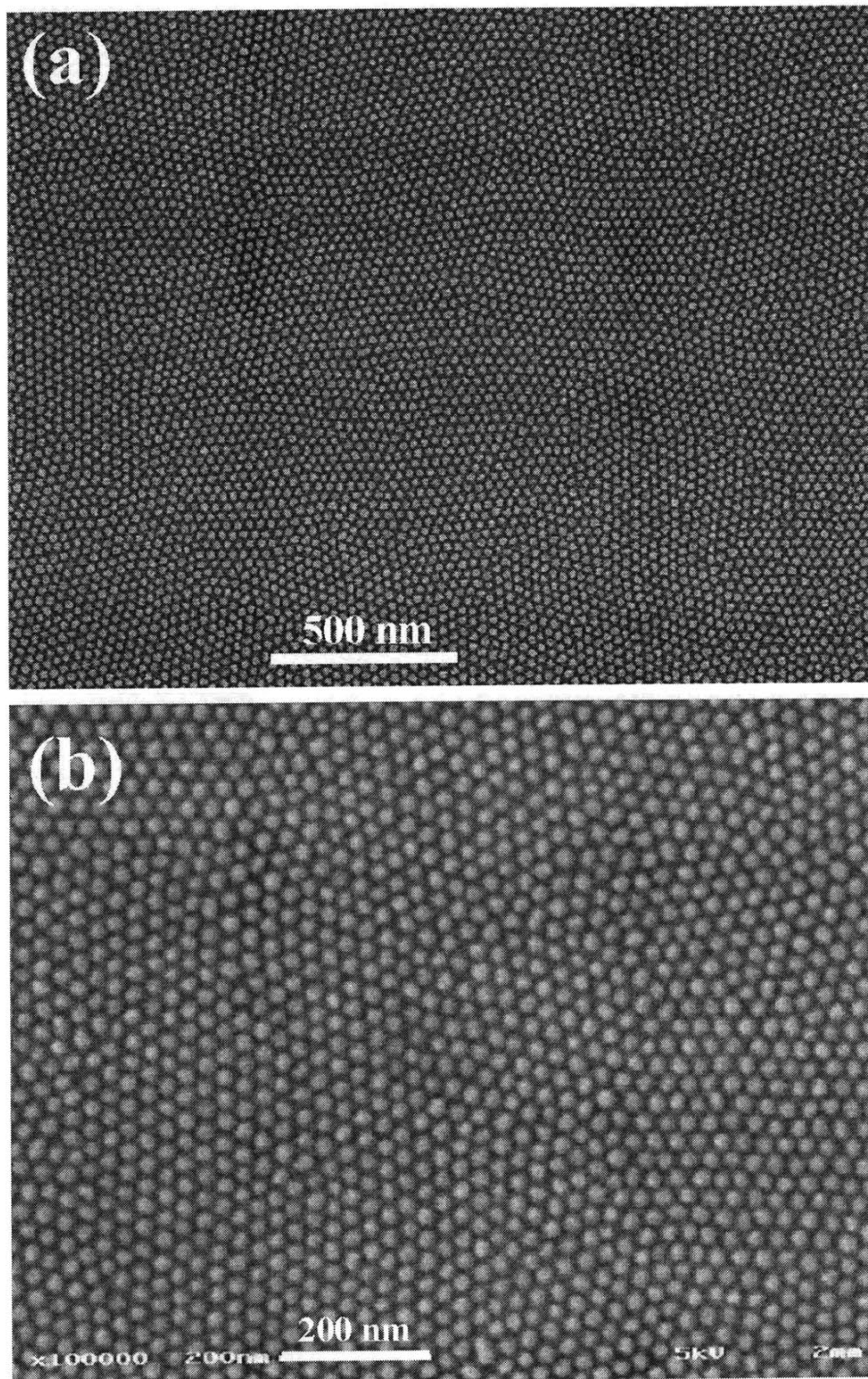

Figure 2.6 SEM micrographs of a 42 nm thick SF 32/10 thin film on silica substrate. (a) Uniform PFS sphere arrays. (b) locally close-packed structures of PFS spheres.

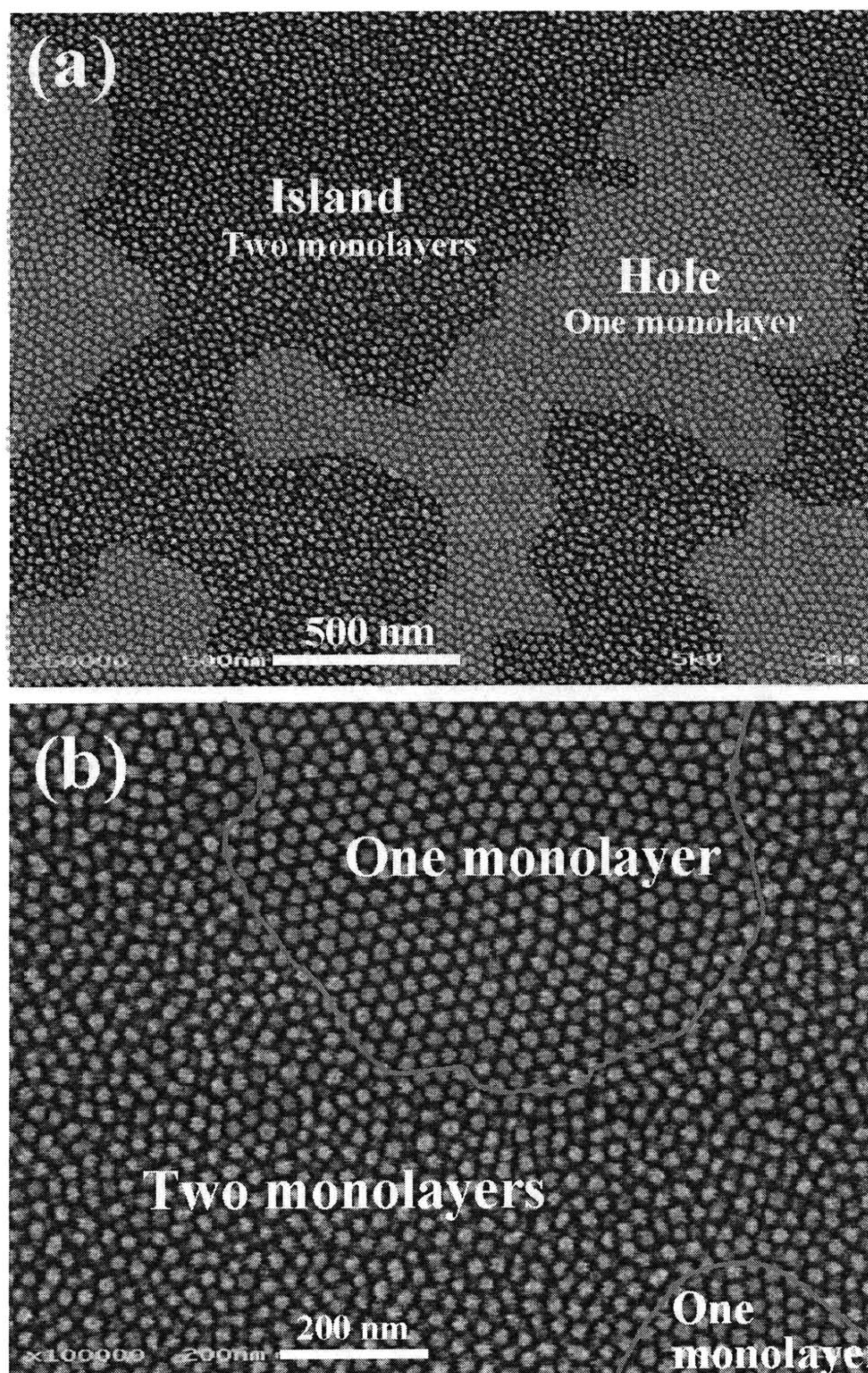

Figure 2.7 SEM micrographs of a 48 nm thick SF 32/10 thin film on silica substrate. (a) Non-uniform PFS spheres. Some regions were one monolayer and the others are two-monolayer areas. (b) The spheres in the second layers are placed at the dips of the bottom layer, and these structures are not as regular as the monolayer region.

2.2 Pattern Transfer Techniques

To use a block copolymer thin film as a self-organizing lithographic mask for fabrication of magnetic particle arrays, pattern transfer techniques play a critical role. Pattern transfer is needed to convert the polymer film into a topological template and to transfer the template structures into magnetic materials. Magnetic particle arrays can be made through either addictive methods or subtractive methods. Electroplating and evaporation are addictive methods, which deposit magnetic materials through the templates with arrays of holes. Electroplating has been used to make high aspect ratio magnetic cylinders and flat magnetic dots have been made by evaporation [2]. On the other hand, a subtractive method involves etching process to remove magnetic material from a continuous thin film to form a discrete dot array.

We used SF 91/21 and SF 32/10 as the lithographic templates because of their high selectivity, stability and compatibility. The PFS in the PS-PFS copolymer is the minority block and form spheres in the PS matrix. Thus, a mask consisting of an array of PFS dot is obtained from these polymers because PFS patterns are left on the surface while unprotected PS is removed. In this case, it would require extra steps to invert the pattern contrast to form arrays of holes needed for addictive processing. Therefore, a subtractive method is simpler and more suitable for pattern transfer when using mask made from our PS-PFS block copolymers.

Plasma etching provides a way to selectively remove materials so that a pattern can be transferred from the mask layer to the other layers. This section covers the basic operation principles for plasma etching and details the conditions for the processes used in this project.

2.2.1 Plasma Process

Basic mechanisms of plasma etching include physical sputtering, chemical etching, and an ion-enhanced energetic mechanism as shown in figure 2.5 [14]. In most cases, several mechanisms are involved in any etching process and can be controlled by the gas species, gas pressure and plasma voltage. In the physical sputtering process (figure 2.8a), high-energy ions mechanically eject substrate material at a low pressure around 10^{-4}-10^{-6} torr. Ion-beam etching (or ion milling), for instance, is a pure physical sputtering process.

The advantage of the ion-milling process is that this mechanism can occur on any substrate, including magnetic materials which are difficult to etch otherwise. In a pure chemical etching process (figure 2.8b), the neutral radicals react with the substrate isotropically at high pressure (0.1-10 torr) and then form volatile products that can be quickly removed through vacuum system. This is typically unsuccessful for etching magnetic materials because they do not form volatile byproducts.

In between pure physical and pure chemical etching, ion-enhanced energetic processes (figure 2.8c and 2.8d) can happen under certain conditions and pressure ranges ($10^{-3} \sim 0.1$ torr). The energetic ions produce reactive gas species and activate the substrate surface. The ion bombardment enhances the reactivity of the substrate, allowing chemical reactions to gasify the materials. In addition, since ions are accelerated across the plasma sheath and strike the surface vertically, ion-enhanced etching is directional. This process is a typical mechanism in reactive ion etching (RIE) and, ideally, provides high chemical selectivity and vertical sidewalls, which are critical in successful pattern transfer. In some cases, a polymerization reaction takes place on the surface of the trench and protects sidewall by inhibiting ion bombardment. This ion-enhanced inhibitor process typically gives straighter sidewalls (figure 2.8d).

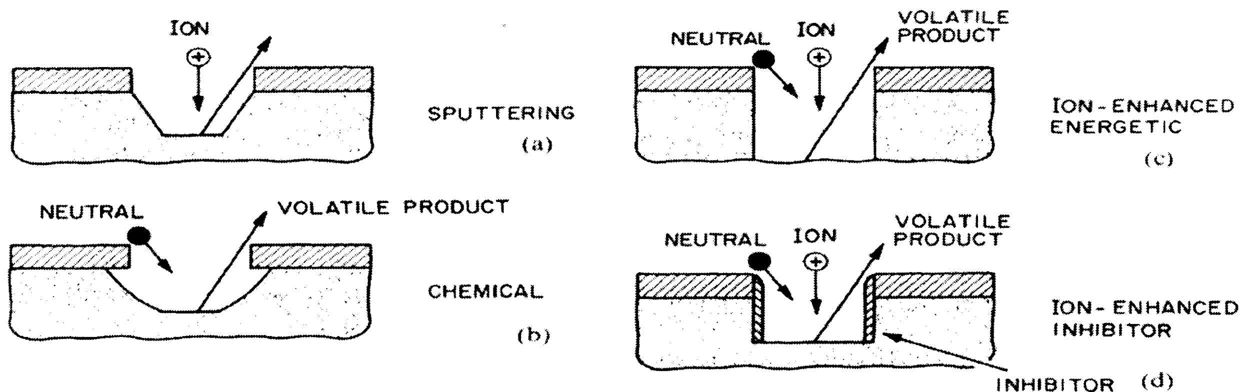

Figure 2.8 Basic mechanisms for plasma etching. [Ref. 14]

2.2.2 Pattern Transfer Process and Conditions – Reactive Ion etching

We used a multilayer scheme to transfer the pattern from a block copolymer thin film to magnetic layer. The multilayer scheme is polymer/ silica/ tungsten / magnetic layer as shown in figure 2.9. The thin films of silica, W, Co are electron-beam evaporated onto

unheated silicon substrates using an Airco Temescal BJD 1800 E-Beam Evaporator. RIE was used in this project to transfer pattern form polymer films to polymer templates, oxide layers and tungsten layers. All RIE was performed on a Plasma Therm Model 790 plasma etcher. Then final etching of the magnetic layer was performed on an Ion Tech ion beam etcher to transfer the pattern from tungsten layer to the magnetic layer. This part describes experimental procedures and considerations for the polymer etching process, oxide etching process and tungsten etching process. The evaporator, plasma etcher and ion-beam etcher are facilities in the NanoStructure Laboratory at MIT.

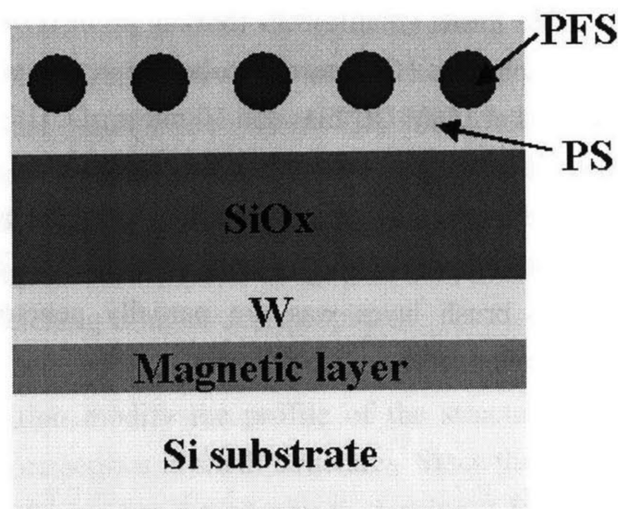

Figure 2.9 Multilayers for pattern transfer from block copolymer to magnetic layer.

A. Polymer Etching

PS-PFS thin film is etched in low-bias, low-pressure O_2-RIE for the best selectivity between the PFS block and the PS block. PS forms volatile byproducts with O_2 plasma and is quickly removed away. Under O_2 plasma, PFS spheres form a surface oxide layer protecting them from further etching. The selectivity between PS and PFS is higher in the lower bias condition, because the oxide protection layer survives longer if there is less physical sputtering. High oxygen pressure leads to high etching rate and fast erosion of the PFS spheres. Low oxygen pressure reduces the etching rate and enables good control of the etching process. More studies of converting PS-PFS block copolymers into templates are discussed in chapter 3.

O_2-RIE was performed at 30V DC bias and 5 mtorr of O_2 to etch SF 91/21 and SF 32/10 polymer thin film. Overetching results in non-uniformity of the size of the PFS spheres.

This O_2-RIE condition is milder than typical recipes for etching polymeric resists or antireflection coating but gives good selectivity and control of etching PS-PFS block copolymers.

B. Silica Etching

Silica (silicon oxide) layer is used as an intermediate layer between the polymer template and hard mask. The reason to use silica is that polymer features can be transferred to the silica layer and the hard mask layer can be patterned easily using the silica structure as a mask with RIE. Silicon oxide forms volatile SiF_4 (boiling point is –86 °C) in CF_4, CHF_3, C_3F_8, C_2F_6 and many other plasmas. CF_3 seems to be the active echant during the RIE process. CHF_3-RIE performed at 150V DC bias and 10 mtorr of CHF_3 had good anisotropy and selectivity for etching silica with a block copolymer mask. Both evaporated silica and thermal silica seem to have the same etch rate. The selectivity between oxidized PFS dots and silica is high and the sidewalls of the silica features are straight. There is no etching of the silica layer if the PFS brush layer was not partially penetrated during O_2-RIE. Overetching reduces the diameters of the silica pillars.

C. Tungsten Etching

Tungsten (W) layer is the hard mask for patterning magnetic thin films. The reason for choosing W as hard mask will be discussed in the ion-beam etching section. W forms WF_6 (boiling point is 17.5 °C) in a CF_4 plasma, where fluorine atoms are the primary etchants. Adding O_2 to CF_4 plasmas enhances the fluorine atom density and reduces carbonaceous deposits by reactions of oxygen atoms and CF_x moieties. It is known that addition of 15% O_2 in CF_4 plasma gives a high W etching rate and high etching contrast between silica and W. The selectivity between W and silica under these RIE conditions is about 3.5 to 1[15]. A mixture of 85% CF_4 and 15% O_2 with a total pressure of 10 mtorr and 30 V DC bias was used to etch the W film. Low bias reduces the etch rate of silica masks.

On the other hand, CHF_3 forms carbonaceous sidewall deposition with W so that W is hardly etched in CHF_3 gas. Therefore, CHF_3 plasma can be used to remove the silica caps after W etching is done.

2.2.3 Ion-beam Etching for Patterning Magnetic Materials

Etching magnetic thin film into discrete dots is a challenge. Since magnetic materials such as cobalt and iron do not form volatile compounds with reactive radicals, ion-beam etching is the only method to anisotropically remove magnetic materials. Broad-beam ion sources have been used extensively for patterning[16,17]. At the present time, ion-beam etching (or ion milling) is the primary dry-etching method for critical patterning steps in the fabrication of magnetic recording heads. Applications include read-element shaping, write-element pole-tip trimming, removal of the plating seed layer, and air-bearing-surface definition [18]. In ion-beam etching, ionization is achieved by a Kaufman source, which contains a hot filament, a radio-frequency (or microwave) source. Ions are extracted through a series of grids and directed to the wafer to be etched. The ionic charges in the ion-beam etching chamber are neutralized by electrons to avoid charging and arcing on the sample. The pressure in an ion-beam etching system is typically one to two orders of magnitude lower than that in a sputtering or reactive ion etching system. As a result, the scattering of the ions is minimized, and the etching is highly anisotropic.

Faceting and redeposition modify the profile of the structure during ion-beam etching. These problems are more serious in small structures. Since the momentum transfer is angle dependent, the ion sputtering has a tendency to develop a facet on the mask edge at the angle of maximum etch rate. The corner of the mask etches faster than the center of the mask. This results in the tapered structures instead of straight sidewalls. Because the sputtered products of ion-milling are non-volatile, they redeposit on step edges. Redeposition involves non-volatile species from the removed materials settling on the sidewalls of the mask and etched trench and gives a sloped sidewall profile. A thinner mask with higher selectivity to the target magnetic materials in the ion-beam etching reduces the both faceting and redeposition problem.

At dimensions of tens of nanometers, good selectivity is a key to achieve the desired structure. Physical sputtering is a momentum transfer process, thus the sputtering selectivity depends on the mass of incident ion (M_1) and target atom (M_2) [19]. The sputtering yield S is defined as the ratio of number of ejected atoms and number of incident ion, which is

$$S = \frac{3\alpha}{4\pi^2} \frac{4M_1M_2}{(M_1+M_2)^2} \frac{E_1}{Eb}$$

where α is the efficiency for momentum transfer, E_1 is the ion incident energy and Eb is the

surface binding energy of the sputtered materials. Larger differences between M_1 and M_2 lead to smaller the sputter yields of M_2, thus higher resistance to the ion milling process. Table 2.2 shows the sputtering yield data for Co, Ti and W using He, Ne, and Ar ions-beam of 500 eV.

Target	He (M=4)	Ne (M=20)	Ar (M=40)
Co (M=59)	0.13	0.9	1.22
Ti (M=49)	0.07	0.43	0.51
W (M=184)	0.01	0.28	0.57

Table 2.2 The sputter yield of Co, Ti and W at different ion beam conditions.

In order to etch the pattern down to the magnetic layer, a hard mask layer to support the high-energy ion flux is required. Polymeric thin films are not good hard mask layers for ion milling because of their low density and weaker binding energy. To achieve high selectivity between hard mask and magnetic layer, a heavier material for the mask and a lighter inert gas for ion flux are required from the above table and equation. Because of good resistance to ion milling and well-known process for RIE of W layer, W layer was chosen as a hard mask for patterning magnetic materials. It was demonstrated that the experimental etching selectivity for W to Co is 2.3 using Ne gas, with no obvious faceting and redeposition [20].

In this project we use Ar and Ne ion beams to transfer the pattern from W to magnetic thin films. The conditions for ion-beam etching are listed in table 2.3.

Ion Beam	Bias (eV)	Beam Current (mA)	Current Density (mA / cm^2)	Gas Pressure (torr)	Etch Rate (nm / min)
Ar	500	36-43	0.4-0.6	3×10^{-4}	7-12
Ne	1000	36-43	0.4-0.7	4.5×10^{-4}	5-8

Table 2.3 The parameters for Ar and Ne ion-beam etching.

The end point of the ion-beam etching process can be determined by measuring magnetic properties of the sample along the etching process. Details of ion-beam etching process will be discussed in chapter 3.

2.3 Fabrication of Topographical Substrates

The structures of self-organizing materials are typically characterized as having short-range order. A typical block copolymer thin film falls in this category. Figure 2.6 shows the "polycrystalline structure" of SF 32/10 thin film with a "grain" diameter of a few hundreds of nm. However, long-range ordered structures are desired for certain applications such as patterned magnetic recording media. An artificial topographic pattern on the substrate can be used to orient the growth of a thin film in a process known as graphoepitaxy [21]. In this thesis, we used topographical substrates to template self-assembled process and improve long-range ordering of block copolymer thin film. Large-area topographical substrates with regular features of few hundreds nm to a micron are needed for the templating experiments.

The topographical relief structures for templated self-assembly were made by interference lithography [22, 23]. Interference lithography is a maskless method which is ideal for patterning large-area periodic structures. Two interfering beams form a standing wave pattern as illustrated in figure 2.10a. The period (P) of the standing wave depends on the wavelength (λ) and the half-angle at which two beam intersect (θ).

$$P = \frac{\lambda}{2\sin\theta}$$

A Lloyd's mirror is one of the methods to produce interference pattern (figure 2.10b). A laser beam is directed through a spatial filter to remove high frequency noise and then expanded to cover the area of the mirror/ substrate assembly. The substrate is mounted perpendicular to the mirror on a rotation stage; therefore, the light arriving directly at the substrate comes at the same angle as the reflected beam from the mirror and an interference pattern is formed on the substrate. The period of the pattern can be adjusted by simple rotation of the whole mirror/ substrate assembly without the need of realignment of the optical path. In addition, the rigid mechanical connection between the substrate and mirror fixes the length of the optical path for the two incident beams and thus this set up is relatively robust.

The substrates were 10 cm-diameter silicon wafers, which were thermally oxidized to form a 150 nm thick surface layer of silica. A trilayer resist stack consisting of a 200 nm thick antireflection coating layer (ARC, AZ BARLi), a 30 nm thick evaporated silica interlayer then a 200 nm thick photoresist layer (PFI-88 from Sumitomo) was deposited sequentially over the oxidized wafer. A 325 nm wavelength HeCd laser was used to expose grating structures in the resist with a periodicity that was varied from 200 nm to 1500 nm by

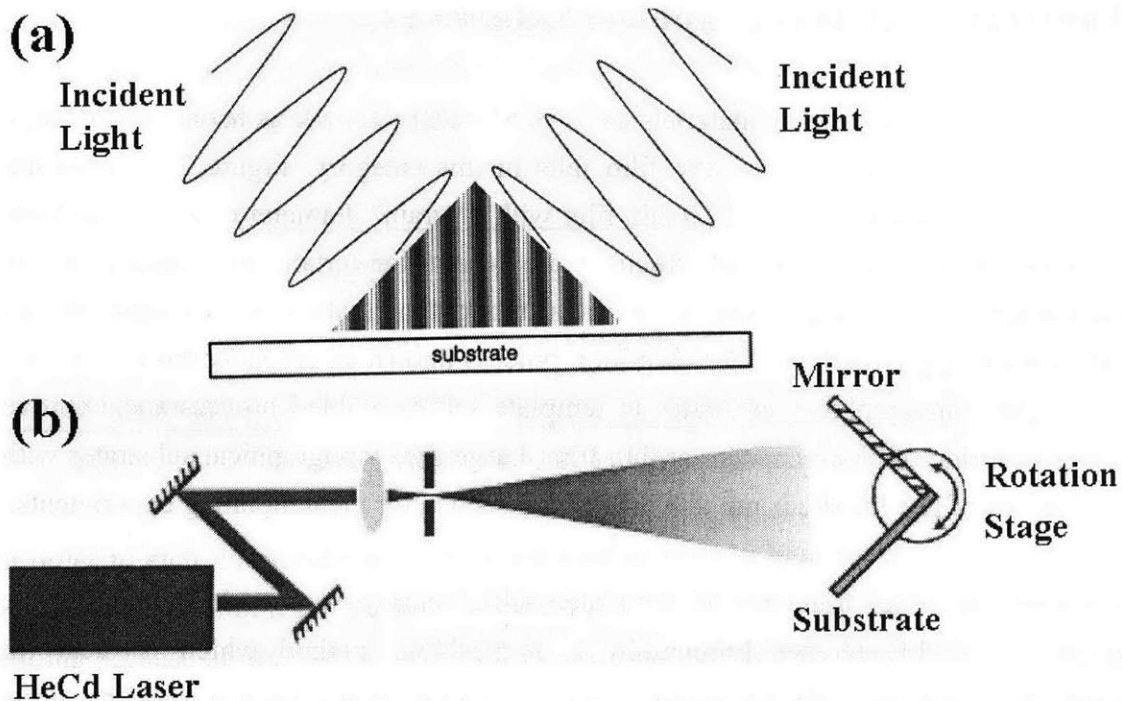

Figure 2.10 (a) Two beams interference form a standing wave pattern. (b) Lloyd's mirror set up for interference lithography. [Ref 23]

varying the relative angle between incident beam and substrate. The resist was developed in CD26 after exposure and the pattern transferred down into the underneath layers.

Figure 2.11 demonstrates the process of pattern transfer from the resist to the underlayers. A grating in the developed photoresist is shown in figure 2.11a. CHF_3 RIE is used to etch the silica interlayer and this interlayer serves as the hard mask to etch thick ARC layer using O_2+He RIE. High etching bias improves etching anisotropy, which is particularly important for etching thick ARC layer. The addition of He gas dilutes O_2 gas and stabilizes plasma. The etch rate of ARC with this O_2+He-RIE depends on the dimension of the features; higher etch rate was found for larger features. Figure 2.11b shows the etched trilayer resist. Then the grating structure is transferred to the thermal oxide layer through another CHF_3 RIE process as illustrated in figure 2.11c. After removing the residual ARC on the top with an RCA clean, a square-wave grating topography remains in the thermal oxide (figure 2.11d). The duty cycle of the grating and the depth of the steps are adjusted by controlling the exposure time and etch process. With the control of period, groove width and groove depth, various gratings were made for testing the templated self-assembly of block copolymers. Table 2.4 lists the parameters used in the fabrication of grating structures, etching time varies with the grating period and desired duty cycle. Longer etching time is needed for smaller grating period.

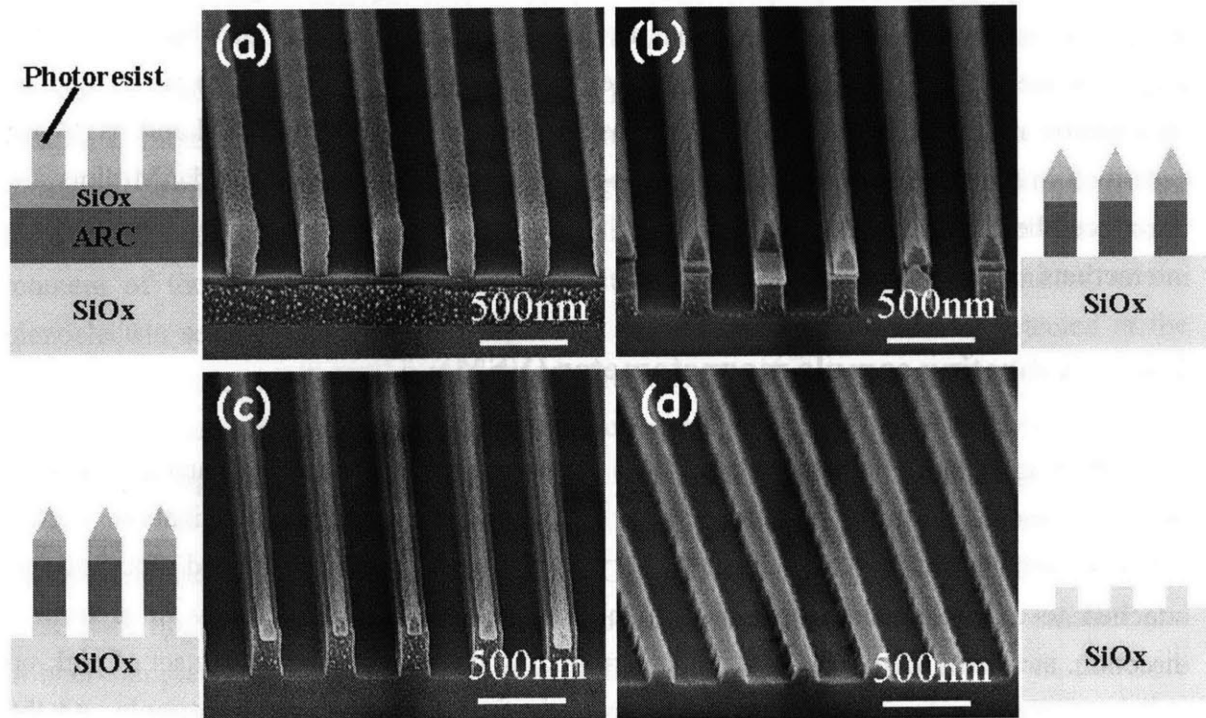

Figure 2.11 SEM micrographs of grating substrates. (a) Grating structures in the photoresist after development. (b) Etch into the interlayer and ARC. (c) Etch into oxide. (d) Oxide grating after RCA clean.

Process	Conditions	Time (min : sec)
RIE 20 nm Oxide	150 V DC, 10 mtorr CHF_3	1:00 ~ 1:30
RIE 200 nm ARC	250 V DC, 6 mtorr O_2+He (2:1)	2:00 ~ 3:00
RIE thermal Oxide	150 V DC, 10 mtorr CHF_3	depends on the required depth
RCA Clean	$H_2O:NH_4OH:H_2O_2 = 5:1:1$, 80 °C	15:00

Table 2.4 Fabrication process of grating structures.

2.4 Magnetic Characterization

Ferromagnetism of materials can be studied by hysteresis measurement. A hysteresis loop is the relationship between the material's magnetization and an externally applied magnetic field. Magnetic characterization of a particle array involves generating a hysteresis loop using a magnetometer that senses the magnetic moment of a sample. Both vibrating sample magnetometer (VSM) and alternating gradient field magnetometer (AGM) were used to characterize magnetic particle arrays. The basic setup and principles of VSM and AGM are described in this section. In addition, sweep-rate dependent coercivities and ΔM plots are introduced here for characterizing activation volume of particle switching and inter-particle interactions.

2.4.1 Vibrating sample magnetometer (VSM)

The vibrating sample magnetometer (VSM) is based on the principle of Faraday's law of induction and is the most commonly used method of magnetic characterization. Figure 2.12a is a schematic of a VSM. In the VSM, the sample is mounted at the end of a rigid rod attached to a mechanical resonator, which oscillates the sample, usually in a vertical direction, at a fixed frequency at 75 Hz. Surrounding the sample nearby is a set of pick-up coils. An electromagnet produces a DC magnetic field to magnetize the sample. As the sample oscillates, its magnetic field, which is proportional to the magnetization (M) of the sample, leads to a varying magnetic flux through the coils. The induced EMF voltage is directly proportional to dM/dt; therefore, the magnetic moment of the sample can be derived by calibrating with a reference sample. The voltage measured across the sensing coils depends on the vibration frequency, vibration amplitude, and the sensitivity function of sensing coils [24]. The VSM usually has a sensitivity limit of $10^{-5} \sim 10^{-6}$ emu.

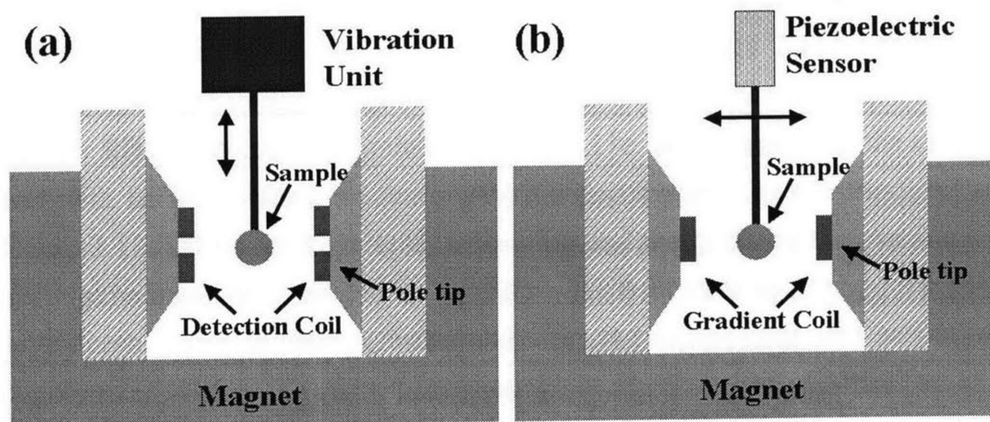

Figure 2.12 Schematics of (a) VSM, and (b) AGM

2.4.2 Alternating Gradient Magnetometer (AGM)

An alternating gradient field magnetometer (AGM) is a highly sensitive measurement system, capable of measuring a hysteresis loop in a very short time. It uses a modified technique compared to conventional VSM. In VSM, a sample placed in a magnetic field is vibrated at a fixed frequency via an electro-mechanical transducer. In an AGM, an alternating gradient field is utilized to exert a periodic force on a magnetized sample. The sample is mounted on the tip of an extension rod attached to a piezoelectric element as illustrated in figure 2.12b. The field gradient generated from the coils exerts an alternating force on the sample proportional to the magnitude of the gradient field and the magnetic moment of the sample. The resulting deflection of the extension is transmitted to the piezoelectric sensor and the output signal of the piezoelectric element is detected at the operating frequency of the gradient field. The signal from the piezoelectric element is greatly enhanced by operating at or near the mechanical resonant frequency of the assembly. Therefore, a high sensitivity of $10^{-7} \sim 10^{-8}$ emu can be achieved in AGM [25].

There are advantages and disadvantages of AGM. Compared with VSM, AGM has higher sensitivity and better signal to noise ratio, hence, AGM allows measuring smaller and thinner samples and requires less time to complete a hysteresis loop. However, there are more restrictions for the sample in the AGM measurement. The size and mass of the sample must be small enough so that the resonance frequency of the piezo is not reduced significantly and the gradient field is uniform for the whole sample. The measured moment is sensitive to sample placement due to the gradient field. In addition, when measuring low coercivity sample ($H_C < 100$ Oe), it is necessary to reduce the magnitude of the gradient field in order to maintain the accuracy of measurement and hence reduce the sensitivity and signal to noise ratio. In general, AGM is suitable for small, low moment samples, while VSM is better for large, low coercivity samples.

It is sometimes difficult to quantify the magnetic moment using AGM because the typical sample size was larger than the size of the AGM standard, which is an epoxy sealed 4 mm^2 square Ni foil. For example, when 64 mm^2 sample is measured in a well-calibrated VSM and AGM, the measured coercivities are the same for both measurements, but the results of saturation magnetization (Ms) and the remanence are different. For instance, Ms = 440 μemu from AGM and Ms = 385 μemu from VSM. Therefore, we compared the a series of sample of the same sample size and shape with AGM, but use VSM for absolute values for magnetic properties.

2.4.3 Sweep-rate Dependent Coercivity

Switching volume (or activation volume), V, is the unit volume of magnetic moments that switch together in magnetization reversal. The energy barrier for switching the magnetization of a particle is proportional to KV, where K is the magnetic anisotropy energy. Therefore, the switching volume can be used to characterize the thermal stability and the switching behavior of the magnetic particle.

The energy barrier and switching volume of the medium are often determined by measuring the scan-rate dependence of coercivity, H_C (R). The coercivity increases as the scan rate (or field pulse time) increases and the smaller the switching volume, the larger is the change in time-dependent coercivity. The basic principle and measurement are described by Sharrock [26]. Defining the scan-rate dependent coercivity, Hc(t), as the field that causes switching of half of the particle in the sample during time t,

$$H_C(t) = H_0\{1-[(\frac{k_B T}{KV})\ln(f_0 t)]^n\}\ldots\{2\}$$

where H_0 is the anisotropy field at which field the energy barrier is zero; k_B is Boltzman constant and f_o is the thermal attempt frequency which is around 10^9 Hz. Figure 2.13 shows the scan rate dependent coercivity of typical magnetic recording media [27]. Four different media with different thickness δ are measured. The sweep-rate dependent coercivity of all four samples varies mostly linearly with logarithm of field pulse length. This trend follows equation {2} over a large time scale. The switching volume can be derived from the inverse slope 1/C ~ KV/k_BT. It is obvious that thinner media has smaller inverse slope, thus smaller switching volume. The switching volume scales up with the thickness of the magnetic film.

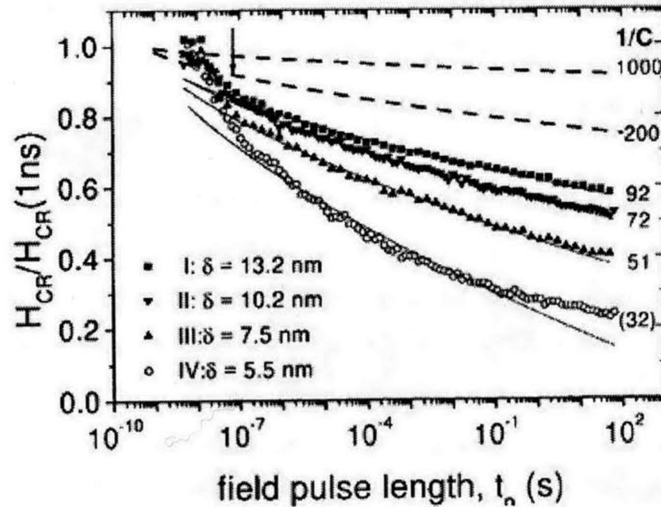

Figure 2.13 Scan-rate (pulse width) dependent coercivity. [Ref 27]

The switching volume can be compared with the actual grain volume, V_P. Ideally, $V \sim V_P$ is desired for patterned media applications. Measuring the switching volume of magnetic nanostructures provides us a tool to characterize the reversal in magnetic particle arrays.

2.4.4 ΔM Plots

The magnetic properties of small particle arrays can be greatly affected by interparticle interactions. Remanence curves probe the irreversible component of magnetization and can supply important information about the intrinsic magnetic properties of the system. There are two basic remanence curves: isothermal remanent magnetization (IRM) and dc demagnetization (DCD) curves. IRM is obtained by magnetizing an initially AC demagnetized sample by applying an increasing field, H, in small steps and measuring the remanence, $M_r(H)$, after removal of the field. The DCD curve is similarly measured by applying an increasing negative field to an initially saturated sample. $M_r(\infty)$, and the remanence, $M_d(H)$, is obtained after removal of the field. For an assembly of non-interacting, uniaxial single domain particles, Wohlfarth showed that $M_r(H)$ and $M_d(H)$ are related according to the following expression [28]:

$$M_d(H) = M_r(\infty) - 2M_r(H)$$

Henkel proposed that deviations from this relation can be attributed to interparticle interactions as long as the particles retain their single domain, uniaxial behavior [29]. Hence, it is possible to determine whether the interparticle interactions enhance or reduce the magnetization of the sample. Then ΔM is defined as following,

$$\Delta M = 2M_r(H) - 1 - M_d(H)$$

where $M_r(H)$ and $M_d(H)$ are normalized by $M_r(\infty)$. Positive values of ΔM are due to interactions promoting the magnetized state while negative values of ΔM are caused by interactions tending to assist magnetization reversal.

Figure 2.14 shows the ΔM deviations of α-Fe metal particles at different packings [30]. P is the packing fraction of magnetic particles in the sample. Negative ΔM indicates these α-Fe metal particles are demagnetized by their neighboring particles. The interaction of these magnetic particles increase as the packing fraction because of smaller spacing between the particles in a denser sample.

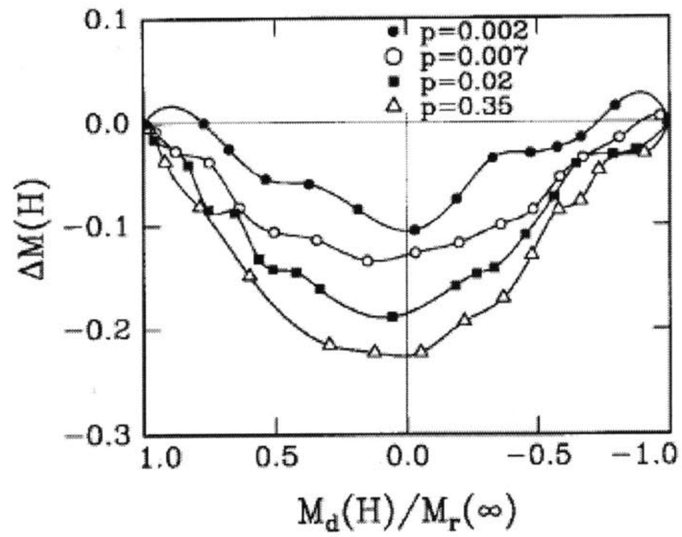

Figure 2.14 ΔM deviations of α-Fe metal particles at different packings. [Ref 30]

Reference

1. M. Park, C. Harrison, P. M. Chaikin, R. A. Register, D. H. Adamson, Science 276, 1401 (1997); C. Harrison, M. Park, P. M. Chaikin, R. A. Register, D. H. Adamson, J. Vac. Sci. Technol. B 16, 544 (1998); R. R. Li, P.D. Dapkus, M. E. Thompson, W. G. Jeong, C. Harrison, P. M. Chaikin, R. A. Register, D. H. Adamson, Appl. Phys. Lett. 76,1689 (2000); M. Park, P. M. Chaikin, R. A. Register, D. H. Adamson, Appl. Phys. Lett. 79, 257 (2001)
2. T. Thurn-Albrecht, J. Schotter, G. A. Kastle, N. Emley, T. Shibauchi, L. Krusin-Elbaum, K. Guarini, C. T. Black, M. T. Tuominen, T. P. Russell, *Science*, **290**, 2126 (2000); K. Liu, S. M. Baker, M. Tuominen, T. P. Russell and I. K. Schuller, *Phys. Rev. B* **63**, 060403R (2001); T. Shibauchi, L. Krusin-Elbaum, L. Gignac, C. T. Black, T. Thurn-Albrecht, T. P. Russell, J. Schotter, G. A. Kastle, N. Emley, M. T. Tuominen, *J. Mag. Mag. Mater.* **226**, 1553 (2001); Z. Q. Lin, D. H. Kim, X. D. Wu, L. Boosahda, D. Stone, L. LaRose, T. P. Russell, *Adv. Mater.* **14**, 1373 (2002); K. Shin, K.A. Leach, J. T. Goldbach, D. H. Kim, J. Y. Jho, M. Tuominen, C. J. Hawker, T. P. Russell, *Nano Lett.* **2**, 933 (2002); M. Bal, A. Ursache, M. T. Touminen, J. T. Goldbach, T. P. Russell, *Appl. Phys. Lett.* **81**, 3479 (2002)
3. G. N. Taylor, T. M. Wolf, L. E. Stillwagon, *Solid State Technol.* **27**, 145-155 (1984)
4. S. A. Macdonald, H. Schlosser, H. Ito, N. J. Clecak, C. G. Willson, *Chem. Matter.* 3, 435 (1991); D. E. Seeger, D. C. LaTulipe, R. R. Kunz, C. M. Garza, M. A. Hanratty, *IBM J. Res. Develop.* **41**, 105 (1997)
5. J .P. Spatz, T. Herzog, S. Mobmer, P. Ziemann, M. Moller, *Adv. Mater.* **11**, 149 (1999); B. Koslowski, S. Strobel, T. Herzog, B. Heinz, H. G. Boyen, R. Notz, P. Ziemann, J .P. Spatz, M. Moller, *J. Appl. Phys.* **87**, 7533 (2000)
6. R. G. H. Lammertink, M A. Hempenius, V. Z. H. Chan, E. L. Thomas,G. J. Vancso, *Chem. Mater.* **13**, 429 (2001)
7. R. G. H. Lammertink, M A. Hempenius, J. E. van den Enk, V. Z. H. Chan, E. L. Thomas, G. J. Vancso, *Adv. Mater.* **12**, 98 (2000)
8. D. A. Foucher, B. Z. Tang , I Manners, *J. Am. Chem. Soc.* **114**, 6246 (1992)
9. R. Rulkens, Y. Ni, I. Manners, *J. Am. Chem. Soc.* **116**, 1212 (1994); Y. Ni, R. Rulkens, I. Manners, *J. Am. Chem. Soc.* 1**18**, 4102 (1996)
10. R. G. H. Lammertink, M.A. Hempenius, I. Manners, G. J. Vancso, *Macromol.* 31, 795 (1998)
11. R. G. H. Lammertink, M.A. Hempenius, E. I. Thomas, G. J. Vancso, *J. Poly. Sci. Poly. Phys.* **37**, 1009 (1999); W. Li, N. Sheller, M. D. Foster, D. Balaishis, I. Manners, B. Annis, J. S. Lin, *Polymer* **41**, 719 (2000)
12. R. G. H. Lammertink, M.A. Hempenius, G. J. Vancso, K. Shin, M. H. Rafailovich, J. Sokolov, *Macromol.* **34**, 942 (2001)
13. R. G. H. Lammertink, M. A. Hempenius, G. J. Vancso, *Langmuir* **16**, 6245 (2000)

14. M. Madou, *Fundamentals of Microfabrication*, chapter 2, p52-78, CRC Press (1997)
15. M. E. Burba, E. Degenkolb, S. Henck, M. Tabasky, E. D. Jungbluth, R. Wilson, *J. Electrochem. Soc.* 2113 (1986); D. W. Hess, *Solid State Tech.* April, 97 (1988)
16. H. R. Kaufman and R. S. Robinson, *Operation of Broad-Beam Source*, Commonwealth Scientific Corporation, Alexandria, Virginia (1986)
17. J. M. Harper, "Ion Beam Etching," *Plasma Etching*, D. M. Manos and D. L. Flamm, Eds., Academic Press, Inc., San Diego, p391-424 (1989); P. R. Puchett, S. L. Michel, and W. E. Hughes, "Ion Beam Etching," *Thin Film Processes II*, J. L. Vossen and W. Kern, Eds., Academic Press, Inc., Boston, p749-782 (1991)
18. A. Hayes, J. F. Weldon, E. Ostran, and R. Gambino, "Ion Milling for Thin-Film Head Fabrication," *Data Storage*, PennWell Publishing Co., Tulsa, OK, March, p43-47 (1995); R. Hsiao, *IBM J. Res. Develop.* **43**, 89 (1999)
19. M. Ohring, *The Material Science of Thin films*, p111-113 (1992)
20. M. E. Walsh, Y. Hao, C. A. Ross, H. I. Smith, *J. Vac. Sci. Technol. B* **18**, 3539 (2000)
21. H. I. Smith, M. W. Geis, C.V. Thompson, H.A. Atwater, *J. Cryst. Growth* **63**, 527 (1983)
22. M. Farhoud, J. Ferrera, A.J. Lochtefeld, M.L. Schattenburg, C.A. Ross, H. I. Smith, J. Vac. Sci. Technol. B 17, 3182 (1999)
23. M. E. Walsh, *Nanostructuring Magnetic Thin Films Using Interference Lithography,* Master Thesis, MIT (2000)
24. B. D. Cullity, *Introduction to Magnetic Materials*, p67 (1972)
25. P .J. Flanders, *J. Appl. Phys.* **63**, 3940 (1988); K. O'Grady, V. G. Lewis and D. P. R. Dickson, *J. Appl. Phys.* **73**, 5608 (1993)
26. M. P. Sharrock, *IEEE Trans. Magn.* **35,** 4414 (1999)
27. D. Weller and A. Moser, *IEEE Trans. Magn.* **35,** 4423 (1999)
28. E. P. Wohlfarth, *J. Appl. Phys.* **29**, 595 (1958)
29. O. Henkel, *Phys. Stat. Sol.* **7**, 191 (1964)
30. G. Bottoni, D. Candolfo, A. Cecchetti, *J. Appl. Phys.* **81**, 3811 (1997)

Chapter 3

FABRICATION OF MAGNETIC PARTICLE ARRAYS USING BLOCK COPOLYMER LITHOGRAPHY

Periodic nanostructures of block copolymer provide a self-assembled template for nanolithography [1,2]. Combining the block copolymer templates and additive or subtractive methods, various nanoparticle arrays have been made. For example, Si, Ge, SiN_x, and GaAs nanodots have been made using etching or selective area growth based on spherical PS-PI or PS-PB templates [2-5]. Vertical arrays of Co nanowires, silica nanopillars and metal nanoporous or nanodot films have been electroplated or evaporated through cylindrical holes in PS-PMMA [6-11]. As/InGaAs/GaAs quantum dots and diamond dots have been made using thin films of PS-PVP (poly-2-vinylpyridine) micelles with gold particles loaded in the PVP domains [12,13].

The fabrication of nanoscale magnetic dot arrays has attracted considerable interest, both for fundamental studies of micromagnetism and for possible applications in high-density magnetic data storage. Single-domain magnetic particles are ideal for applications such as patterned recording media, in which each particle stores one bit according to its magnetization direction. In this chapter, we demonstrate a process to fabricate an array of magnetic dots from a thin film through successive etching steps, using an organic-organometallic block copolymer as a template. The fabrication process consists of an oxygen plasma treatment to convert the copolymer into a topographical template, four subsequent reactive-ion-etching (RIE) processes to transfer patterns from templates to hard masks and an ion beam etch to pattern magnetic thin films into discrete dot arrays. Arrays of Co, NiFe and a pseudo spin valve film were fabricated using this process. The magnetic dots are small enough to be single-domain magnetic particles and have a density of 2.3×10^{10} dots/cm^2. This method is versatile, and can be applied to patterning a wide variety of thin film materials into dot arrays.

3.1 Etching PS-PFS Thin Films in Oxygen Plasma

We used an organic-organometallic block copolymer, PS-PFS, as a lithographic mask and a subtractive method to pattern magnetic thin films. Because of the presence of Fe and Si, the organometallic PFS domains are considerably more resistant than the organic domains to an O_2 plasma [14,15], thus, high etching selectivity is obtained. The advantage of using PS-PFS is that the inorganic components, which enhance selectivity within the block copolymers, are inherent in our system, which eliminates the extra steps required if organic-organic block copolymers are used. In addition, applying a subtractive method for pattern transfer allows the widest control of the properties of the magnetic materials through thin film deposition, which is difficult to do using an additive method on the nanoscale. This section describes the optimization of the conversion of PS-PFS thin film into topographical templates for making magnetic particles.

A PS-PFS block copolymer with 21kg/mole PS and 91kg/mole PFS (SF 91/21) was used as an example to demonstrate our method of patterning a magnetic thin film. The molar mass of the block copolymer is chosen according to the phase diagram to give 16 volume percent of PFS spheres embedded in a PS matrix [16]. Spherical PS-PFS has a stable morphology and is compatible with the substrate, which is essential for a robust process. When a 1% - 3% toluene solution of SF 91/21 is spun onto a substrate and annealed at 180 °C, it forms a monolayer of close-packed PFS spheres in a PS matrix. The spheres appear to be about 35nm in diameter and have a spacing of 56 nm. These dimensions allow us to fabricate a high-density array of magnetic dots, which are expected to be single magnetic domains.

The lithographic template is formed by reactive ion etching (RIE) of the block copolymer film in an O_2 plasma. This oxidizes the exposed PS matrix and removes it completely, leaving the PFS spherical domains behind as illustrated in figure 3.1.

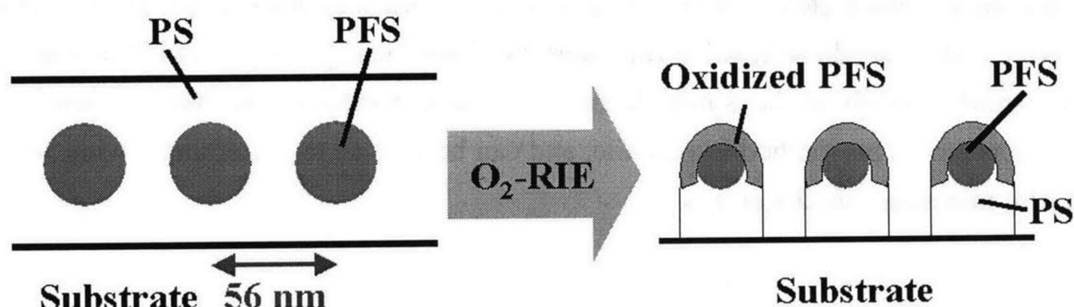

Figure 3.1 Structure of PS-PFS thin film before / after O_2-RIE. Unprotected PS forms volatile species and is removed by oxygen plasma. PFS reacts with oxygen plasma and then forms a protective layer which limits further etching.

The effects of the O_2 plasma on the PFS have been studied [14]. The O_2-RIE process consists of both ion-assisted chemical reactions and physical sputtering. The ion-assisted chemical reactions lead to partial oxidation of the PFS domains, in which the silicon and iron in the PFS form a silicon-iron oxide. The thickness of the polymer layer that reacts with the plasma is around 10 nm estimated by the depth-profiling auger electron spectroscopy.

To quantify the reaction of the oxygen plasma with PFS, we used x-ray photoelectron spectroscopy (XPS) to determine and quantify the surface composition and chemical states of a PFS *homopolymer* etched in an O_2 plasma. The characterization was done with a Kratos Axis Ultra X-ray Photoelectron Spectrometer using an aluminum source with input power of 225W (15KV and 15mA). An oxygen 1s peak appears in the oxidized PFS, and the binding energy of the silicon 2p and iron 2p peaks increases shown in figure 3.2, indicating that the PFS homopolymer is partially converted to an iron-silicon oxide. The surface atomic concentration can be estimated from the XPS peak area and relative sensitivity factor for each element. The data shows that the concentrations of oxygen, silicon and iron increase while the carbon concentration decreases after O_2-RIE treatment. The surface atomic concentrations of the elements in PFS homopolymers are listed in table 3.1.

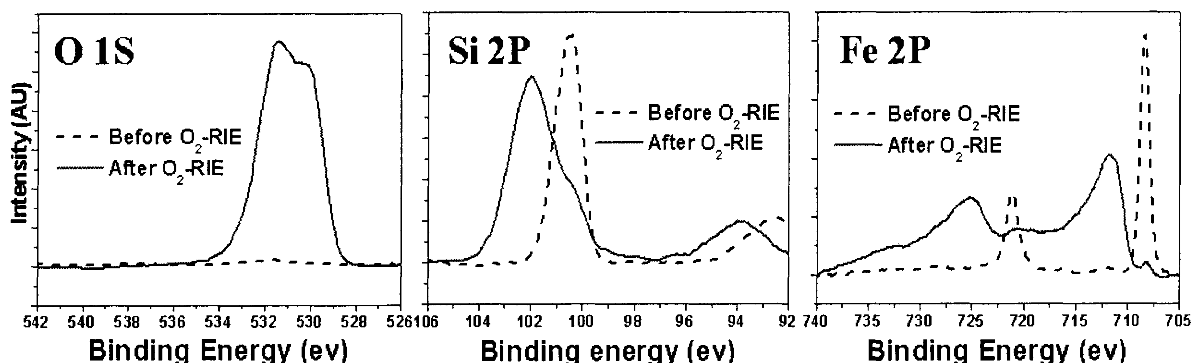

Figure 3.2 XPS spectrum of PFS homopolymer thin film before and after O_2-RIE process.

In the PS-PFS thin film, this iron-silicon oxide is believed to form a protective layer around the PFS domains, reducing their etch rate during the O_2-RIE process, and leading to good topographic contrast in the oxidized PS-PFS block copolymer. The key to utilizing such a film as a lithographic mask is to completely remove the PS matrix to leave PFS features with a large aspect ratio (height/width) and straight sidewalls. This can be optimized by choice of etching time and bias voltage.

The endpoint of the block copolymer O_2-etching process was determined from ellipsometry

and SEM measurements. Ellipsometry provides information of the refractive index of the polymer thin film along the O_2-RIE process. Figure 3.3 shows that there is little change in the refraction index of PFS homopolymers during the etching time. Compared to the homopolymer, the refraction index of PS-PFS decreased linearly with etching time which mainly results from removal of PS. At the point where PS had been etched down to the substrate, the refractive index stopped changing and this is the end point of the etching.

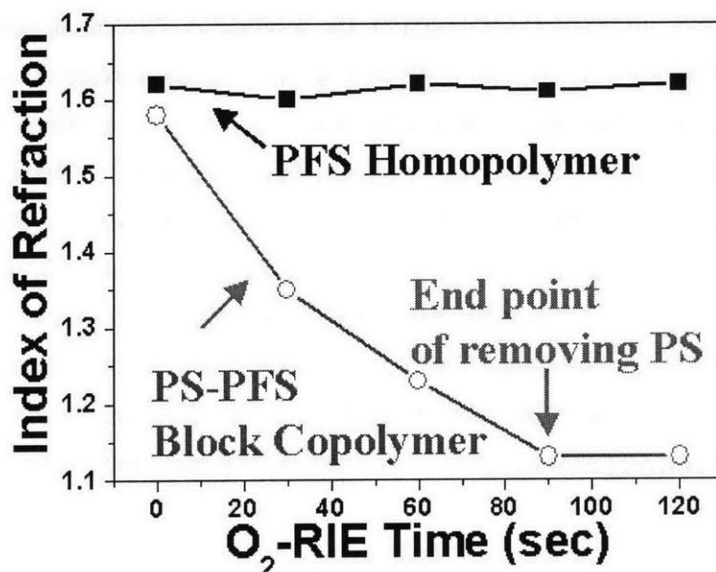

Figure 3.3 Index of refraction of PFS homopolymer and PS-PFS block copolymer vs. O_2-RIE etching time, from ellipsometry.

Figure 3.4a shows a cross-sectional SEM micrograph of the partially etched PS-PFS block copolymer film. It appears that about half the thickness of the PS has been removed, and oxidized PFS posts can be seen emerging from the remaining PS matrix. The original size and spacing of the close-packed spherical nanostructure is preserved through the etching process. Figure 3.4b-d shows the end-point SEM micrographs for different etching conditions. In these cases, there are good correlations between the endpoint detected from SEM and from ellipsometry. Therefore, ellipsometry and SEM provide endpoint detection methods for removing the exposed PS, which allows the etching of the PFS domains to be minimized, thus maximizing the aspect ratio of the posts.

In addition to controlling the etching time, the shape and uniformity of the remaining PFS features were optimized by adjusting the DC bias used during RIE. In the O_2-RIE process, there is a competition between oxide formation by the ion-assisted chemical reaction and removal of material through physical sputtering, which leads to a change both in the morphology of the remaining PFS features, and in the relative etch rates of the PS and PFS,

as a function of DC bias. At higher bias there was a decrease in the etching selectivity between PS and PFS. 60V DC bias gave the greatest difference in etch rates (PS:PFS = 8:1), 100V DC bias gives less selectivity (5:1) and 200V DC bias gives the least selectivity (2:1). This result can be explained by comparing the effects of bias on both etching and oxidation of the PFS. From XPS measurements on the PFS homopolymer (table 3.1), it appears that under higher bias, ion-assisted oxidation is faster and more of the PFS is converted into the nonvolatile iron-silicon oxide. This would by itself reduce the removal rate of the PFS. However, under higher bias, physical sputtering becomes the dominant mechanism for material removal, leading to higher etch rates and a decrease in the selectivity between PS and PFS.

Elements	Unetched PFS	60V O_2-RIE	200V O_2-RIE	60V O_2-RIE then 150V CHF_3-RIE
C	85.7	29.3	18.9	48
O	0.6	46.8	53.0	6
Si	6.0	8.5	10.9	3
Fe	7.7	15.4	17.2	4
F	-	-	-	39

Table 3.1 Atomic concentration of the PFS homopolymer after various RIE treatments, from XPS data. Higher etching bias results in better conversion from PFS polymer to oxidized PFS, however, a higher bias also enhances physical sputtering that removes both PS and PFS without selectivity.

The SEM micrographs of Figure 3.4b-d show the nanostructures formed under different bias conditions. Feature diameters were measured at mid-height from the SEM images. At 200V DC bias, tapered features with an average base diameter of 22 nm are formed (Figure 3.4b). At 100V bias, cylindrical features with straight sidewalls were formed, with an average diameter of 27 nm (Figure 3.4c). At 60V, the features have straight sidewalls and improved uniformity, and an average diameter of 35 nm. Therefore, relatively low bias conditions must be used in order to obtain anisotropic etching to preserve the straight sidewalls of the features, while maintaining a high selectivity between the PS and PFS domains. Similar trends have been observed in surface image resist systems, where the silylation layer was destroyed by a high power flux [17]. This optimization of the O_2-RIE process enables us to make lithographic masks with arrays of posts of 30 nm – 40 nm in height and 20 nm – 35 nm in diameter from a single spin-coated block copolymer film. In addition to changing the etching conditions, the feature size can be adjusted by changing

the molar mass of the block copolymer.

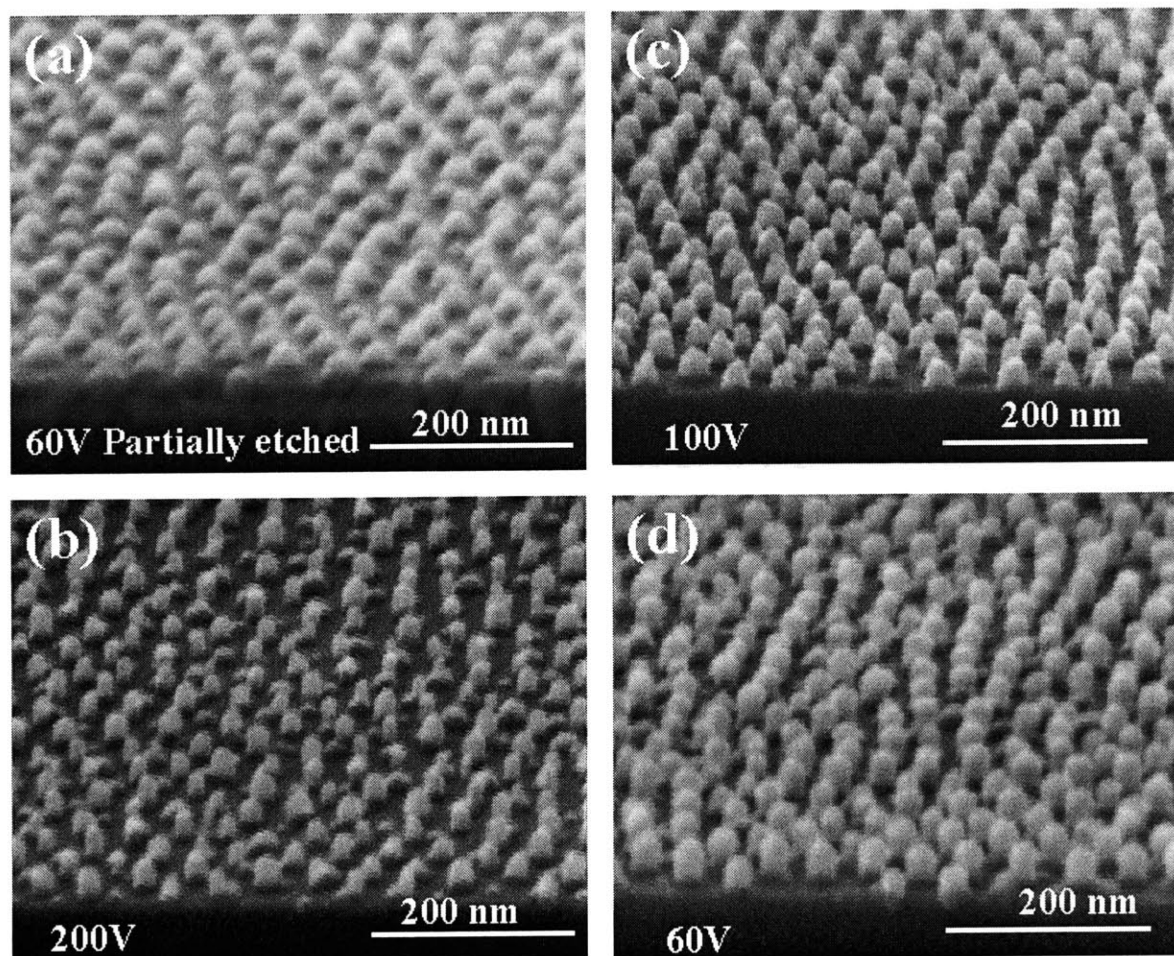

Figure 3.4. Tilted SEM micrographs of O_2-RIE etched PS-PFS copolymer. (a) PS-PFS etched partway through the PS. A layer of PS is still left on the substrate, with PFS domains protruding. (b) PS- PFS etched completely through the PS matrix, using 200V DC bias. (c) PS-PFS etched completely, using 100V DC bias. (d) PS-PFS etched completely, using 60V DC bias.

3.2 Pattern Transfer from Block Copolymer Masks to Tungsten Hard Masks

The next step is to transfer the template pattern into a magnetic film using intermediate masking layers. Magnetic materials such as iron, nickel, and cobalt cannot be etched using an RIE process because they do not form volatile products [18]. Hence, to transfer the pattern from the template into the magnetic layer, we developed a multilayer scheme which uses a combination of reactive ion etching and ion beam etching (ion milling). Figure 3.5 summarizes the materials, procedures and intermediate nanostructures for this process. The multilayer consists of chromium (Cr), cobalt (Co), tungsten (W), then silica, with each layer 5 ~ 50 nm thick. (The Cr serves as an adhesion layer for the Co.) They were electron-beam evaporated onto unheated substrates using an Airco Temescal BJD 1800 E-Beam Evaporator. The pattern in the block copolymer template is transferred sequentially through the silica, then the W, then the Co. W was chosen to provide a hard-mask for ion-beam etching of the Co. The silica layer was introduced to improve the pattern transfer from the block copolymer template into the W. The patterned silica layer forms a robust template, which can be used to pattern a variety of materials including W, other metals, or other polymeric layers.

Figure 3.6a is an SEM micrograph of the lithographic mask (etched polymer film) on top of the multilayer stack, which corresponds to the schematic structure in figure 3.5b. A CHF_3-RIE was used to transfer the pattern from the lithographic mask to the silica. We saw earlier from XPS that after etching a PFS homopolymer with O_2 then CHF_3, the surface becomes richer in fluorine (table 3.1). This indicates that the CHF_3 forms a passivation layer on the oxidized PFS. Due to the protection of the passivation layer, there is good RIE selectivity between the oxidized PFS lithographic mask and the silica using CHF_3 gas [19]. The selectivity is silica: oxidized PFS = 10:1, which ensures the preservation of the PFS pattern during pattern transfer into the silica. The result of etching a 50 nm thick silica layer with CHF_3 RIE is shown in figure 3.6b. Tall pillars of silicon oxide capped with oxidized PFS are seen, with average height of 80 nm, corresponding to the schematic structure in figure 3.5c. The high aspect ratio of these features should be noted.

A CF_4 and O_2 gas mixture (CF_4: O_2= 85: 15) was subsequently used to etch through the W layer using the silica as a mask. For this gas mixture, the selectivity is W: silica = 3:1. The 50 nm thick silica mask was used successfully to pattern a 20 nm thick W film, preserving the lateral dimensions of the features. Figure 3.6c shows the structures after CF_4+O_2-RIE. After patterning the W, the silica and any residual oxidized PFS were removed by an ashing

process with a high pressure CHF_3 plasma (figure 3.5e). Figure 3.6d shows a 20 nm thick patterned W film on top of a Co layer after removal of the silica and oxidized PFS caps. The pattern of PS-PFS has been successfully transferred to the W through four high-selectivity RIE etching processes. Detail RIE conditions are listed in section 2.2.2.

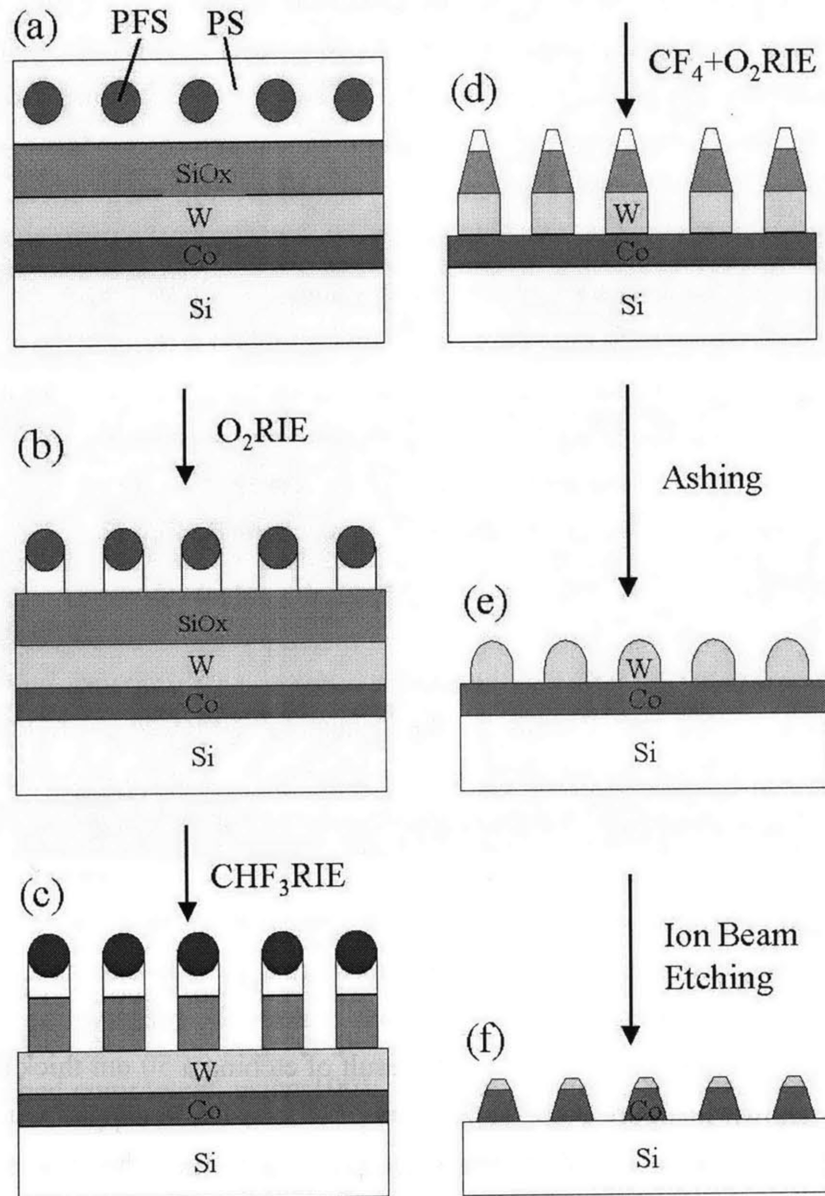

Figure 3.5 Fabrication process of the Co dot array using block copolymer lithography. (a) A block copolymer thin film on a multilayer of silica, W and Co. (b) The block copolymer lithographic mask is formed through O_2-RIE process. The PFS domains are partly oxidized. (c) The silica film is patterned using CHF_3-RIE. (d) The W hard mask is patterned using CF_4+O_2-RIE. (e) Removal of silica and residual polymer by high pressure CHF_3-RIE. (f) The Co dot array is formed using ion beam etching.

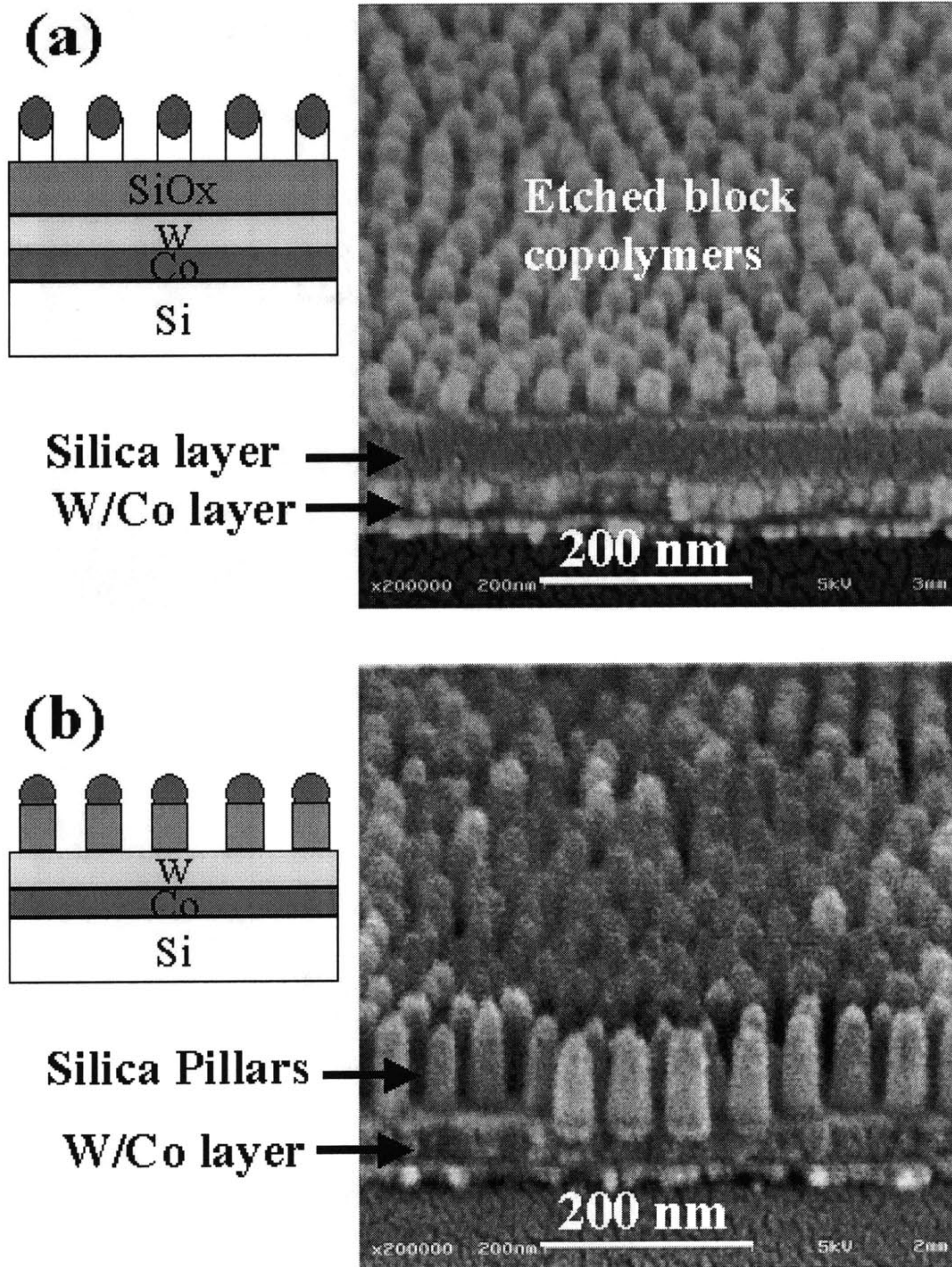

Figure 3.6 Tilted SEM micrographs of the intermediate stages of lithographic processing. (a) An O_2-RIE treated block copolymer thin film on a multilayer of silica, the metallic films and the silicon substrate. (b) Pillars of silicon oxide capped with oxidized PFS after CHF_3-RIE. Straight, vertical sidewalls of polymer pillars and silica pillars are the evidence for high etching selectivity and good control of the RIE processes.

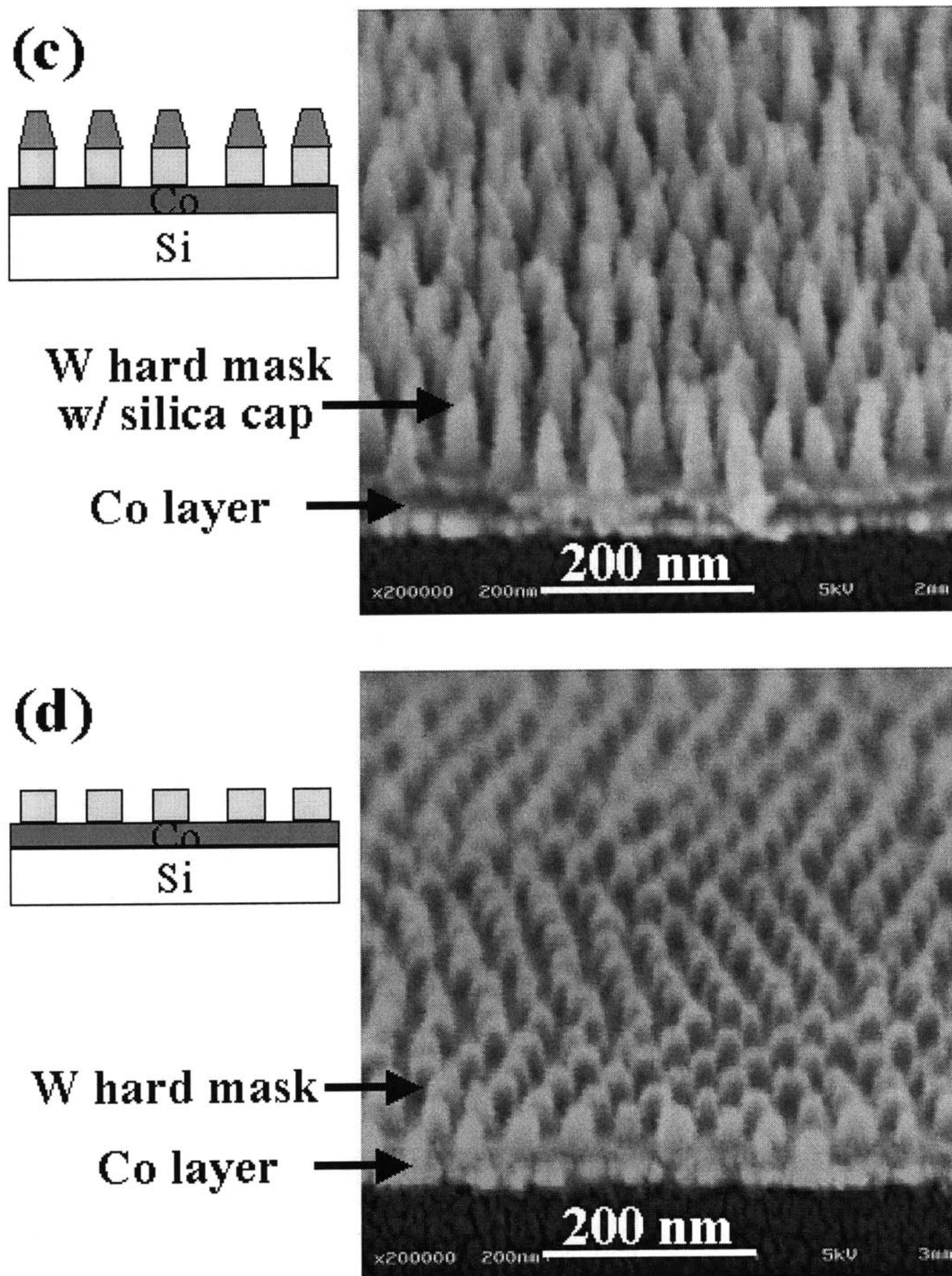

Figure 3.6 Tilted SEM micrographs of the intermediate stages of lithographic processing. (c) Dots of W capped with silica and residual polymer after CF_4+O_2 -RIE. (d) W hard mask on top of a Co layer after ashing away the cap with high pressure CHF_3 plasma. The dimensions of the W hard mask dots are close to those of the polymer dots in figure 3.6a, which indicates that the transfer of the nanostructure from PS-PFS thin film to the metal hard mask was successful.

3.3 Ion-Beam Etching Process for Patterning Magnetic Thin Films

Finally, ion beam etching, a purely physical sputtering process, was used to pattern the various magnetic thin films with thickness from 5 nm to 20 nm, with the 12 nm ~ 20 nm-thick W dots serving as a hard mask. The sputtering rate is related to energy transfer from the bombarding gas ions to the substrate material: if there is a large difference in atomic mass, energy transfer will be minimized and the film will be etched slowly [20]. Because of its high atomic mass and process compatibility with silica, W (184 amu) is a good choice as a hard mask for patterning magnetic materials such as Fe (56 amu), Co (59 amu) and Ni (59 amu) using ion beam etching. The ion beam etching conditions are described in section 2.2.3.

Good selectivity between W and magnetic material in the ion-beam etching is essential for patterning nanoscale magnetic dots. Both Ar and Ne ion beam etching have been used to transfer structure from W hard masks to magnetic thin films. The selectivity between W and Co can be estimated from the atomic mass of materials and plasma gas [20]. The larger the mass difference between high-energy ions and target materials, the smaller the etching rate. The selectivity between W and Co is 1.4:1 in Ar and 2.2:1 in Ne [18]. Figure 3.7 is an example of results from pattering 10 nm thick Co film covered by 20 nm thick, 35 nm diameter W hard mask dots in two different plasmas. The saturation magnetization (Ms) of the Co thin film changes with ion-beam etching time under Ar ion beam etching and Ne ion-beam etching. In both cases, the Ms, which is proportional to the volume of Co, decreases linearly with time during the first part of ion-beam etching as the Co directly exposed to the ion beam is removed. The Ar ion beam etches Co faster than the Ne ion beam and the end-point of the etching is approximately 60 sec for Ar ion-beam etching and 100 sec for Ne ion-beam etching, at which a discrete Co dot arrays are formed. Such discrete dots correspond to a constant value of Ms because no more Co can be removed under the W hard mask. Further etching results in a second slower decrease in magnetization with time as the diameter of the W-capped Co features is decreased. It is noted that the Ms value stays constant for a longer time in Ne compared to Ar. The Ar plasma induces more faceting in the etching process and leads to faster diameter decrease in the W hard mask. Therefore, the higher selectivity between Co and W obtained by using Ne leads to wider process window and better control of the etching process. Figure 3.8 shows SEM micrographs of the Co dot arrays from Ar and Ne ion-beam etching. If ion-beam etching is performed using Ar, the W mask erodes leading to small, faceted Co dots as shown in figure 3.8a. Using Ne is preferable to using Ar, leading to more uniform, flatter-topped features as shown in figure 3.8b.

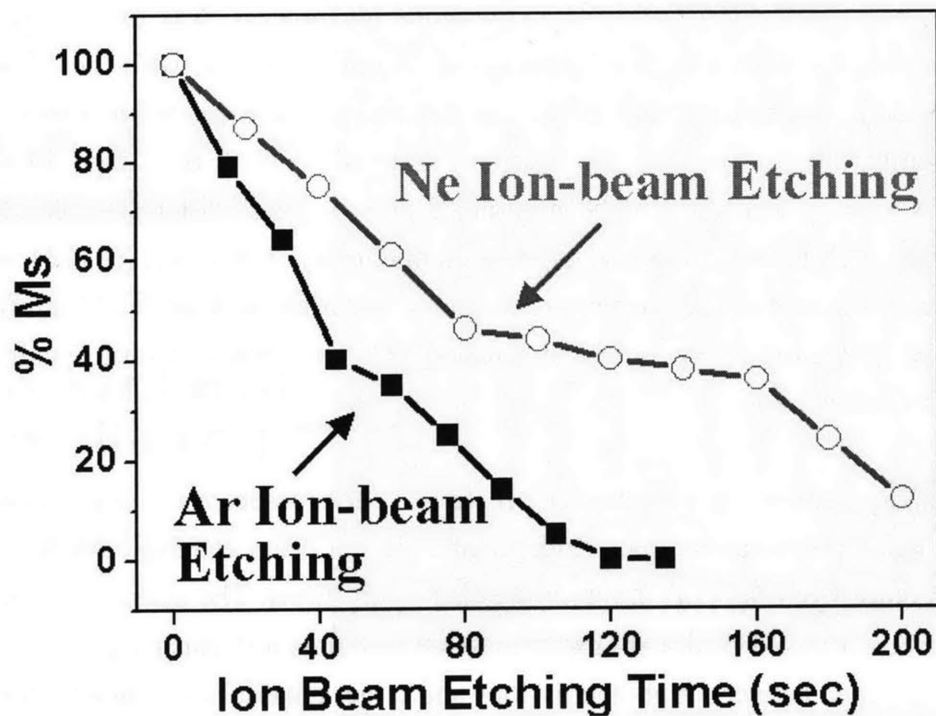

Figure 3.7 The saturation magnetization (Ms) as a function of Ar and Ne ion-beam etching time. Ms decreases due to the removal of cobalt.

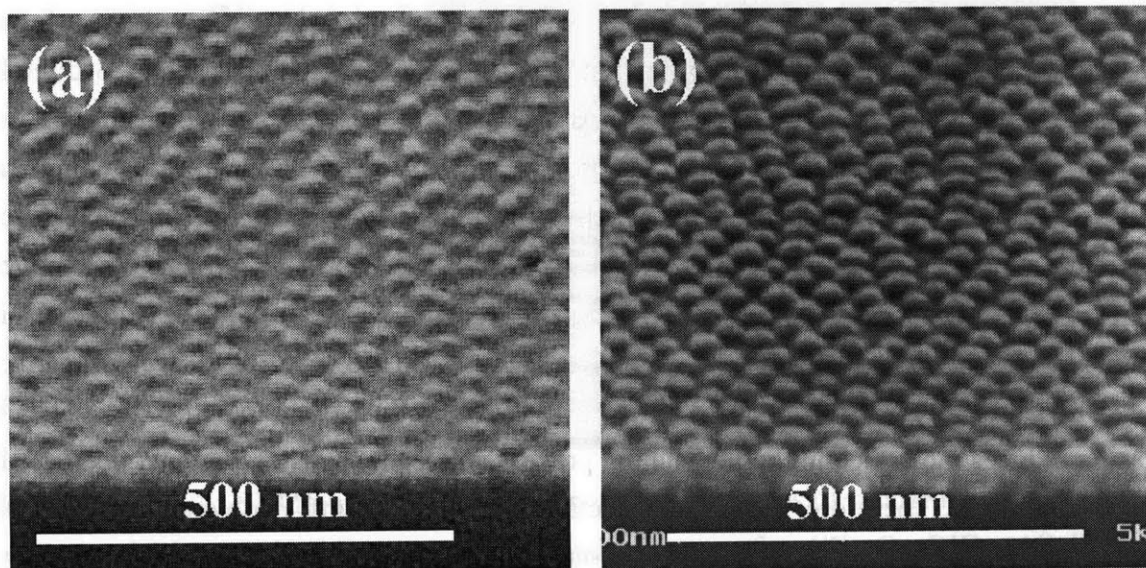

Figure 3.8 Tilted SEM micrographs of the W-capped Co dot array produced by (a) Ar, and (b) Ne ion-beam etching. Co dot arrays are more uniform and less faceted using Ne ion beam etching.

It is difficult to determine the end point of ion-beam etching of the magnetic particle arrays using structural characterization tools such as SEM and AFM because the structures are small. Alternatively, since the magnetic properties of particles are size and shape dependent and very sensitive to the patterning process, measurements of magnetic properties during the etching process provide information about the structural evolution of the magnetic thin film. Figure 3.9 shows how the in-plane coercivity (H_c) correlates to the reduced magnetization as Ne ion-beam etching proceeds. Four Co thin films with different thickness (5 nm, 10 nm, 15 nm, 20 nm) basically follow similar trend. The unpatterned cobalt films had a coercivity of 8-18 Oe. The coercivity gradually increases in the initial stages of etching, during which the unprotected Co is being removed to produce a corrugated surface shown schematically in the figure. The increase in Hc is due to the increased roughness of the still continuous cobalt film, which pins domain wall motion in plane. The peak in H_c occurs when around 40% of M_s remains, and discrete Co dots have been formed. Further etching causes a decrease in H_c as the diameter of the dots slowly decreases. The peak coercivity varies between 130 Oe for the 5 nm thick Co dots and 220 Oe for the 15 nm

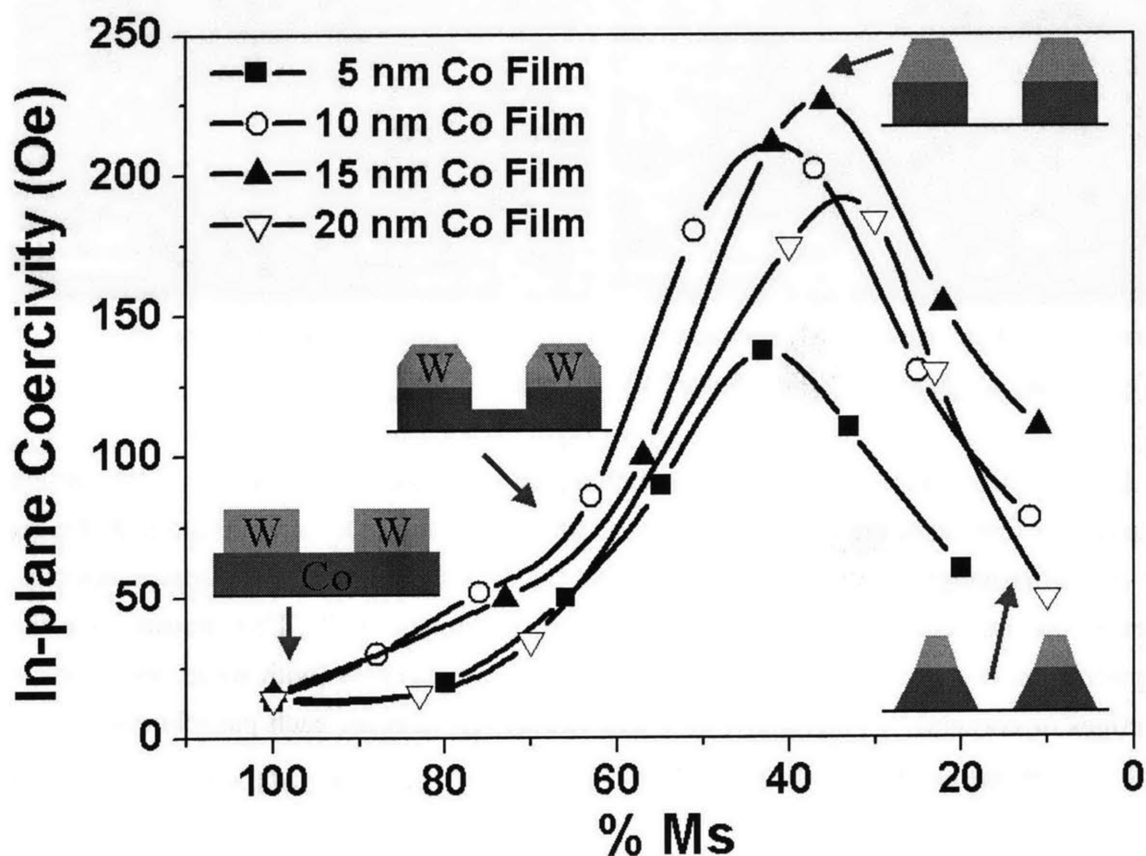

Figure 3.9 In-plane coercivity vs. remaining magnetization during the ion-beam etching process of Co thin film of different thickness. The maximum coercivity refers to the formation of discrete dot arrays.

thick Co dots, but the position of the peak, at 40 % remaining M_s, is similar for the four samples, and is consistent with the surface coverage of a close-packed array of 35 nm diameter disks with 56 nm period.

Pseudo-spin-valve (PSV) dot arrays and 5 nm, 10 nm, 15m, and 20 nm thick NiFe dots have been made using the same block copolymer lithography process. Figure 3.10 demonstrates the plan-view SEM micrographs of 15 nm NiFe dots and PSV (CoFe 3.3 nm / Cu 6.0 nm / NiFe 4.5 nm) dots. Both micrographs show locally close-packed dot arrays with 34 nm diameter and 56 nm center-to-center spacing. Similar to the Co dots, these NiFe dots and PSV dots made from block copolymer lithography are thermally stable at room temperature.

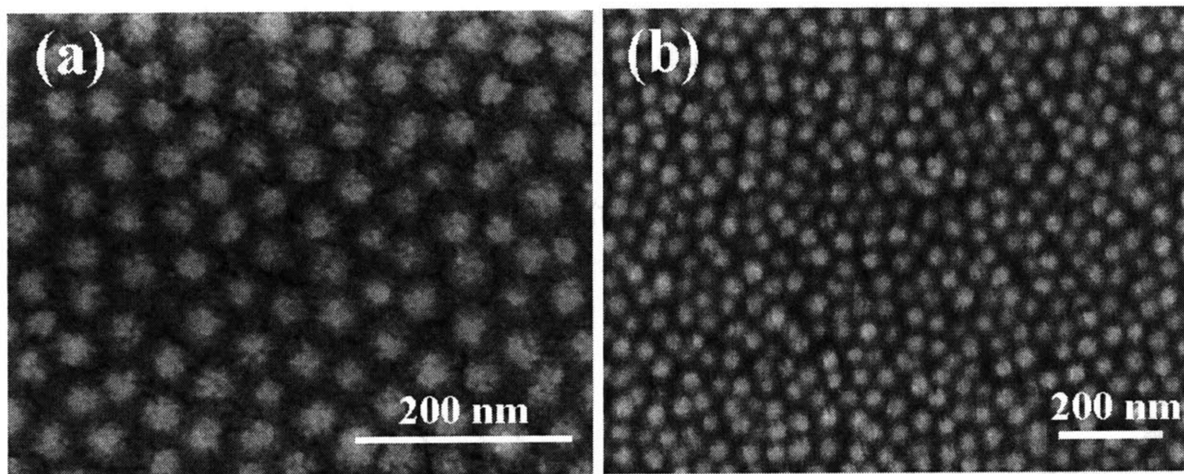

Figure 3.10 Plan-view SEM micrographs of (a) 15nm thick NiFe dots, and (b) dots of CoFe 3.3 nm / Cu 6.0 nm / NiFe 4.5 nm PSV structures.

The Co and NiFe dots at the end point of etching have diameters of 25 nm to 35 nm, which is equal to a few times the magnetic exchange length of 7 nm in Co and 20 nm in NiFe. At this size, micromagnetic modeling predicts that the dots should be single-domain particles, because the particles are too small to support a domain wall. This means that the magnetization is approximately uniform within these Co particles (with some deviations at the edges or corners)[21]. Potentially, in a data storage application, each particle could store one bit according to its magnetization direction.

In conclusion, a series of Co and NiFe dot array of different thickness and PSV dot arrays have been fabricated using self-assembled block copolymer lithography. There are several advantages to the fabrication process that we have developed. The process allows

high-density arrays of dots to be fabricated: the magnetic particle density illustrated here is $2.3\times10^{11}/in^2$. The process can pattern large areas, such as the 10 cm diameter wafers used in this study. The process can be applied very generally to pattern a variety of thin-film materials into dot arrays. In addition, particle sizes and spacings can be controlled through the choice of the block copolymer template and etching conditions. Therefore, magnetic properties such as coercivity, magnetostatic interactions, and thermal stability, which determine the switching behavior of the magnetic elements, are adjustable in this fabrication system through both the geometric parameters of the particle array and the composition and growth of the magnetic thin film.

References

1. P. Mansky, P. Chaikin, E.L. Thomas, *J. Mater. Sci.* **30**, 1987 (1995)
2. M. Park, C. Harrison, P. M. Chaikin, R. A. Register, D. H. Adamson, *Science* **276**, 1401 (1997)
3. C. Harrison, M. Park, P. M. Chaikin, R. A. Register, D. H. Adamson, *J. Vac. Sci. Technol. B* **16**, 544 (1998)
4. R. R. Li, P.D. Dapkus, M. E. Thompson, W. G. Jeong, C. Harrison, P. M. Chaikin, R. A. Register, D. H. Adamson, *Appl. Phys. Lett.* **76**,1689 (2000)
5. M. Park, P. M. Chaikin, R. A. Register, D. H. Adamson, *Appl. Phys. Lett.* **79**, 257 (2001)
6. T. Thurn-Albrecht, J. Schotter, G. A. Kastle, N. Emley, T. Shibauchi, L. Krusin-Elbaum, K. Guarini, C. T. Black, M. T. Tuominen, T. P. Russell, *Science*, **290**, 2126 (2000)
7. K. Liu, S. M. Baker, M. Tuominen, T. P. Russell and I. K. Schuller, *Phys. Rev. B* **63**, 060403R (2001)
8. T. Shibauchi, L. Krusin-Elbaum, L. Gignac, C. T. Black, T. Thurn-Albrecht, T. P. Russell, J. Schotter, G. A. Kastle, N. Emley, M. T. Tuominen, *J. Mag. Mag. Mater.* **226**, 1553 (2001)
9. Z. Q. Lin, D. H. Kim, X. D. Wu, L. Boosahda, D. Stone, L. LaRose, T. P. Russell, *Adv. Mater.* **14**, 1373 (2002)
10. K. Shin, K.A. Leach, J. T. Goldbach, D. H. Kim, J. Y. Jho, M. Tuominen, C. J. Hawker, T. P. Russell, *Nano Lett.* **2**, 933 (2002)
11. M. Bal, A. Ursache, M. T. Touminen, J. T. Goldbach, T. P. Russell, *Appl. Phys. Lett.* **81**, 3479 (2002)
12. J .P. Spatz, T. Herzog, S. Mobmer, P. Ziemann, M. Moller, *Adv. Mater.* **11**, 149 (1999)
13. B. Koslowski, S. Strobel, T. Herzog, B. Heinz, H. G. Boyen, R. Notz, P. Ziemann, J .P. Spatz, M. Moller, *J. Appl. Phys.* **87**, 7533 (2000)
14. R. G. H. Lammertink, M A. Hempenius, V. Z. H. Chan, E. L. Thomas, G. J. Vancso, *Chem. Mater.* **13**, 429 (2001)
15. R. G. H. Lammertink, M A. Hempenius, J. E. van den Enk, V. Z. H. Chan, E. L. Thomas, G. J. Vancso, *Adv. Mater.* **12**, 98 (2000)
16. R. G. H. Lammertink, M.A. Hempenius, E. I. Thomas, G. J. Vancso, *J. Poly. Sci. Poly. Phys.* **37**, 1009 (1999)
17. J. Munoz and C. Dominguez, *J. Vac. Sci. Technol. B* **13**, 2179 (1995)
18. M. E. Walsh, Y. Hao, C. A. Ross and H. I. Smith, *J. Vac. Sci. Technol. B* **18**, 3530 (2000)
19. D. L. Flamm and G. K. Herb, *Plasma Etching, An Introduction*, Academic Press, San Diego (1988)
20. M. Ohring, *The Materials Science of Thin Films*, Academic Press, New York (1992)
21. M. Schabes, *J. Magn. Magn. Mats.* **95**, 249 (1991)

Chapter 4

PROPERTIES OF MAGNETIC DOT ARRAYS

The magnetic properties of nanoscale magnetic particle arrays are a subject of current interest, both from a fundamental point of view and for potential applications. Recent advances in nanofabrication technology have opened up the possibility to study deep submicron magnetic particle arrays and magnetism at a small scale [1,2]. Self-organizing materials form large-area periodic nanostructures and provide simple and low-cost templates for nanofabrication. Various magnetic nanostructures such as nanoparticles, nanorods, nanowires and anti-dots have been made using anodized alumina [3], colloidal crystals [4], and block copolymers [5,6,7]. The dimensions of these templates are typically in the deep submicron region, which naturally gives high-density and close packed magnetic particle arrays. These arrays can be used for data storage applications or magnetotransport devices. Studying the magnetic behavior such as magnetization reversal of the particle arrays is important both for understanding the nanoscale magnetism and further optimizing the array structures for device applications.

This chapter presents a study of magnetic behavior of patterned magnetic dot arrays from block copolymer lithography. Single layer dots of Co, NiFe, and two layer dots of CoFe/Cu/NiFe pseudo-spin-valve are made from polystyrene-polyferrocenyldimethylsilane templates. The hysteresis loops and scan-rate dependent coercivities are measured and compared to show the magnetic switching behavior of the arrays. The trend of coercivity, switching field distribution and the switching volume of dot arrays with different thickness and materials composition will be discussed. All samples show thermally activated reversal and inter-particle magnetostatic interaction. The behavior of single layer dots is compared with that of two-layer dots, in which magnetostatic interactions exist both within and between the dots.

4.1 Magnetic Dot Arrays from Block Copolymer Lithography

Magnetic dots of Co, NiFe and CoFe/Cu/NiFe pseudo-spin-valves (PSV) are fabricated through block copolymer lithography. Polystyrene-*b*-Polyferrocenyldimethylsilane block copolymers were used as lithographic templates for patterning the magnetic thin films. Co

and NiFe films with thicknesses of 5 – 20 nm were deposited onto oxidized silicon wafers by electron-beam evaporation. A CoFe/Cu/NiFe PSV thin film was sputtered in a UHV chamber. The magnetic films were then coated with an etch mask consisting of 20 nm W followed by 50 nm silicon oxide, deposited using electron-beam evaporation. A solution of PS-PFS 91/21 was spin-cast on to the SiO_2 / W/ magnetic material multilayer stack and annealed to spontaneously form a close-packed monolayer of PFS spheres embedded in a PS matrix. Four successive reactive ion etching (RIE) processes were used to remove the PS matrix and then to transfer the PFS dot pattern into the oxide, then the W hard mask layer [1]. Finally, arrays of discrete magnetic dots were produced by ion-beam etching the magnetic film in a neon plasma using the W hard mask. The Co, NiFe and PSV dot arrays are formed using the same polymer templates and pattern transfer process, hence, have the same size and geometry. This provides us a basis to compare the magnetic behavior of dot arrays of different thickness and material composition.

Uniform Co dot arrays of different thickness are shown in figure 4.1. The average diameter of dots in these arrays is 34 nm. The average center-to-center spacing is 56 nm and this gives a density of 2.38×10^{11} magnetic particles /in^2. The dots have uniform height (thickness) and diameter. The heights of dots are uniform because the thickness of magnetic thin film is well controlled by the evaporation process. The lateral dimensions of the dot arrays defined by block copolymers are preserved since the W hard mask provides good etch selectivity to the magnetic layer. Slightly tapered sidewalls are observed in the thicker dots due to the faceting effect of longer ion-beam etching time.

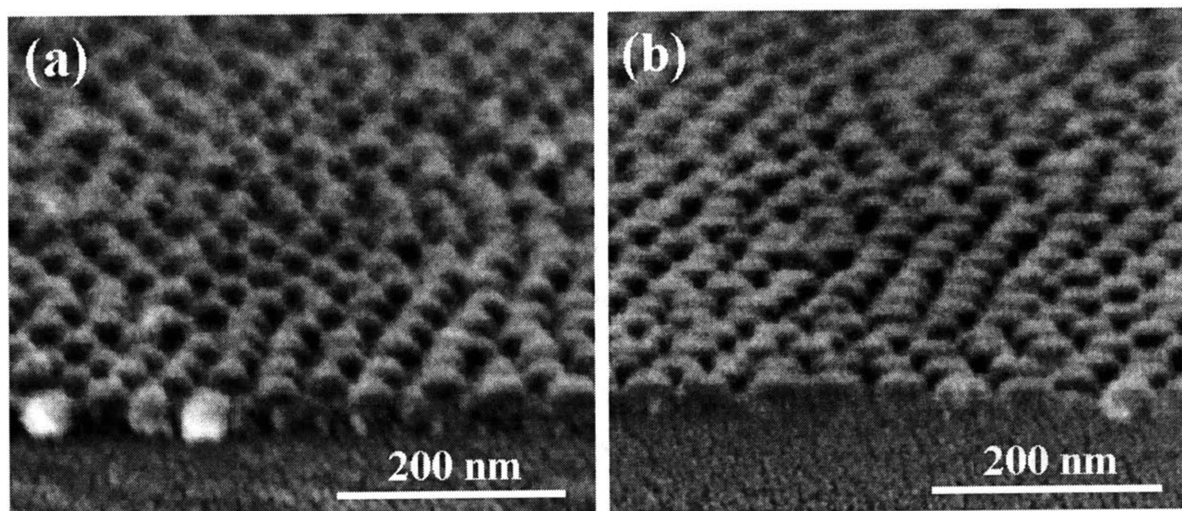

Figure 4.1 SEM cross-section micrographs of (a) 15 nm thick Co dot arrays and, (b) 5 nm thick Co dot arrays.

4.2 Hysteresis Loops of Single-layer Dot Arrays

Co and NiFe dots were made with 34 nm diameter and different thickness (5 nm, 10 nm, 15nm and 20 nm). Before patterning, the Co thin film has a coercivity of 8 Oe to 18 Oe and NiFe thin film has a coercivity of 5 Oe to 14 Oe. After patterning, the in-plane loops of these disk-like magnetic elements have high remanence while the out-of-plane loops have low remanence and saturate at high fields, indicating that the in-plane direction is the easy axis.

Figure 4.2 shows the in-plane hysteresis loops of arrays of discrete Co and NiFe dots. The in-plane coercivity H_c of Co and NiFe single-layer dot arrays varies from 30 Oe for 5 nm thick NiFe dots to 228 Oe for 15nm thick Co dots. Typically, the coercivity of Co and NiFe dot arrays increase as the dot thickness increases. Ideally, the in-plane coercivity of a perfect circular dot of this size would be close to zero and the remanence would be high, because the magnetization can rotate in plane. For larger circular dots, vortex configurations are stable because demagnetization energy is larger than the exchange energy. The vortex state gives a hysteresis loop with zero remanence and zero coercivity. Single domain states are stable in the circular dots if the dots is very thin and has small diameter compared to the exchange length. These single domain circular dots typically switch at very low field (few Oe) [8]. The dot arrays made from block copolymer lithography show higher coercivities than that of circular dots.

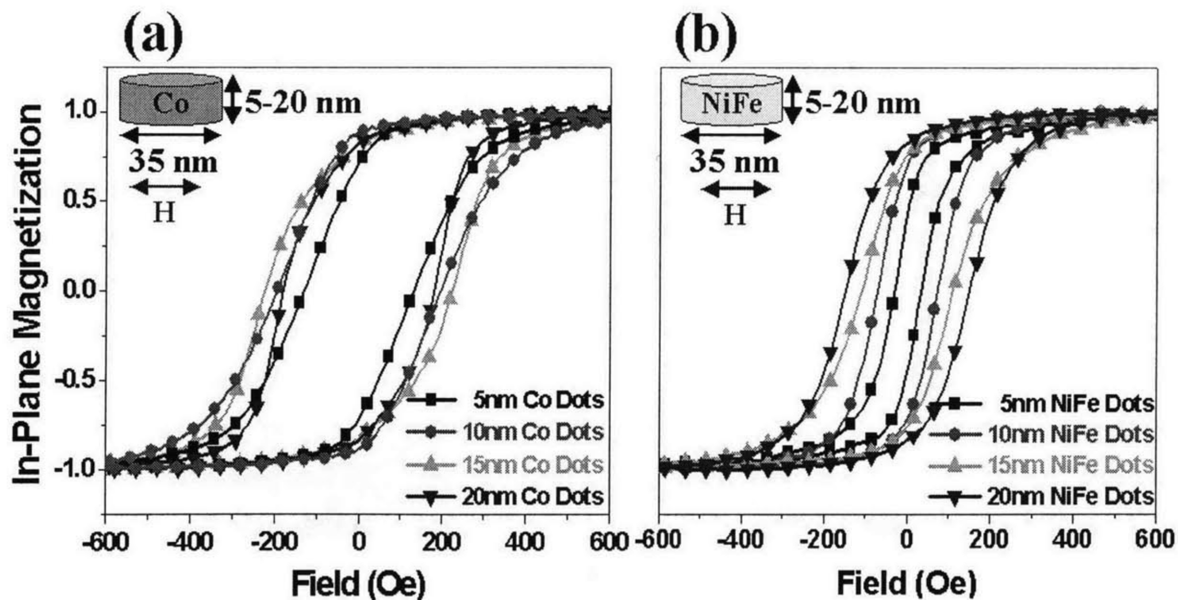

Figure 4.2 The in-plane hysteresis loops of single-layer (a) Co dot arrays and, (b) NiFe dots arrays with dot thickness from 5 nm to 20 nm.

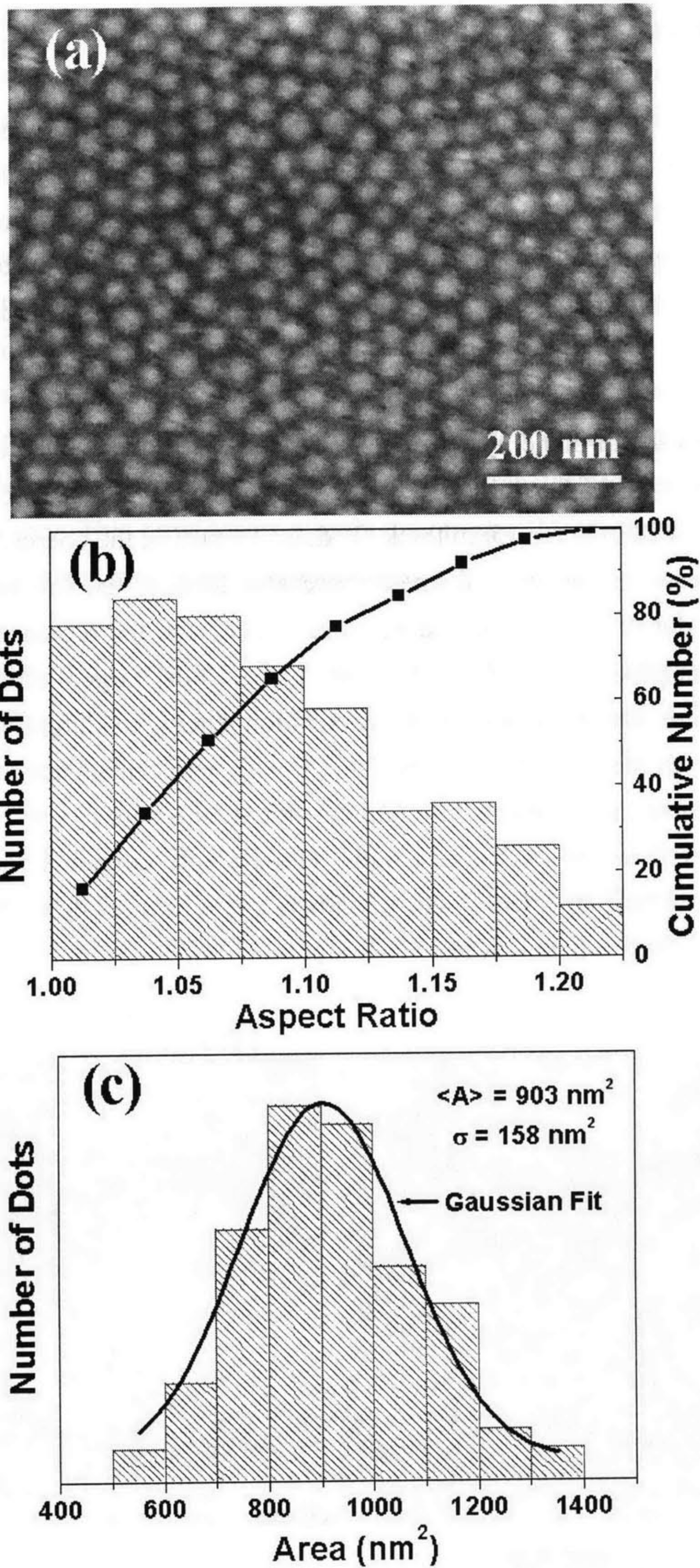

Figure 4.3 (a) Plan-view SEM micrographs of 15 nm thick Co dot arrays. (b) The aspect ratio distribution of the Co dots. (c) The size distribution of Co dots.

Figure 4.3a shows plan-view SEM of arrays of 15 nm thick Co dots. The dots are locally close-packed. The dot size and shape of were characterized by the aspect ratios (ellipticities) and particle size distribution within the magnetic dot arrays. Statistical results found from analyzing 400 magnetic particles are shown in figure 4.3b and 4.3c.

These single-layer dots are not perfectly circular. Most magnetic dots are elliptical. The elliptical shapes mainly come from imperfections in the fabrication process. The distribution of aspect ratios (the ratio of the major axis length to the minor axis length) of the magnetic dots is shown in figure 4.3b. The average aspect ratio of the dot arrays is 1.06 and 80% of the dots have aspect ratios between 1 and 1.15. The effects of shape anisotropy can be estimated by considering the shape anisotropy of a triaxial ellipsoid of Co (M_s = 1420 emu/cm^3) and NiFe (M_s = 800 emu/cm^3) with two major in-plane axes and an out-of-plane axis which equals 5, 10, 15 or 20 nm. For circular dots, the particle has zero shape anisotropy in the in-plane direction. If the two in-plane axes are not equal, the in-plane coercivities can be estimated from the difference in in-plane demagnetizing factors multiplied by Ms. (Magnetocrystalline anisotropy is neglected.) Assuming a 6 % in-plane shape anisotropy of the dots, an in-plane coercivity ranging between 145 Oe for 5 nm thick Co dots and 345 Oe for 20 nm thick Co dots, and 80 Oe for 5 nm thick NiFe dots and 196 Oe for 20 nm thick NiFe dots would be expected. These values show that a few percent ellipticity in the dot shapes can give rise to a significant in-plane coercivity. Although the estimated values are somewhat higher than the measured in-plane coercivity, such shape anisotropy explains the trend of increasing coercivity with dot thickness. The thicker the sample, the larger the difference between the in-plane demagnetizing factors. Therefore, higher in-plane coercivity is expected in the thicker dot arrays.

The area distribution of the dot arrays is shown in figure 4.3c. The mean area is 903 nm^2, which corresponds to the area of a circle of 34 nm diameter. The standard deviation of the dot diameter is 9 %. The variation of the particle size mainly comes from the block copolymer templates where the size non-uniformity is a result of low diffusivity of polymer molecules. A longer annealing time and higher annealing temperature can enhance the diffusivity of the polymer molecules and improve the size distribution of the block copolymer templates and thus give better size distribution of magnetic dot arrays. Both the aspect ratio and size distribution of the magnetic dots contribute to the variation of the coercivity of the dots.

The variability of switching field of the dot arrays can be quantified from the derivative of the hysteresis loops. The derivatives of the hysteresis loops of Co and NiFe dot arrays are

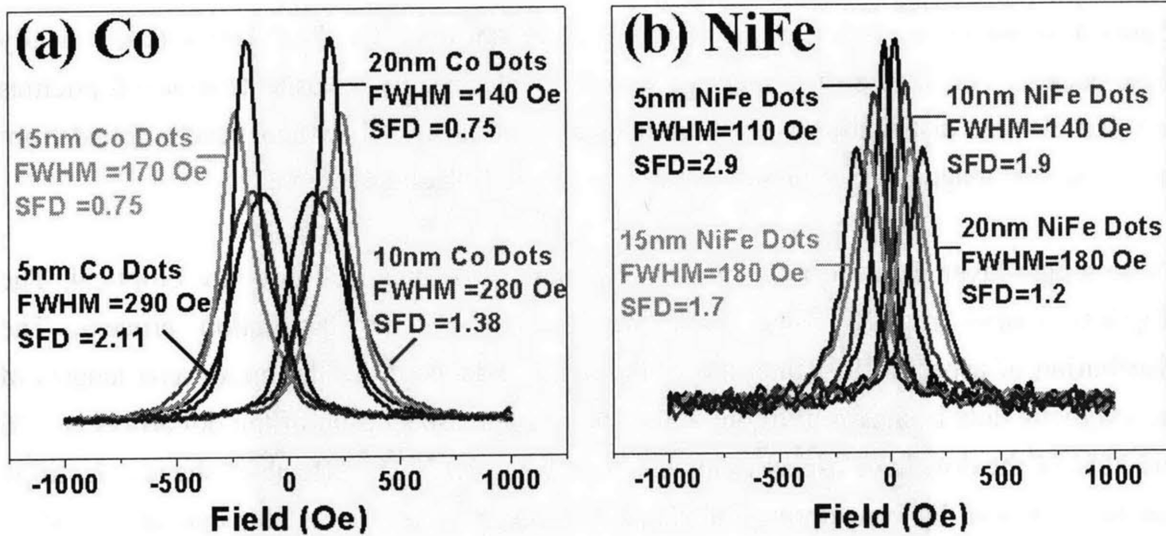

Figure 4.4 The in-plane switching field distribution of single-layer (a) Co dot arrays and, (b) NiFe dot arrays with dot thickness from 5 nm to 20 nm.

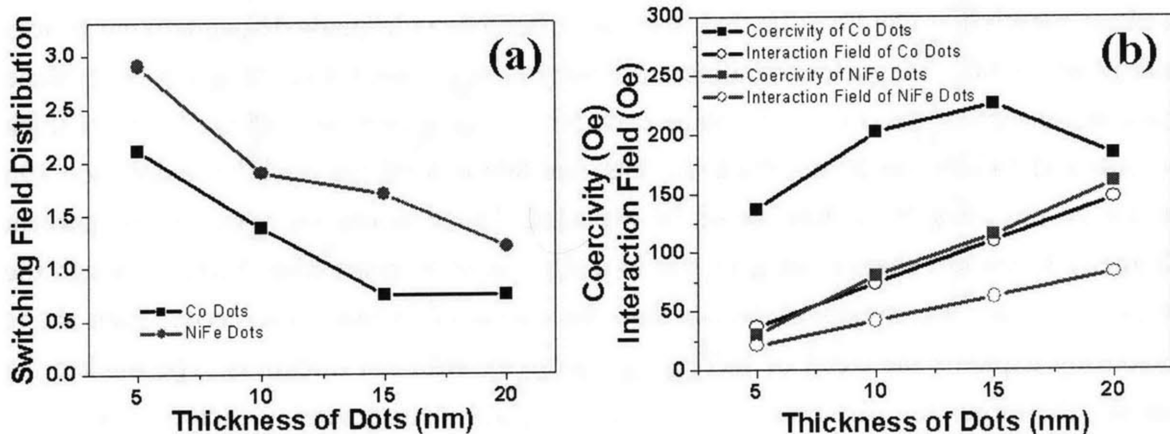

Figure 4.5 (a) Switching field distribution of Co dots and NiFe dots. (b) The coercivity of the Co and NiFe dots (solid symbols) and the interaction field from one neighboring Co and NiFe dot (open symbols).

shown in figure 4.4. The switching field distribution (SFD) is defined as the ratio between full width at half maximum (FWHM) of the peak and the coercivity. Variability of magnetic properties between dots, expressed by SFD, is relatively large as a result of the variations in shape, size and the effects of magnetostatic interactions. Figure 4.5a plots the SFD of Co and NiFe dots as a function of their thickness. The switching field distribution decreases for thicker dots, indicating less variability between individual dots. In addition, the switching field distribution in NiFe arrays is wider, relatively, than in Co arrays. The distribution of dot shape and size are the same for various dot arrays and therefore cannot account for these trends. These trends more likely to be a result of magnetostatic

interactions between the dots. In figure 4.5b, the interaction field from one nearest neighbor is compared with the average coercivity of the dots. The interaction field is a significant fraction of the switching field. The dots in the arrays typically have six nearest neighbors and therefore, the interaction field is even greater, so the array behavior is dominated by the magnetostatic interactions.

The interactions between the magnetic particles can be characterized by comparing their remanence curves: isothermal remanent magnetization (IRM) and dc demagnetization (DCD) curves [9]. IRM is obtained by magnetizing an initially AC demagnetized sample by applying an increasing field, H, in small steps and measuring the remanence, $M_r(H)$, after removal of the field. The DCD curve is similarly measured by applying an increasing negative field to an initially saturated sample. The remanence, $M_d(H)$, is obtained after removal of the field. A ΔM plot is used to show the deviation from a non-interacting system and is defined as

$$\Delta M = 2M_r(H) - 1 - M_d(H)$$

Positive values of ΔM are due to interactions promoting the magnetized state (exchange coupling) while negative values of ΔM are caused by interactions tending to assist magnetization reversal (magnetostatic coupling).

Figure 4.6 shows the ΔM plot of 5 nm thick Co arrays and 15 nm thick Co arrays. Negative ΔM indicates these dots are demagnetized by their neighboring particles. The value of ΔM can be used to quantify the interaction in the dot arrays. The interactions of the magnetic

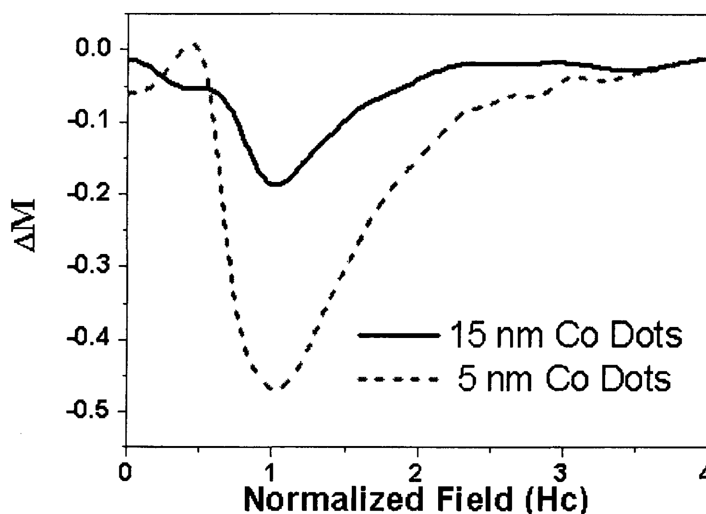

Figure 4.6 ΔM plots of 5 nm thick Co arrays and 15 nm thick Co arrays. The field is normalized to the coercivity of the dot arrays.

dots are stronger in the 5 nm dot array than in 15 nm dot array. Also, the field range for interparticle interaction is wider for the 5 nm dot array. Thinner dots have lower coercivity, therefore, are more affected by the interaction field form the neighbor dots. Accordingly, a wider switching field distribution is found for the thinner dot arrays. For the same reason, the interaction fields in the NiFe arrays are relatively closer to the coercivity than in the Co arrays, consequently, the NiFe has a wider switching field distribution.

In this section, we have shown the hysteresis loops of the Co and NiFe dot arrays. Most of the dots have an in-plane easy axis due to their flat ellipsoid shape. In-plane coercivity increases with thickness. It is caused by shape anisotropy of the dots. The switching field distribution shows that the variability between dots is relatively large. This is a result of the variations in dot shape, dot size and the effects of magnetostatic interactions in the dot arrays.

4.3 Scan-rate dependent Hysteresis of Single-layer Dot Arrays

Switching volume (or activation volume), V_S, represents the volume of magnetic material that must reverse in order for the entire magnetic particle to reverse its magnetization. On the other hand, physical volume, V_P, is the actual size of magnetic particle. The value of the switching volume can be used to characterize the switching behavior and the energy barrier of the magnetic dot arrays. The switching volume and the relation between switching volume and physical volume gives us an insight into how magnetic reversal proceeds in these dot arrays. $V_S \sim V_P$ means the magnetic particle switches coherently and independently from the other particles in the arrays. $V_S > V_P$ suggests that several particles switch together. $V_S < V_P$ indicates incoherent rotation inside a single magnetic particle.

The switching volumes of Co and NiFe dot arrays have been determined by measuring the scan-rate dependence of coercivity, H_C (R). The basic principle and measurement are described by Sharrock [10]. The measured coercivity H_C (R) can be related to the field scan rate R as follows [11]:

$$H_C(R) = C + (k_B T / M_S V_S)\, ln(R)$$

where R (Oe/sec) is the field scan rate during the hysteresis loop measurement, k_B is Boltzmann's constant, T is the temperature and C is a constant.

Figure 4.7 plots rate-dependent coercivity vs. the logarithm of the field scan rate, and shows linear fits to the data. The coercivity changes more quickly with scan rate for thinner Co and NiFe dot arrays, reflecting a smaller switching volume for thermally-assisted magnetization reversal. The switching volume V_S for the in-plane magnetization reversal process can be derived from the slope of the fit to the scan-rate coercivity. Figure 4.8 shows the physical volume and switching volume for the Co and NiFe arrays. The physical volume V_P is calculated from the thickness and diameter of the dots, and is linear in film thickness. The switching volumes of both arrays are found to increase with the film thickness. The ratio of V_S/V_P is 2 - 6 for NiFe dots and 1.5 for Co dots. The switching volume exceeds the physical volume, which suggests that these magnetic dots reverse in a cooperative manner, due to magnetostatic interactions. The magnetostatic interaction is stronger in NiFe arrays than in Co arrays leading to more dots involved in a single switching event. One extreme example is the 5 nm NiFe dot arrays. This array, with the lowest coercivity and strong magnetostatic interactions, gives the largest switching field distribution and the highest V_S/V_P ratio ($V_S/V_P = 6$ in this case) out of all the samples.

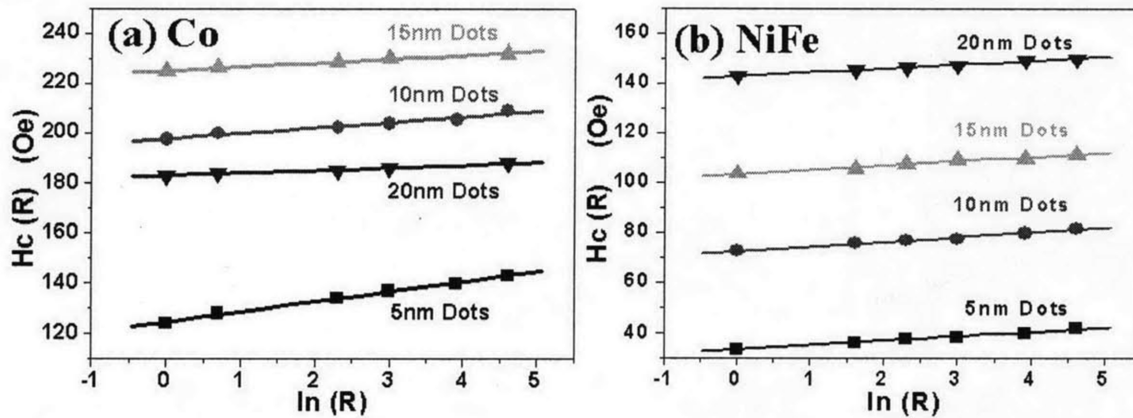

Figure 4.7 Scan-rate dependent coercivity with linear fits for (a) Co, and (b) NiFe arrays.

The energy barrier of magnetization reversal of the dots can be estimated from $K_{eff}V_S$, where K_{eff} is the net magnetic anisotropy. The value of K_{eff} can be estimated as M_SH_0, where H_0 is the coercivity measured at very high field scan rates. This gives a value for K of $3x10^5$ - $4x10^5$ erg/cm^3 for Co dots and $7x10^3$ - $1.5x10^4$ erg/cm^3 for NiFe dots. For both Co and NiFe, K_{eff} is much smaller than the magnetocrystalline anisotropy. K_{eff} has contributions from the shape anisotropy and averaged magnetocrystalline anisotropy over the polycrystalline dots. The energy barrier of Co and NiFe dot arrays is presented in figure 4.9 in units of k_BT (at T = 300 K). All the dots have their energy barrier larger than 25 k_BT and are thermally stable at room temperature. The energy barrier of the dot arrays increases almost linearly with the

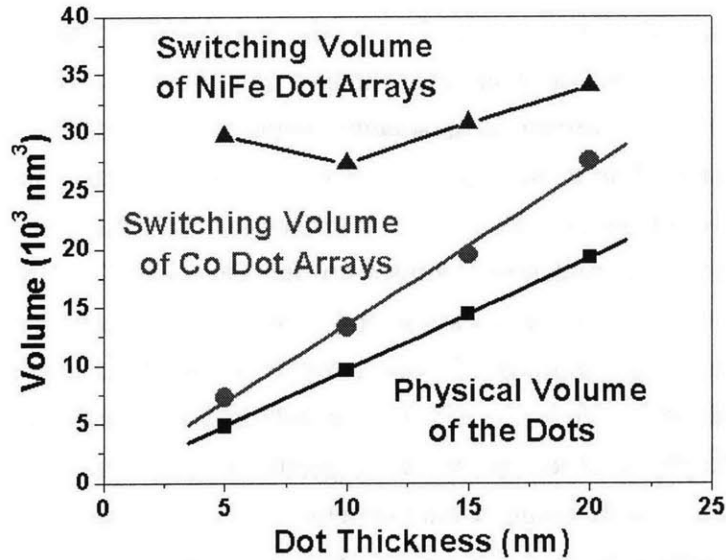

Figure 4.8 Switching volume and physical volume of the Co and NiFe dot arrays.

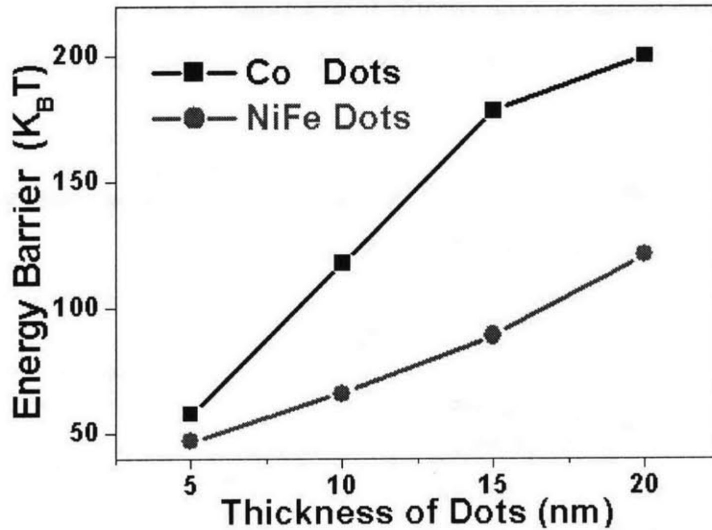

Figure 4.9 The energy barrier, of Co and NiFe dot arrays, expressed in units of kT at T = 300 K.

thickness. Dots of below ~ 2 - 3 nm thickness are predicted to be superparamagnetic at room temperature.

In this section, we have described scan-rate dependent coercivities of single-layer Co and NiFe dots and compared the switching volume V_S and physical V_P volume of the dots. The switching volume is larger than the physical volume in all arrays. This indicates the dots in the arrays are switching cooperatively due to magnetostatic interaction. For data storage application, the interactions of the magnetic dots need to be reduced so that each dot can be addressed independently.

4.4 Magnetic Behavior of Two-layer Dot Arrays

A pseudo-spin-valve (PSV) consists of a non-magnetic layer (typically Cu) between a soft magnetic layer and a hard magnetic layer. The resistance of a PSV depends on the relative orientation of the magnetization in the soft layer and hard layer. The low resistance state corresponds to the parallel orientation of the magnetization in the two layers and the high resistance state corresponds to antiparallel orientation. This giant magnetoresistance (GMR) change can be used in magnetic random access memory (MRAM) applications [12]. Future high density MRAM would rely on deep-submicron patterned layered elements, therefore, the properties of small PSV element are of great interest.

Two-layer pseudo-spin-valve dots are made from the same block copolymer lithography to compare with the magnetic behavior of single layer dots. The unpatterned thin film consists of CoFe 3.3 nm / Cu 6.0 nm / NiFe 4.5 nm. The two-layer dot array has a center-to-center spacing of 56 nm and dot diameter of 34 nm, which is the same as the single layer dots. Figure 4.10 demonstrates the dot structure after patterning and the plan-view SEM micrographs of the patterned two-layer dot arrays.

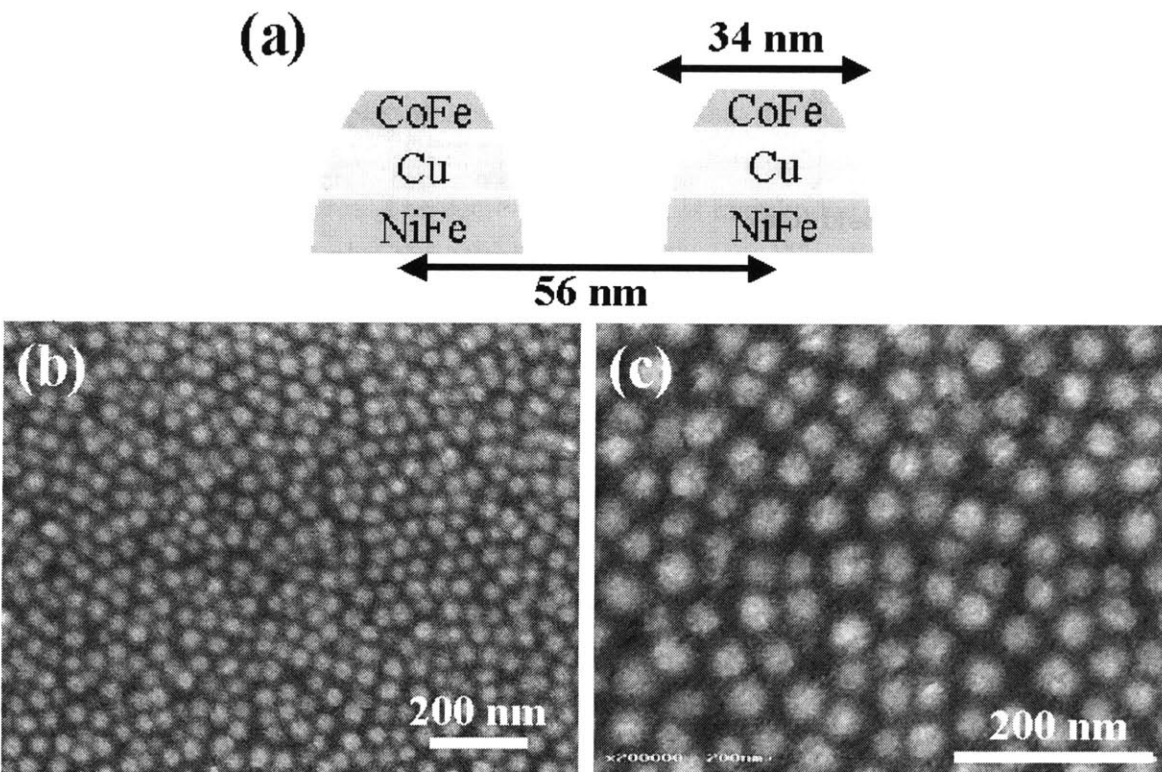

Figure 4.10 (a) Schematic of two-layer (CoFe 3.3 nm / Cu 6.0 nm / NiFe 4.5 nm) dots. (b) & (c) plan-view SEM micrographs of two-layer dots.

The hysteresis loop of the unpatterned CoFe/Cu/NiFe PSV film is shown in figure 4.11a. There are two distinct steps in the hysteresis loop. The NiFe layer (soft layer) and the CoFe layer (hard layer) switch at fields of approximately 5 Oe and 21 Oe respectively. This indicates the interlayer coupling favors parallel magnetization alignment. Figure 4.11b shows the hysteresis loop of arrays of 34 nm-diameter PSV dot arrays. The loop shows distinct switches for two magnetic layers. The hard layer switches at 85 Oe and the soft layer switches at –65 Oe. The NiFe layer switches prior to field reversal leading to antiparallel coupling at remanence, unlike the unpatterned film. This is attributed to the strong magnetostatic interaction between two magnetic layers within the dots. Also, comparing with single layer dots, the switching distribution in PSV dots is narrower than the distribution in the single layer dots. Inter-particle coupling is also strong: interaction from one nearest neighbor dot is about half of the coercivity of the hard layer.

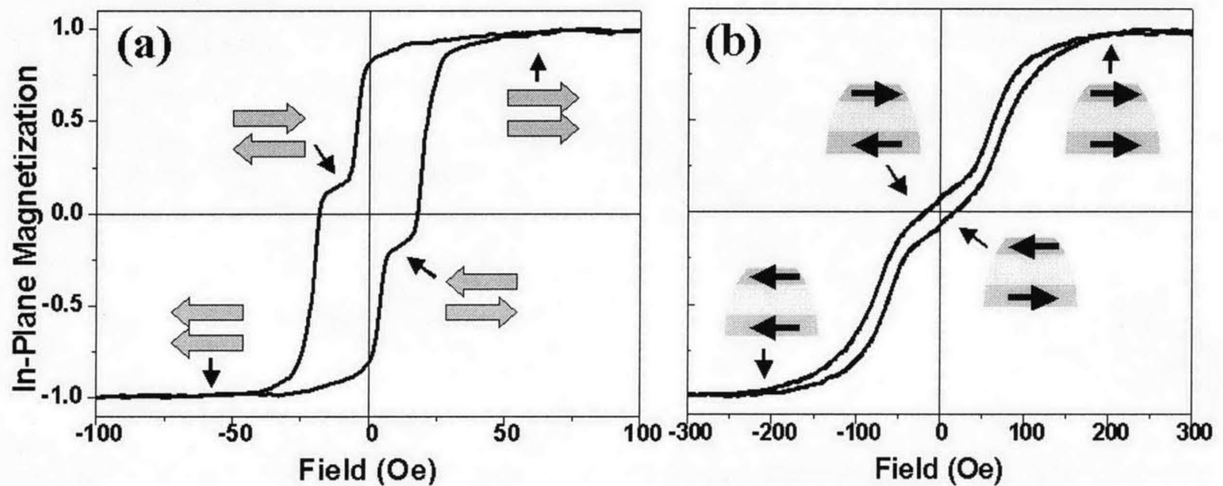

Figure 4.11 Hysteresis loop of (a) unpatterned CoFe/Cu /NiFe PSV film, and (b) patterned PSV dots.

The scan-rate dependent coercivities are plotted in figure 4.12. Linear fitting of the coercivities gives switching volumes of CoFe layer and NiFe layer. The switching volumes for CoFe layer and NiFe layer are 2×10^4 nm^3 and 8×10^4 nm^3 respectively. On the other hand, the physical volumes of CoFe layer and NiFe layer are 2.5×10^3 nm^3 and 4.5×10^3 nm^3 respectively. The switching volume is much larger than the physical volume and the ratio of V_S/V_P is 10 to 20 which is much higher than that of single layer dots. Such high switching volume of two-layer dots is attributed to strong coupling within the dots and between the dots.

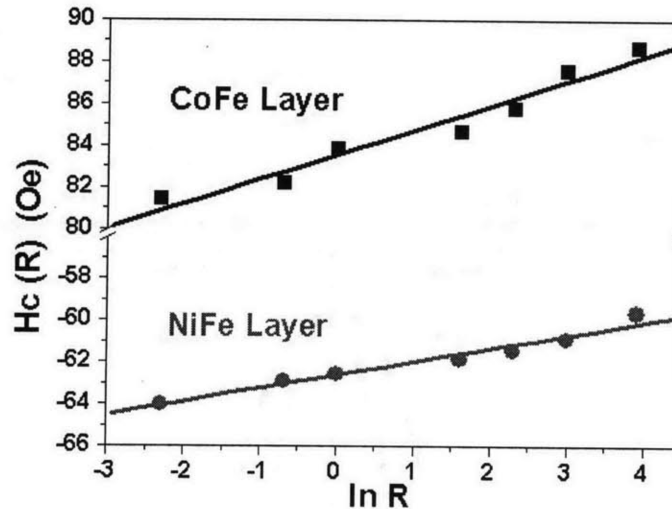

Figure 4.12 Scan-rate dependent coercivity with linear fits for CoFe/Cu/NiFe PSV dot arrays.

A sample of the PSV dot arrays was covered with 5 nm evaporated Au film as illustrated in figure 4.13a for GMR measurement. The GMR ratio, defined as $\{[\rho(H)-\rho(H_{max})]/\rho(H_{max})\}\times100\%$, is measured by a conventional four-point probe. The GMR of the unpatterned PSV film is 0.7%. The GMR of dots coated with Au is 0.16% as shown in figure 4.13b. The strong magnetostatic interaction between two layers results in the antiparallel coupling states at remanence and high resistance state at zero field. Although the GMR ratio of PSV dot arrays is small, it is clear that the block copolymer lithography can be used to pattern PSV film without extensive damage to the interface between the layers in the PSV structures. The decrease of GMR is mainly due to the shunting effect of the Au and residual W, plus the effects of patterning on the edges of the multilayer [13]. Assuming the shunting effect is eliminated, the GMR change of patterned PSV elements is estimated around 1%. The patterning process seems to maintain the GMR effect from the bulk film [14].

In conclusion, single layer dots of Co, NiFe, and two layer dots of CoFe/Cu/NiFe pseudo-spin-valve are successfully made from polystyrene-polyferrocenyldimethylsilane templates. The hysteresis loops and time dependent coercivities are measured and compared to show the magnetic switching behavior of these arrays. The coercivity increases as the thickness of the dots increases. This trend can be interpreted as a result of in-plane shape anisotropy. In addition, thermally activated reversal and large switching field distribution are observed in all samples. The switching volumes extracted fromscan-rate hysteresis loop measurements are larger than the physical volumes of the dots. These indicate strong magnetostatic interaction between the dots. The patterned PSV

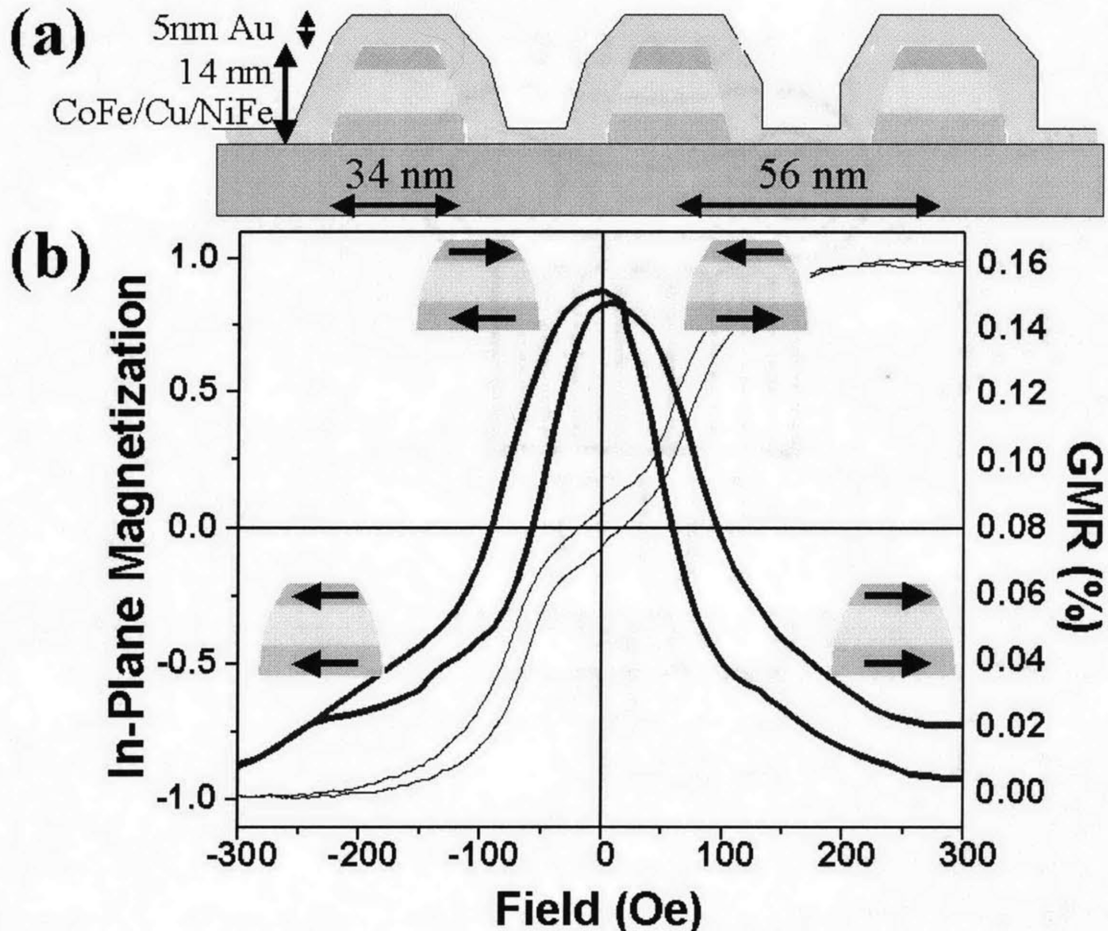

Figure 4.13 (a) The schematic of CoFe/Cu/NiFe PSV dot arrays for magnetoresistance measurement. (b) The GMR curve of CoFe/Cu/NiFe PSV dot arrays. The hysteresis loop is superimposed onto GMR curve to show the magnetic states of soft layer and hard layer.

dots show magnetostatic interaction between two layers within a dot. Such strong inter-dot and intra-dot magnetostatic interaction leads to very large switching volume.

Data storage applications require the dots to switch independently. Therefore, it is important to reduce the inter-dot and intra-dot magnetostatic interaction. The present work suggests that using material with higher Ms or high magnetic anisotropy will lead less inter-dot magnetostatic interaction and smaller switching field distribution. For the two-layer dots, structure such as a synthetic antiferromagnet multilayer could be used to reduce the intra-particle magnetostatic interactions. Ordered magnetic dot arrays made from magnetic thin films with high perpendicular crystalline anisotropy are ideal for patterned media. There are two main advantages. First, the anisotropy of the media in such system is dominated by crystalline anisotropy rather than shape anisotropy, which is sensitive to the

patterning process. Second, ordered dot arrays are necessary for the head to address each single bit. These two criteria can be achieved by well-controlled thin film growth technique and templated self-assembly of block copolymers [15].

Reference

1. J. I. Martin, J. Nogues, K. Liu, J. L. Vicente, I. K. Schuller, *J. Mag. Mag. Mater.* **256**, 449 (2003)
2. C. A. Ross, *Ann. Rev. Mater. Res.* **31**, 203 (2001)
3. G. Zangari, D. N. Lambeth, *IEEE Trans. Magn.* **33**, 3010 (1997); R. M. Metzger, V. V. Konovalov, M. Sun, T. Xu, G. Zangair, M. Benakli, W. D. Doyle, *IEEE Trans. Magn.* **36**, 30 (2000); K. Nielsch, R. B. Wehrspohn, J. Barthel, J. Kirschner, U. Gosele, S. F. Fischer, and H. Kronmuller, *Appl. Phys. Lett.* **79**, 1360 (2001)
4. S. P. Li, W. S. Lew, Y. B. Xu, A. Hirohata, A. Samad, F. Baker, J. A. C. Bland, *Appl. Phys. Lett.* **76**, 748 (2000)
5. T. Thurn-Albrecht, J. Schotter, G. A. Kastle, N. Emley, T. Shibauchi, L. Krusin-Elbaum, K. Guarini, C. T. Black, M. T. Tuominen, T. P. Russell, *Science*, **290**, 2126 (2000); K. Liu, S. M. Baker, M. Tuominen, T. P. Russell and I. K. Schuller, *Phys. Rev. B* **63**, 060403R (2001); T. Shibauchi, L. Krusin-Elbaum, L. Gignac, C. T. Black, T. Thurn-Albrecht, T. P. Russell, J. Schotter, G. A. Kastle, N. Emley, M. T. Tuominen, *J. Mag. Mag. Mater.* **226**, 1553 (2001); K. Shin, K.A. Leach, J. T. Goldbach, D. H. Kim, J. Y. Jho, M. Tuominen, C. J. Hawker, T. P. Russell, *Nano Lett.* **2**, 933 (2002)
6. J. Y. Cheng, C. A. Ross, V. Z. Chan, E. L. Thomas, R. G. H. Lammertink, G. J. Vancso, *Adv. Mater.* **13**, 1174 (2001); J. Y. Cheng, C. A. Ross, E. L. Thomas, H. I. Smith, G. J. Vancso, *IEEE Trans. Magn.* **38**, 2541 (2002)
7. K. Asakawa, T. Hiraoka, H. Hieda, M. Sakurai, Y. Kamata, *J. Photopolymer Sci. Tech.* **15**, 465 (2002); K. Naito, H. Hieda, M. Sakurai, Y. Kamata, K. Asakawa, *IEEE Trans. Magn.* **38**, 1949 (2002)
8. R. P. Cowburn, D. K. Koltsov, A. O. Adeyeye, M. E. Welland, D. M. Tricker, *Phys. Rev. Lett.* **83**, 1024 (1999); H. Hoffmann, F. Steinbauer, *J. Appl. Phys.* **92**, 5463 (2002)
9. O. Henkel, *Phys. Stat. Sol.* **7**, 191 (1964)
10. M. P. Sharrock, *IEEE Trans. Magn.* **35,** 4414 (1999)
11. P. Bruno, G. Bayreuther, P. Beauvillain, C. Charppert, G. Lugert, D. Renard, and J. Seiden, *J. Appl. Phys.* **68**, 5759 (1990); P. L. Lu. and S. H. Charap, *J. Appl. Phys.* **75**, 5768 (1994)
12. B. A. Everitt, A. V. Pohm, R. S. Beech, A. Fink, and J. M. Daughton, *IEEE Trans. Magn.* **34**, 1060 (1998)
13. F. J. Castano, S. Haratani, Y. Hao, C. A. Ross, H. I. Smith, *Appl. Phys. Lett.* **81**, 2809 (2002)
14. B. A. Everitt, A. V. Pohm, *J. Vac. Sci. Tech. A* **16**, 1794, (1998)
15. J. Y. Cheng, C. A. Ross, E. L. Thomas, H. I. Smith and G. J. Vancso, *Appl. Phys. Lett.* 81, 3657 (2002)

Chapter 5

TEMPLATED SELF-ASSEMBLY OF BLOCK COPOLYMERS ... USING TOPOGRAPHICAL TEMPLATES

In self-assembled materials, the interaction among the structural units is relatively weak and, therefore, the self-assembled structures only have short-range ordering rather than long-range ordering as is found in atomic crystals. Block copolymers are known for good ordering in annealed bulk samples, while short-range ordering is typically observed for thin film samples as shown in the previous chapters. Some potential applications of block copolymer lithography require ordered arrays and some require the ability to tailor the periodicity. Therefore, there is an interest in developing methods to guide the self-assembly process.In living systems, self-assembly processes are controlled by the use of templates, for instance DNA is the template from which proteins are synthesized. The concept of using a template to control self-assembly can be extended to a range of non-biological self-organized systems, in which a template serves to impose long-range order and minimize defect levels in the resulting structure, creating assemblies that otherwise would not spontaneously form[1-11]. We call this process templated self-assembly. In this chapter, we will show how templated self-assembly can be achieved in a model system consisting of a block copolymer whose microphase-separation is templated by a lithographically-patterned substrate.

Background information, experiments and structural characterization of templated PS-PFS block copolymers in various topographical substrates are presented in this chapter. The first section covers a brief review of templated self-assembly of block copolymer thin films. It is followed by a section on the analysis of PS-PFS on a smooth substrate to quantify the basic structure parameters of these particular polymers. After that, the structures of polymers in topographical confinements are demonstrated and discussed in the third section. Well-ordered structures of SF 32/10 are found in grooves with proper confinement. The final section analyzes the structure of well-ordered SF 32/10 block copolymers, and shows that quantized rows of domains are found within the grooves. Dislocations and missing polymer domains can be purposefully introduced by the features on the templates. Combing with block copolymer lithography, these ordered structures may be useful as lithographic masks for fabricating electronic or magnetic devices.

5.1 Templated Self-assembly of Block Copolymers

An artificial surface topographic pattern on the substrate can be used to orient the growth of a thin film in a process known as graphoepitaxy [4]. This has been used to orient crystals grown from solution or vapor [4,5] or to induce alignment in liquid crystals [6]. Similarly, to direct the self-assembly process, substrates with topographical features or chemical heterogeneities have been used to influence the position and/or orientation of the block copolymer domains which form when the block copolymer phase-separates. The substrate features can cover a range of length-scales relative to the dimensions of the block copolymer domains. Substrates with shallow steps separated by distances of several microns have been shown to lead to long-range ordering of a spherical-morphology polystyrene-polyvinylpyridine (PS-PVP) block copolymer, in which perfect ordering of fifty to two hundred domains was created perpendicular to the steps [7]. In this system, since the length-scale of the template is very large compared to the domain size, the effects of incommensurability are negligible, and defects result primarily from entropic effects. In comparison, at the opposite extreme of template length-scale, lamellar domains in polystyrene-polymethylmethacrylate (PS-PMMA) have been oriented along chemically heterogeneous stripes formed lithographically on a substrate, provided that the stripe width is very close to the width of the lamellar domains [8,9]. Defects are observed when there is large mismatch between the period of the substrate pattern and that of the block copolymer. There has also been some exploration, for lamellar-morphology block copolymers, of the effect of rigid confinement in the thickness direction, perpendicular to the substrate. In both symmetric and asymmetric wetting conditions, if the thickness is commensurate with the domain period, an integer number of parallel lamellae form. If the thickness is incommensurate, an integer number of lamellae also form but the period deviates from the equilibrium value [10,11]. The layer thickness inside the slit can be derived from fitting neutron reflectivity data. However, the information of local defects and the correlations between layers and guiding geometry, which is important for understanding templated self-assembly, cannot be derived from the reflectivity or scattering data.

Studying the in-plane nanostructures of block copolymer domains in the confinements therefore appears to offer rich opportunities of direct observation of the ordering behavior of block copolymers. In this chapter, we have investigated the behavior of a spherical-morphology PS-PFS in various one-dimensional topographical confinements. We show how the spatial arrangement of the block copolymer domains can be influenced by topographical confinement on a length-scale of a few domain periods, where the effects of incommensurability and surface-induced ordering are expected to be significant.

5.2 Block Copolymers on a Flat Surface

Block copolymer thin films have short-range ordering are nonuniform. This section is to quantify the ordering and size distribution of PS-PFS block copolymers and explain their molecular weight dependence.

Two PS-PFS samples, SF 91/21 and SF 32/10, employed in the experiments are sphere-morphology block copolymers. When toluene solution of PS-PFS is spun onto a flat substrate and annealed (at 180°C for PS/PFS 91/21 and 140°C for PS/PFS 32/10) for two days, it forms a single layer of PFS spheres in a PS matrix, with PS present at the film-air interfaces and a thin brush layer with PFS at the film-substrate interfaces. The structure of the annealed polymer thin film is illustrated in figure 5.1.

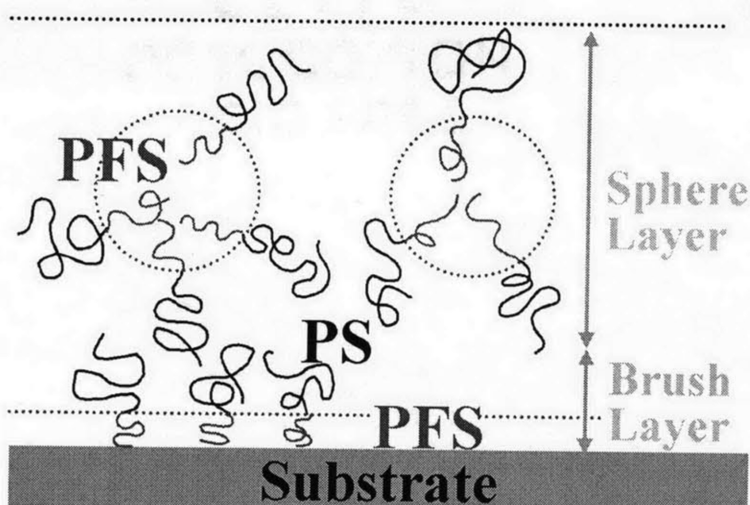

Figure 5.1 Schematic of the arrangement of the polymer chains in the domains and at the polymer film-substrate surface.

Because of the presence of iron and silicon in the PFS block, this organometallic block is more resistant to an oxygen plasma than the organic PS block. Under an oxygen plasma treatment, the PS matrix is removed and oxidized PFS features are well preserved and left on the substrate [12,13]. The microdomains of PFS are clearly resolved by SEM after oxygen plasma treatment just as they were in the film. Therefore, combining with the etching method, the PS-PFS system provides high quality data for analysis and quantification of the nanostructures of a block copolymer thin film on flat and patterned substrates.

Plan-view micrographs of annealed SF 91/21 and SF 32/10 thin films on a silica surface are demonstrated in figure 5.2. The average diameters of the dots are 34 nm and 18 nm for SF

91/21 and SF 32/10. The size variation is larger in SF 91/21 sample for which the standard deviation in diameter is 14%, compared to 7% deviation in SF 32/10.

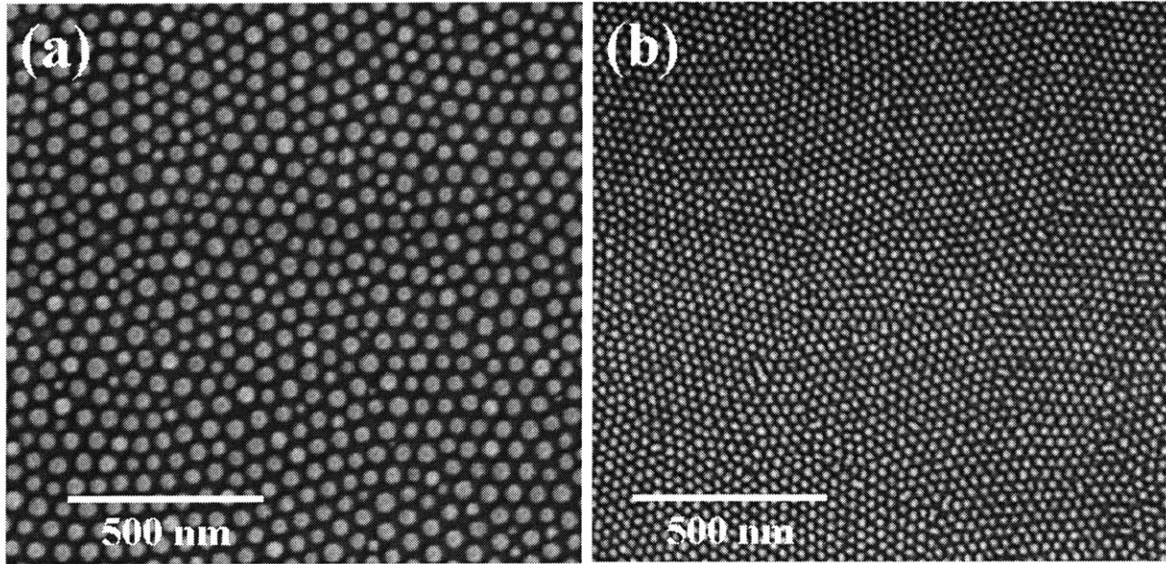

Figure 5.2 Plan-view SEM micrographs for (a) SF91/21 and (b) SF33/10.

To quantitatively describe the short-range-ordering structures of SF block copolymer thin film, a dimensionless pair distribution function (PDF) g(r) is used. The pair distribution function is defined as:

$$g(r) = \frac{1}{\rho} \frac{dn(r, r + dr)}{dA(r, r + dr)}$$

dn is the number of pairs of particles with an inter-particle distance within *r* and *r* + *dr* and *dA* is the area within *r* and *r* + *dr*. ρ is the areal density of the particles. Figure 5.3 shows the PDF for SF 91/21 and 33/10.

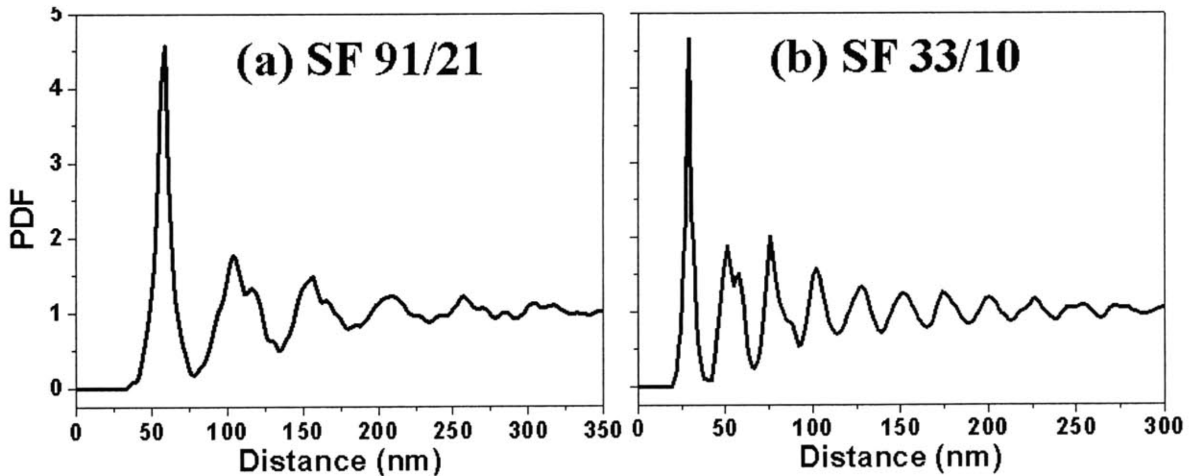

Figure 5.3 Pair distribution function of (a) SF 91/21 and (b) SF 32/10

The arrangement of PFS spheres in the block copolymer thin film is similar to the hard sphere model. There is an inter-PFS-sphere potential so that the pair distribution function (PDF) is zero within the excluded diameter, which is 35 nm for SF 91/21 and 20nm for SF 32/10. The PDF is large when the distance happens to equal a particular preferred inter-particle spacing. The first peak indicates the center-to-center spacing between the nearest neighbors, which is a_o = 56 nm for SF 91/21 and a_o = 28.6 nm for SF 32/10. The number of nearest neighbors estimated by the area under this first peak in PDF is around 6 for both polymers. The spacing for the second and third nearest neighbors correspond to $\sqrt{3}a_o$ and $2a_o$, indicating a local hexagonal symmetry. The correlation distance characterizes the spatial extent of short-range order. Correlation length, defined as the distance where the PDF reaches its asymptotic constant, is 320 nm and 280 nm for SF 91/21 and SF 32/10 respectively, corresponding to ~6 and 10 sphere spacings. In general, SF 32/10 has better ordering and narrower size distribution.

Polymer	Sphere Diameter	STD in Diameter	Excluded Diameter	Sphere Spacing	Correlation Length
SF 91/21	34 nm	13 %	35 nm	56 nm	320 nm
SF 32/10	18 nm	7 %	20 nm	28.6 nm	280 nm

Table 5.1 Basic data for SF 91/21 and SF 32/10 thin film on the flat surface.

The uniformity and ordering of the nanostructures in block copolymer thin films are determined by their diffusivity. The spherical domains are created / annihilated through the association / dissociation of the block copolymer molecules to reach minimum system free energy. The energy barrier (or activation energy) for moving minority blocks from one spherical domain to another governs the diffusion process of sphere block copolymers [14]. The diffusion coefficient D is given by

$$D = D_0 * \exp(-\alpha\chi N_{minor})$$

and the energy barrier for the diffusion in sphere block copolymer is $\Delta G = N_{minor} k_B T$ where χ is the Flory-Huggins parameter, N_{minor} is degree of polymerization of minority block and $k_B T$ is thermal energy. According to the scattering analysis [15], the Flory-Huggins parameter, χ in PS-b-PFS is

$$\chi(T) = 0.028 + \frac{3.28}{T}$$

Using this relation, we have $\chi N = 25.3$ and $\chi N_{minor} = 5.1$ for SF 32/10 annealed at 140°C and $\chi N = 65.8$ and $\chi N_{minor} = 10.6$ for SF 91/21 annealed at 180°C. The diffusivity of SF 32/10 is 245 times of that of SF 91/21 at their annealing temperatures used in this experiment, leading to higher uniformity and better ordering in SF 32/10 than in SF 91/21.

5.3 Block Copolymers on Grooved Substrates

We investigated the nanostructures of the SF 91/21 and SF 32/10 block copolymers on various grating substrates to examine the templating effect. The annealing process and the ordering of SF 91/21 and SF 32/10 are studied and discussed in this section.

The topographical relief structure for templating self-assembled block copolymers was made by interference lithography (IL), [16,17] a maskless method which is ideal for patterning large-area periodic structures. Details of grating fabrication are given in section 2.3. In this experiment, the depth of grating is designed to be larger than the thickness of one minority domain of the PS/PFS block copolymer, and the width of the grooves was varied to test the confinement effect. Three different gratings with 70 nm step height were used in this work: a 700 nm-period grating with 480 nm - 510 nm groove width, a 440 nm-period grating with 300 nm - 330 nm grove width, and a 440 nm-period grating with 230 nm - 260 nm groove width. This templating process can be called graphoepitaxy.

5.3.1 Annealing of Block Copolymers on Grating Substrates

To study the templating effect of the block copolymer films, toluene solutions of SF 32/10 and SF 91/21 was spin-cast onto patterned silica substrates using various spin rates. The spin-cast and annealed samples of SF 32/10 are demonstrated here to reveal the ordering mechanism due to the substrate topography, the same phenomena were observed in SF 91/21 samples as well.

As-spun SF 32/10 films exhibit conformal coverage as shown in figure 5.4a. Etching of the film using an oxygen plasma removes the PS to reveal PFS spheres, where microdomains of PFS are randomly distributed on both the mesas and valleys of the grooves (figure 5.4b). The morphology of the polymer is significantly altered by annealing. After a 4-hour 140˚C anneal, figure 5.4c shows that the top surface of the polymer film is smooth and flat. The appearance of the fracture surface indicates that polymer is present only in the valleys. Etching of the film in oxygen shows an array of PFS spheres in the valleys but not on the mesas. Moreover, the rows of spheres in the valleys are partially aligned with the step edges as illustrated in figure. 5.4d. The gap present between the first row of spheres and the step edges shows that there is a thin PFS-PS brush layer present at groove edge and groove

bottom where PFS wets the silica surface. Such wetting behavior is the same as that of polymer film on the flat silica substrates. This surface-induced thin layer provides the driving force to align the PS-PFS copolymers and results in PFS features parallel to the groove edges [18, 19].

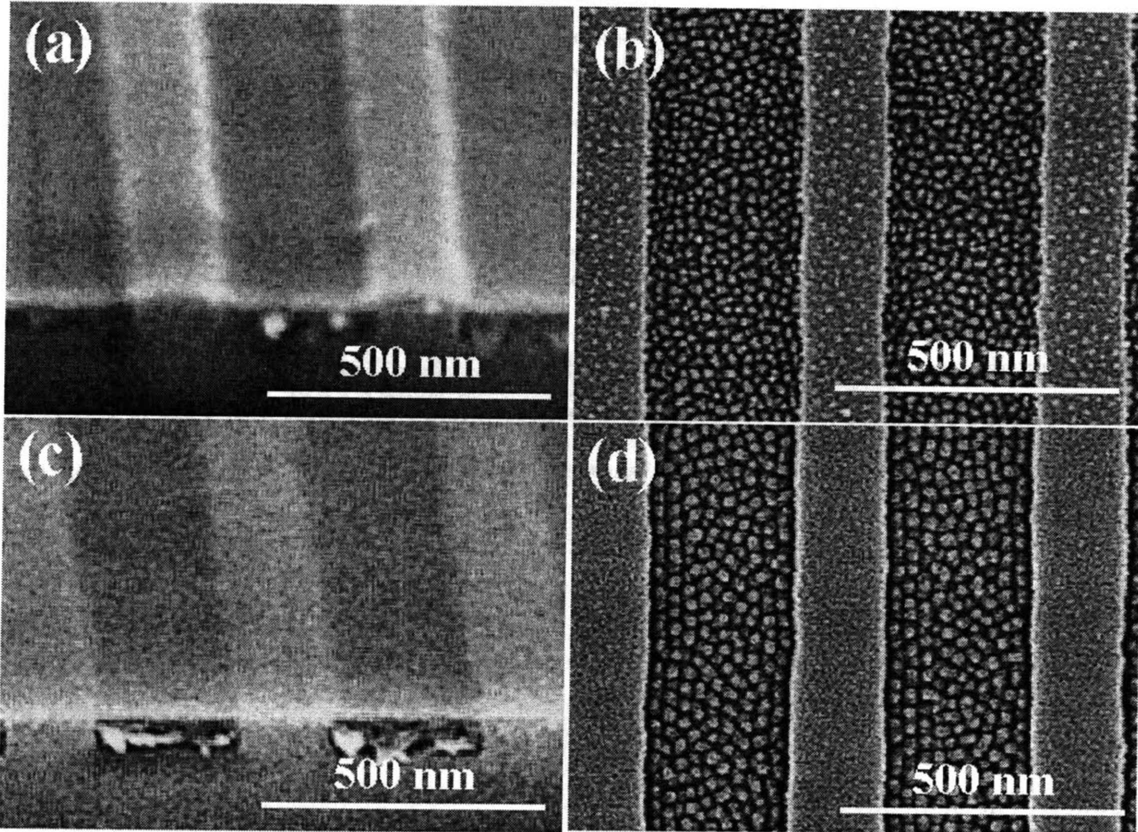

Figure 5.4 SEM micrographs of PS/PFS 32/10 polymer films on patterned substrates. (a) As-spun film, showing conformal coverage; (b) The same film after oxygen plasma etching, showing PFS features on the mesas and valleys of the topography; (c) Film spun then annealed at 140°C for 4 hours, showing a smooth surface as the polymer flows into the valleys; (d) The same film after oxygen etching, showing PFS features present only in the valleys and partially aligned with the steps.

5.3.2 SF 91/21 Thin Films in the Grooves

A solution of SF 91/21 was spun to produce thin films on various grating substrates. After 180°C 48-hour annealing and removing the PS via oxygen plasma, PFS features are revealed. Similar to SF 32/10, a ~ 20 nm PFS wetting layer of the grating provides the driving force to align the PFS features parallel to the groove edges [19]. Figure 5.5a shows that SF 91/21 forms one row of close-packed features at either sidewall when confined within a 500 nm wide groove. The wetting of PFS on the sidewall and the interaction force between the two blocks induce templated self-assembly of the first layer of PFS features. However, due to the low diffusivity of the SF 91/21, the block copolymer microdomains near the center of the groove do not align well with those near the sidewall. Additionally, a size distribution of the PFS domains was found in the 500 nm wide grooves, the same as the size distribution in films deposited on flat substrates. The standard deviation of diameters of the PFS features is ~15%. However, it is noted that larger dots tend to locate at the center while smaller dots at the groove edges which is different from the case on the smooth substrates.

In figure 5.5b, SF 91/21 in a 320 nm wide groove gives better alignment, because the narrower grooves result in stronger confinement and hence fewer misoriented grains in the PFS array compared to figure 5.5a. In addition, the stronger confinement effect leads to faster kinetics and hence the system is closer to an equilibrium state with smaller size distribution. The standard deviation of diameters of the PFS features is ~11% in this case. In figure 5.5c, the SF 91/21 block copolymer is shown in 240 nm wide grooves. Five rows of PFS features are seen parallel to the gratings in some places although the order from the confinement is still imperfect. Clearly, smaller grooves lead to stronger confinement, but due to the low diffusivity of SF 91/21 and incommensurate groove width, the confinement does not lead to complete ordering on these substrates under our annealing condition.

In addition, PFS hemispheres are observed on the edge of the groove in figure 5.5. The structures of polymer chains are illustrated in figure 5.6. A similar situation was found in thin free-standing films of PS-PB block copolymers where PB is the minority block (SB 23/10) [20]. In the PS-PB free-standing film, PB is present at both air-film interfaces as brush layers. The morphology changes as thickness varies, between the thickness of a bilayer and the thickness of a sphere layer plus two brush layers. An intermediate state appeared to be hemisphere PB domains attached to the PB brush layer. In the SF 91/21 system, the formation of the hemispheres at the groove edges may reduce the strains from incommensurate confinement, and decreases the total interfacial area between the PS block

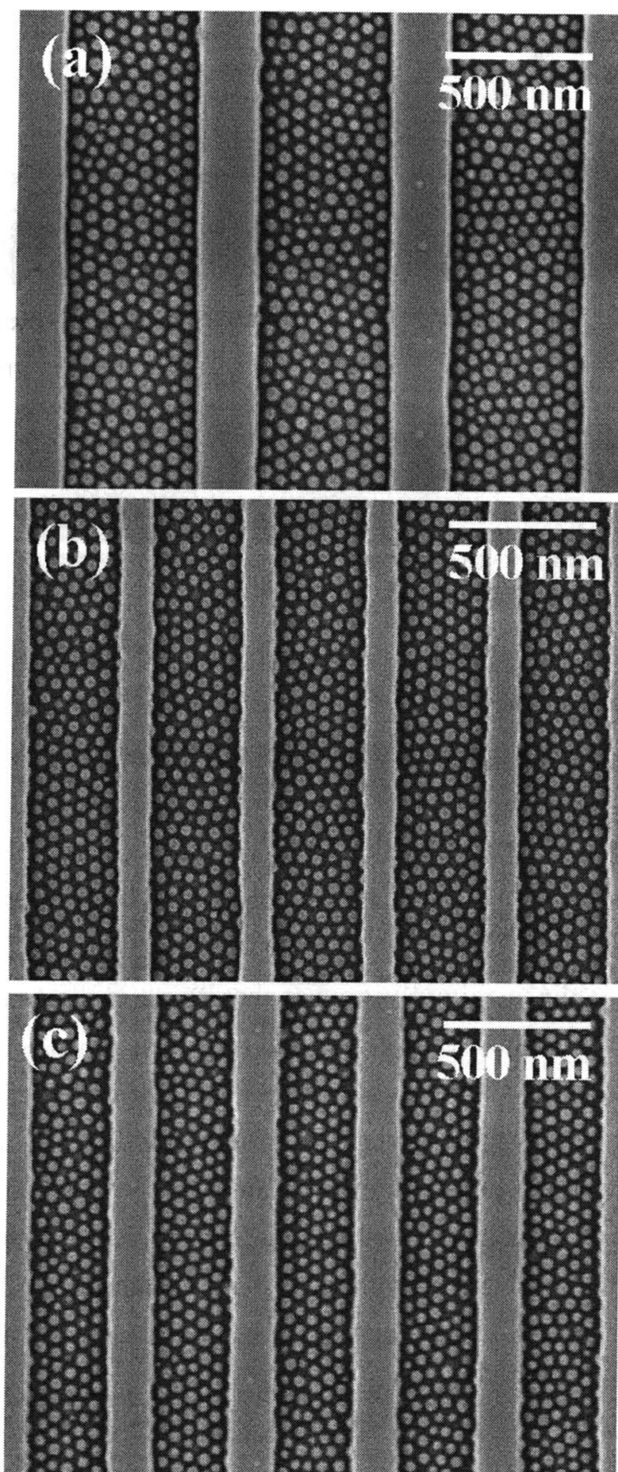

Figure 5.5 SEM micrographs of annealed and oxygen plasma treated SF 91/21 films on silica gratings with (a) 500 nm wide grooves. (b) 300 nm wide grooves. (c) 240 nm wide grooves.

and PFS block.

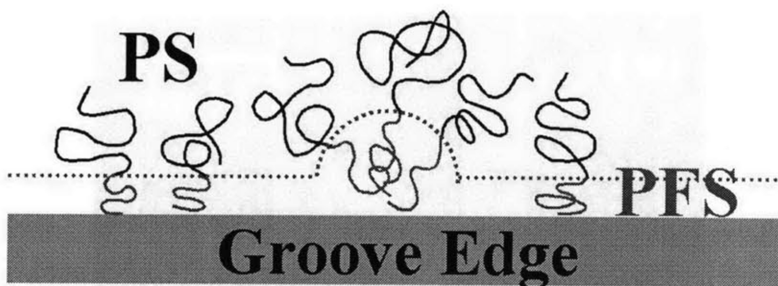

Figure 5.6 Schematic of the arrangement of the polymer chains within hemisphere and brush layer at the film-substrate interface.

5.3.3 SF 32/10 Thin Films in the Grooves

A similar series of experiments was conducted with SF 32/10, which has a higher diffusivity and hence better ordering and narrower feature size distribution than PS/PFS 91/21. A 1.5% SF 32/10 solution in toluene was spun onto substrates with groove widths of 500 nm, 320 nm and 240 nm at 3500 rpm and then annealed at 140°C for 48 hours. Figure 5.7a shows, after oxygen plasma etch, three rows of close-packed PFS features aligned parallel to the sidewall within a 500 nm wide groove. The ordering effect propagates further into the center of the grooves as the groove width is reduced. The domain diameters of the PFS near the sidewalls are slightly smaller than those in the center of the groove. In the 320 nm grooves, features both at the center and near the sidewalls are aligned as shown in figure 5.7b. However, a few "grain boundaries" are still observed. In figure 5.7c, SF 32/10 block copolymers show nearly perfect alignment in 240 nm wide grooves, in which the groove width is comparable to the polymer "grain size" or "correlation length". An area of 4 μm x 4 μm typically contains fewer than ten defects, and grain boundaries are rarely observed. Figure 5.7c reveals sixfold-symmetry of the features inside the gratings. The associated Fast Fourier Transform of figure 5.7c shows sets of sixfold spots closely arranged in Fourier space. This indicates that orientation of the grains in adjacent grooves is the same. Defects inside the grooves are mostly generated from the width variation of the grooves. The rare domain packing defects are apparently generated from the edge roughness of the grooves. The quality of the alignment increases with annealing time, as misaligned grains are observed to reorder to bring close-packed rows parallel to the groove sidewalls. The number of aligned rows increases as the annealing time increases. This can be seen by comparing figure 5.4d (4 hour anneal) with figure 5.7c (48 hour anneal).

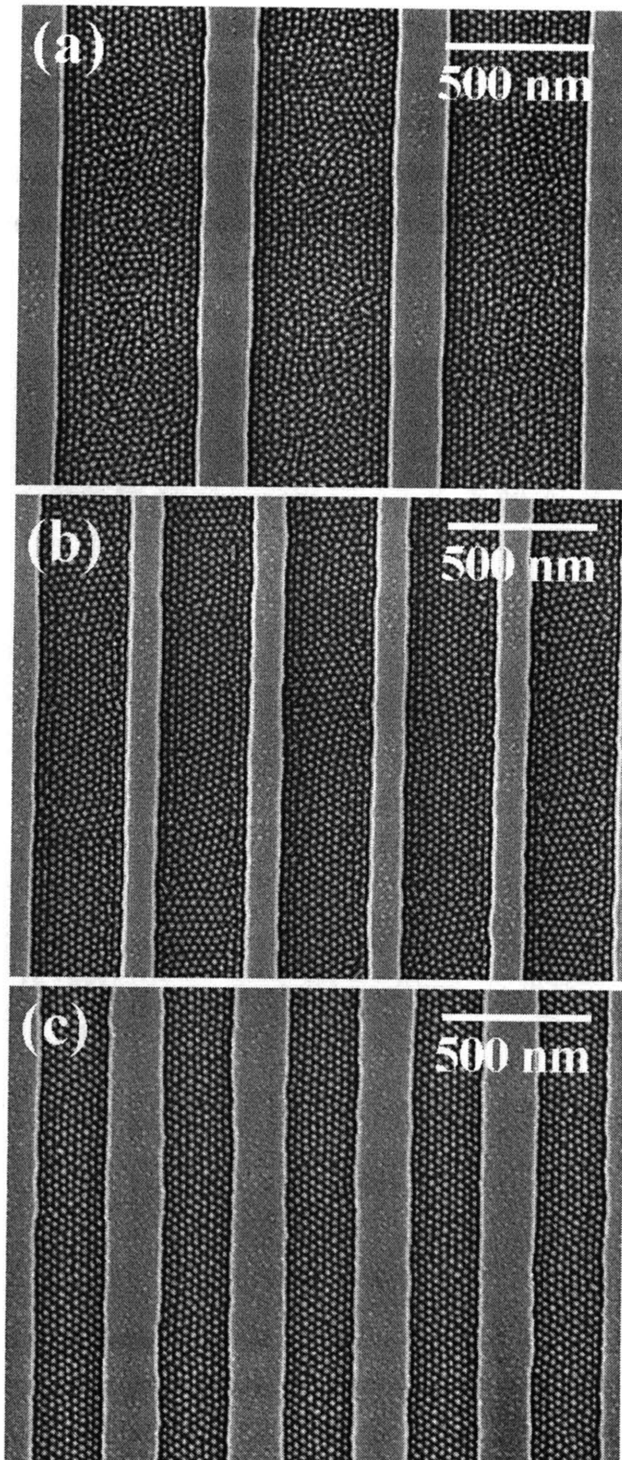

Figure 5.7 SEM micrographs of annealed and oxygen plasma treated SF 32/10 films on silica gratings with (a) 500 nm wide grooves. (b) 320 nm wide grooves. (c) 240 nm wide grooves.

The well-ordered domain patterns (figure 5.8a) were transferred into the underlying silica using a reactive ion etch process with a CHF_3 plasma. This produced ordered arrays of silica posts with aspect ratios of three or higher as shown in figure 5.8b. The silica posts have uniform widths of 20 nm which is consistent with the PFS sphere size, though some height variations exist, presumably due to erosion of the PFS caps on top of each silica pillar. Ordered nanostructures of other materials such as cobalt can be formed by transferring the silica pattern into underlying films such as W/Co bilayers, as described previously [13], making this lithography method applicable to a wide range of materials. The good aspect ratios available in the patterned silica structures are particularly advantageous

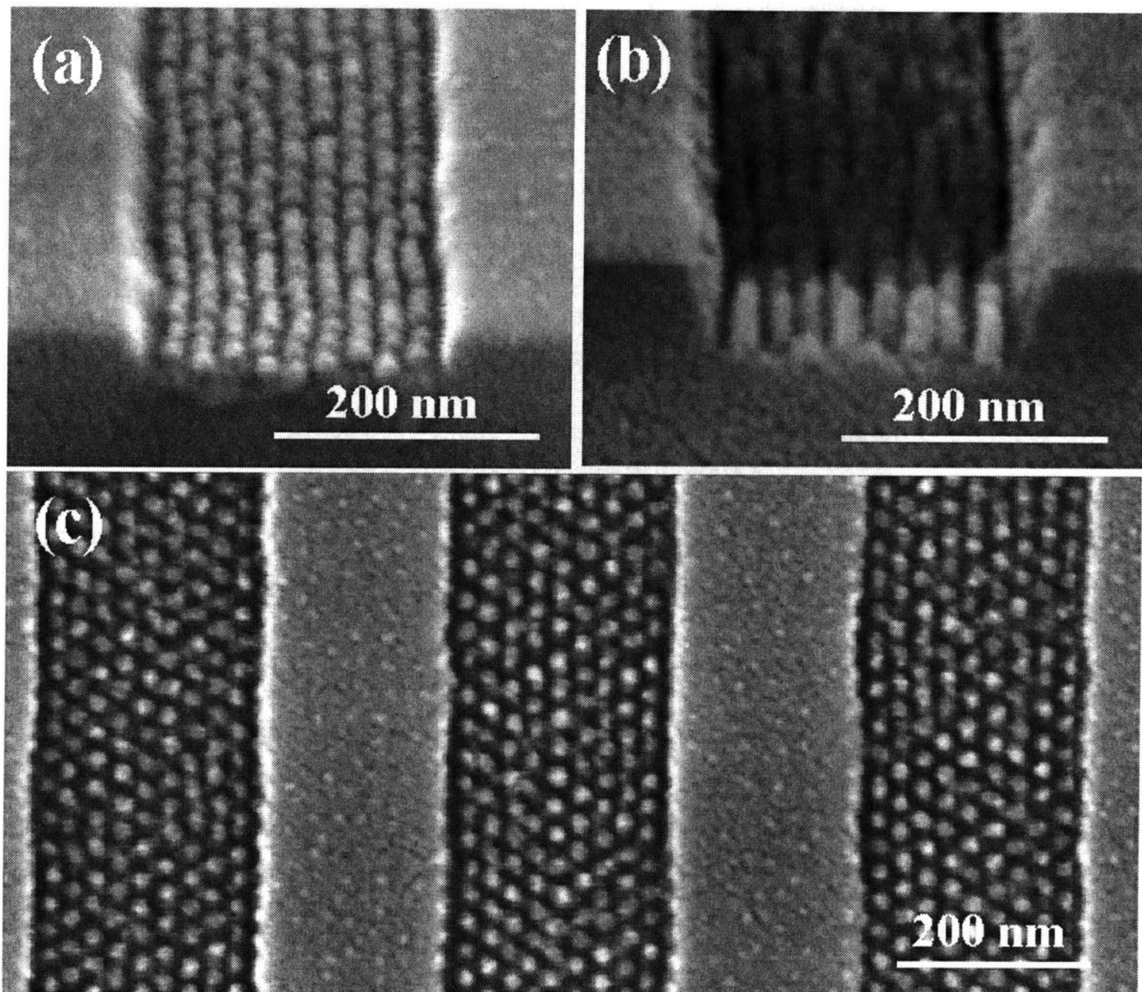

Figure 5.8. Pattern transfer from an ordered SF 32/10 polymer to form an array of ordered silica nanostructures. (a) side view of the PFS pattern in 240 nm wide grooves corresponding to figure 5.7c. (b) Side view and (c) plan view of the pattern after it has been transferred into an underlying silica layer by reactive ion etching. The silica posts in (c) have the same spatial organization as the originating PFS features of figure 5.7c, and aspect ratios exceeding 3.

for pattern transfer to other layers. The aspect ratio in this experiment can be further improved by tuning RIE conditions. This combination of graphoepitaxy and block copolymer lithography therefore provides a powerful method for precise placement of a variety of nanoparticles on a surface. Control of the nanostructure locations in two dimensions is expected to be possible by using a substrate patterned for instance with two sets of grooves oriented at 60° to each other.

In general, SF 91/21 and SF 32/10 follow the same trend. Preferential wetting of the substrate by a PFS layer drives the ordering of block copolymers from the edge of the groove to the center of the groove. Therefore, smaller grooves and higher diffusivity gives better ordering results. The diffusivity of SF 32/10 is 245 times higher than that of SF 91/21, and thus the diffusion length of SF 32/10 is around 15 times of that of SF 91/21. Consequently, better ordering results are found in SF 32/10 systems than in SF 91/21 systems. On the other hand, there is one main difference between these two systems. In the SF 32/10 system, well-ordered structures form in which all the close-packed rows are aligned within the grooves, provided the groove width is smaller than or comparable to the "grain size" of the block copolymer. In contrast, although SF 91/21 in the 300 nm wide groove and 240 nm wide groove is supposed to be well-ordered because the confinement width is smaller than the "grain size" which is around 320 nm, only partial ordering of SF 91/21 is achieved. This suggests that the accommodation of the polymer to an incommensurate substrate become more difficult for high molecular weight polymers, when confinement width is only 5 or 6 times the natural period of block copolymers. The high molecular weight polymer, SF 91/21, seems to be less likely to form ordered rows in the small grooves and tends to generate hemispheres on the edges to release the strain from incommensurate groove width. In addition, the effective diffusivity of the confined block copolymer film may further decrease because of the presence of ordered domains. Solid-like behaviors of liquids such as water and organic solvents have been found when the confinement decreases to 6 or 7 molecular layers. The effective viscosity of such confined liquids increases two to three orders of magnitude from the bulk viscosity [21]. Therefore, long-range order of block copolymer is easier to achieve in low molecular weight systems because of their high diffusivity and small domain spacing. Defects (or dislocations) in such systems can be generated efficiently to accommodate incommensurate confinement width.

In addition, the quality of ordering is affected by the geometry of the sidewalls. The block copolymer does not align well along a tapered sidewall (in which the sidewall angle of the grating is smaller than 40°) because these gratings do not provide sufficient lateral

confinement of the polymer. Alignment is also poor if the grating has undercut sidewalls. Therefore flat, vertical sidewalls are essential to achieve good ordering.

In summary, there are two criteria for templated self-assembly of block copolymers. First, one block should preferentially wet the sidewalls of the topographic features. Second, the width of the confining features should be comparable with the 'grain size' of the block copolymer thin film; however, ordering can fail if the confinement is too small and incommensurate with the natural period of block copolymers. This method is limited by the roughness of the sidewalls and also by the kinetics of the block copolymer. Combining topographic confinement with block copolymer lithographic methods will enable large area ordered functional dot arrays to be made for various applications.

5.4 Analysis of Ordered Block Copolymer Thin Films in the Grooves

Previous work on templating block copolymers shows that domain morphology, periodicity and ordering of self-assembled block copolymers can be influenced by substrate features [7-11], but to date there has not been direct observation of how block copolymers behave when templated by substrate features with characteristic sizes of a few times the natural domain period. In this section, we will first investigate the structures of ordered PS-PFS block copolymer in various topographical confinements and then demonstrate the effects of incommensurability and the correlations between defect and template feature.

Block copolymer SF 32/10 is employed in this section to form ordered block copolymer arrays inside the grooves. The grooves had a period of 400 nm, and their widths were varied between 200 nm and 270 nm. The block copolymer was spin-cast from a toluene solution to form a conformal coverage on the gratings, and then annealed at 140°C for typically 48 hours to obtain good ordering.

5.4.1 Topographically-induced Ordering of Block Copolymer Thin Films

From the analysis in section 5.2, the distance between first-nearest neighbors, or the averaged center-to-center spacing of the domains in a SF 32/10 thin film on the smooth substrate, is a_0 = 28.6 nm. The PFS spheres show short-range ordering with a 280 nm correlation length. Within the correlation length, the spheres are close-packed with a sixfold

symmetry. The spacing between parallel close-packed rows is $d_0 = \sqrt{3}a_0/2 = 24.8$ nm.

In contrast, figure 5.9a shows the domain morphology for the same polymer but now confined within a 233 nm wide shallow groove. 9 rows of spheres are oriented parallel to the sides of the groove to give a well-ordered, close-packed array. Also, a brush layer is found both at the bottom and sidewall of the silica grooves. The rows of spheres faithfully follow the variations in groove width, conforming to the sidewall variations. The number of rows of spheres is plotted vs. groove width in figure 5.9b. The groove width is expressed in terms of the corresponding number of ideal block copolymer periods. The number of ideal periods is calculated as (groove width minus the thickness of the brush layers) divided by the equilibrium row width d_0 (24.8 nm). The width is measured as an average over a groove

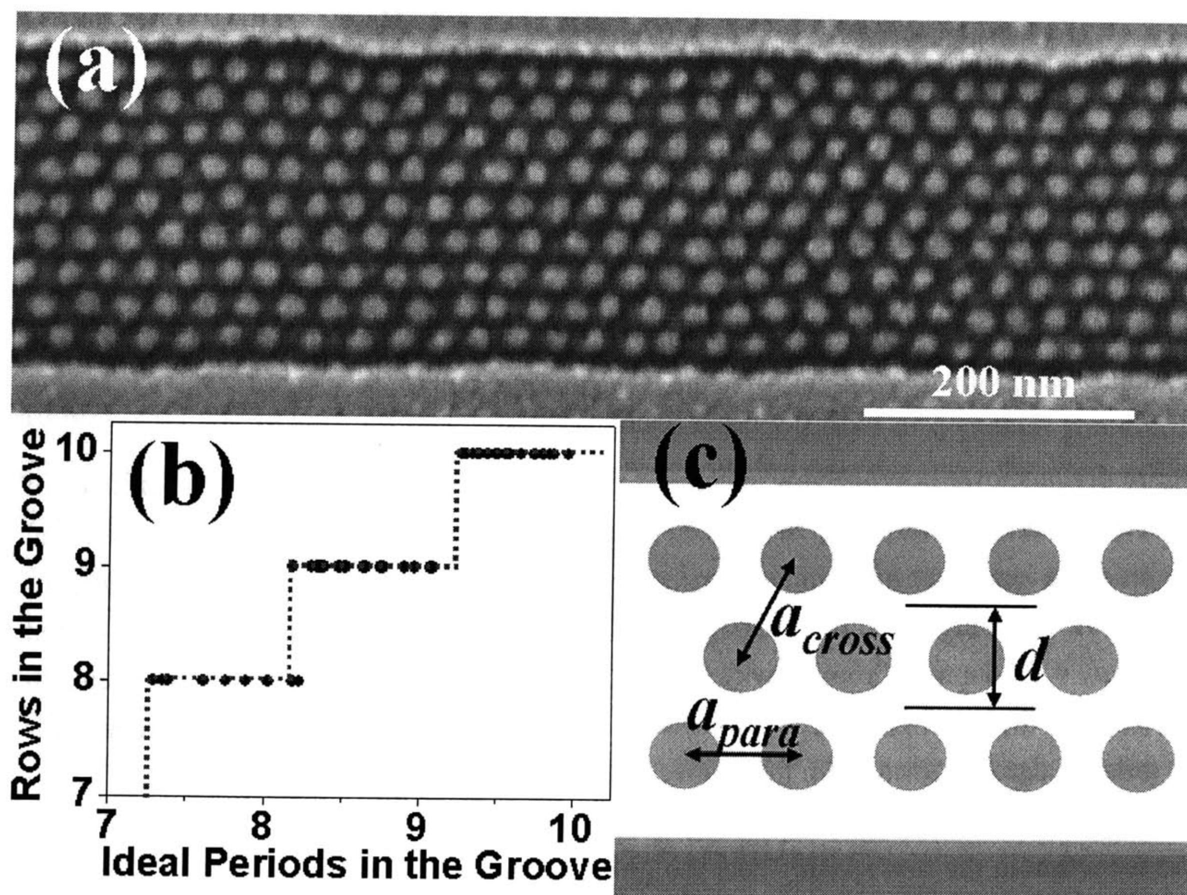

Figure 5.9 PS-PFS polymer confined within grooves in a silica substrate. (a) SEM image of a section of one groove, showing 9 rows of PFS spheres. (b) Schematic of the structure showing the row spacing d and the domain spacings a_{para} and a_{cross}. (c) The number of rows in the groove vs. groove width, showing the widths at which 8, 9 or 10 rows are stable. The groove width is expressed in terms of how many rows would ideally fit within the groove, calculated from the equilibrium row spacing.

length of 400 nm. The number of rows is quantized, for example, 9 rows are found in grooves with widths between 8.25 and 9.25 ideal periods, then it jumps to 10 rows for widths of 9.25 to 10.25 ideal periods. The periodicity of the block copolymer domain is compressed or expanded in order to comply with the groove width. When the groove width is incommensurate with the ideal period, it is apparently easier to accommodate an additional row such that the domain array is on average slightly compressed. This represents an interesting comparison with the vertical confinement of a lamellar system where, for instance, 9 parallel lamellae were found if the film thickness was held within the range from 8.5 to 9.5 periods [10,11]. The formation of a well ordered array for all the groove widths shown in figure 5.9b may also be compared with the case of hard spheres packed within grooves, where incommensurability between the sphere diameter and groove width leads to a loss in ordering [22].

The preferential wetting layers on the vertical sidewalls of the groove drives domain ordering and generates gradient in the domain spacing and domain size. First, the center-to-center spacing of the PFS spheres is no longer the same in the direction parallel to the groove (a_{para}) and in the direction across the groove (a_{cross}), shown in figure 5.9c. The averaged spacing a_{para} is 29.3 ± 0.3 nm, slightly larger than the averaged center-to-center spacing a_o found for the film on the smooth substrate. Second, the spacing d of rows parallel to the grooves is not uniform across the groove.

Figure 5.10a shows how the row spacing d varies across the groove width for grooves of different widths. Clearly, the row spacing is smaller near the sides of the grooves, and expands to a nearly uniform value near the center of the grooves. The rows at the center of the groove are compressed or expanded (the equilibrium spacing is indicated by the dotted line at d_o = 24.8 nm). Grooves with 8 or 10 rows also show this structural gradient. In comparison, the rows within a 466 nm-wide groove show the same reduced spacing near the groove edge, but away from the groove edge the row spacing approaches d_o.

The reduction in the row spacing near the groove edges is also associated with a change in the size of the PFS spheres. Notably, the two rows closest to the groove steps show a significant reduction in sphere to spheres at the center of the rows. From Figure 5.10b, the sphere area within the edge row is 75 % of that of the center row and the diameter is 85 % of that of the center row. By following the evolution of the domain structure with annealing time, we observe initially that small domains form and grow to a stable size over a few hours. Subsequent annealing leads to improvements in the ordering of the domains but not to changes in their size. This implies that the observed non-uniform domain sizes and row

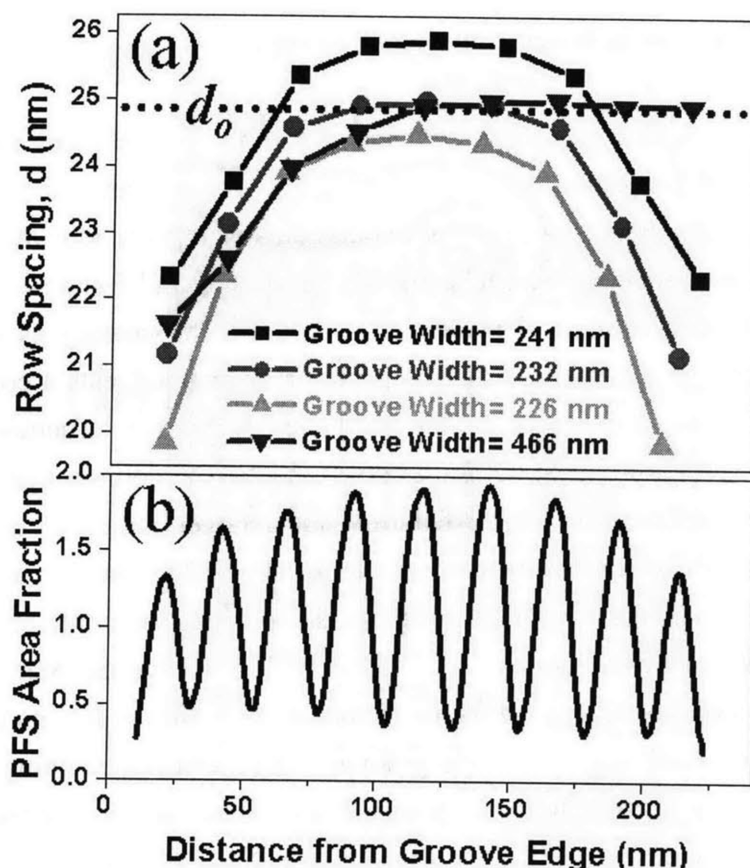

Figure 5.10 (a) The row spacing d for each of the rows of domains, in four different grooves. In each case the rows are more closely spaced near the groove edges. Three of the grooves, with widths 226, 232 and 241 nm, contain exactly 9 rows of domains. The fourth groove is much wider, but still shows a smaller row spacing near the edge. The dotted line shows the equilibrium row spacing d_o, on a smooth substrate. (b) The PFS domain area fraction across a 232 nm wide groove. The size of the PFS spheres is smaller near the edges of the groove and larger at the center of the groove.

spacings are in fact equilibrium states for the confined polymer, rather than being kinetically-trapped features. The size and spacing variation at the groove edges is related to the presence of the PFS wetting layers at the vertical sidewalls which decreases the concentration of PFS blocks available for domain formation in the vicinity of the step edge. This indicate that the surface chemistry of the confinement edges affects domain spacing over several periods, and can be used to induce gradients in the spacing and size of self-assembled structures. More uniform domain size and spacing may be expected when using a substrate preferentially wetted by the majority block. Therefore, by adjusting confinement width, surface chemistry of the confinement substrates, and molecular weight of block copolymers, a range of gradient features can be designed and fabricated with templated block copolymers, which is difficult to achieve with assembly of hard spheres.

5.4.2 Defect Formation in Block Copolymer Arrays

The topographical confinement described here not only controls the row spacing and feature dimensions of templated block copolymers, but also induces defect formation in the block copolymer arrays. Point defects (missing domains) and point edge dislocations can be purposefully generated in the close-packed arrays by the sidewall features of the grooves. A sharp edge feature such as a small protrusion causes a local vacancy as shown in figure 5.11a. This locally pins the position of the sphere array and suggests a convenient means for aligning the lateral position of the array. To pin the array structure, the radius of curvature of the edge feature must be in the same range as the domain size, less than about 50 nm in this polymer. A blunt edge feature with a larger radius of curvature usually perturbs the block copolymer arrangement as a long-range effect. In the presence of a blunt edge feature, the block copolymer array can either expand or contract to maintain an ordered arrangement, or dislocations can be generated to change the number of rows and accommodate the variation in groove width. Figure 5.11b shows polymers in three grooves along with a corresponding plot of their groove width vs. distance along the groove. In groove A, 9 ordered rows of spheres form regardless of the variation of the groove width, because the groove width remains within the ideal 8.25 – 9.25 periods (shown shaded), where a 9 row structure is stable. In groove B, as the width increases gradually from 8.15 to 8.8 ideal periods; the number of rows increases from 8 to 9 via the formation of a dislocation at the location where the groove width enters the shaded region (marked by an arrow). In groove C, the groove width decreases gradually, and the number of rows changes from 10 to 9 with the formation of a dislocation, at the position marked with the arrow. There are other places, e.g. the position marked with a star, at which the width of groove C briefly enters the 9-row region, but the system does not change to 9 rows, presumably because the strain energy associated with the formation of two additional dislocations would exceed the energy penalty from the nonequilibrium number of rows over such a short distance. This behavior is reminiscent of that seen in lattice-matched films growing on substrates, in which the film can grow epitaxially up to a certain critical thickness, at which point strain-relieving dislocations can nucleate [23].

In conclusion, topographical confinement is seen to template the formation of nanoscale domains in a PS-PFS block copolymer, leading to a quantized number of rows within a groove. Unlike the packing of hard spheres, the block copolymer system behaves elastically and can conform to various groove widths, leading to arrays with row spacing that depend on the commensurability between the groove and the natural polymer period. The variation in domain spacing across the groove, believed to be a result of interfacial interaction

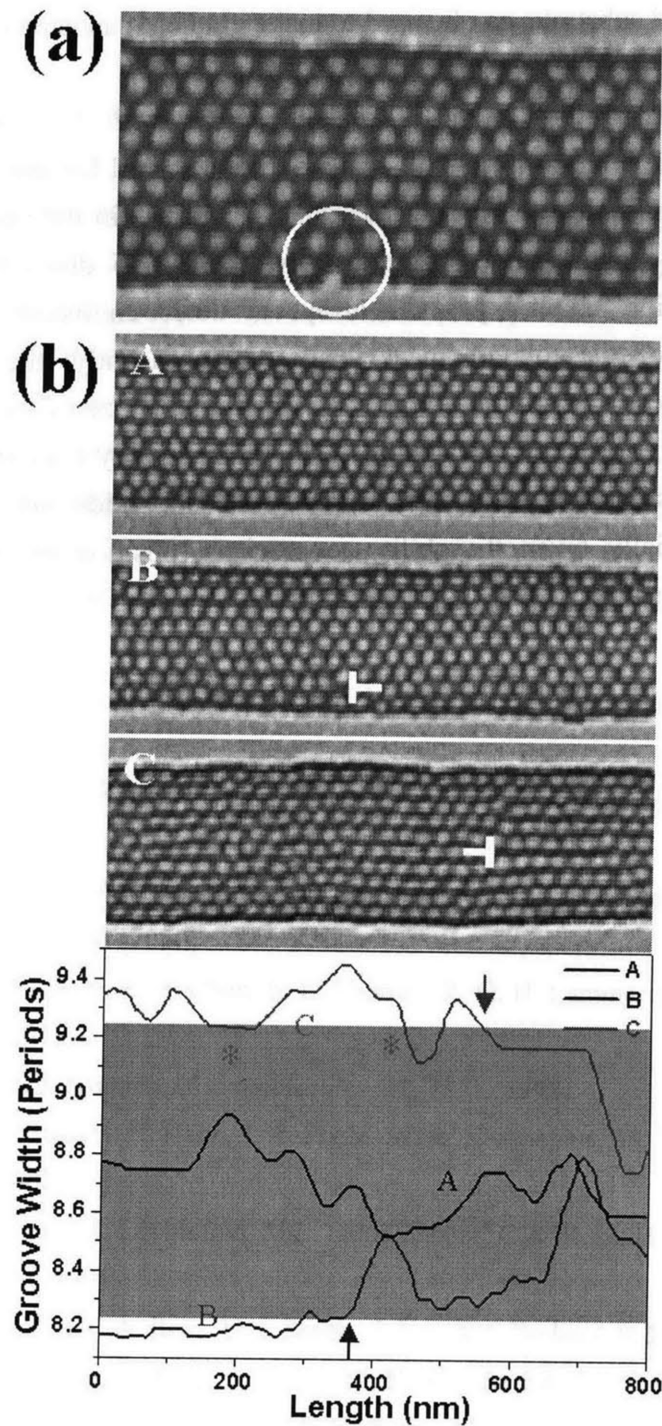

Figure 5.11. (a) A point defect (a missing domain) forms where there is a small, sharp protrusion at the groove edge, but the overall array is undisturbed. (b) Three grooves, A, B and C, showing how the number of domain rows adapts to changes in groove width. The lower plot shows groove width along the length of each groove. The shaded region represents the groove widths at which 9 rows form. In B and C, dislocations accompany a change in the number of rows, from 8 to 9 in B, and 10 to 9 in C, associated with changes result of interfacial interaction in groove width.

between polymer and substrate, can be used to make gradient nanostructures.

The rows of domains conform to the sidewall variations, with the rows exhibiting a high correlation to the sidewall profile. Small-scale, abrupt sidewall features can lead to defects such as vacancies (missing spheres), which can be used to pin the lateral position of the array, while longer-range changes in groove width lead to dislocation formation. By utilizing this behavior, tailored periodic arrays or defect-engineered structures can be created by design of the topographical features. Significantly, the requisite template periodicity is an order of magnitude larger than the domain size of the polymer, allowing control of the location of nanoscale features using considerably coarser substrate features. Such hierarchical structures can have applications in fields such as photonics or microfluidics, especially given the ability to precisely position engineered defects and periodicity in the structures [24,25].

Reference

1. M. Trau, N. Yao, E. kim, Y. Xia, G. M. Whitesides, I. A. Aksay, *Nature* **390**, 674 (1997)
2. M. Boltau, S. Walheim, J. Mlynek, G. Krausch, U. Steiner, *Nature* **391,** 877 (1998)
3. Y. Yin, Y. Lu, B. Gates, and Y. Xia, *J. Am. Chem. Soc.* **123,** 8718 (2001)
4. H. I. Smith, M. W. Geis, C.V. Thompson, H.A. Atwater, *J. Cryst. Growth* **63**, 527 (1983)
5. T. Kobayashi and K. Takagi, *Appl. Phys. Letts.* **45** 44 (1984)
6. D. C. Flanders, D. C. Shaver, H. I. Smith, *Appl. Phys. Lett.* **32**, 597 (1978)
7. R. A. Segalman, H. Yokoyama, E. J. Kramer, *Adv. Mater.* **13**, 1152 (2001)
8. L. Rockford, Y. Liu, P. Mansky and T. P. Russell, *Phys. Rev. Lett.* **82**, 2602 (1999); L. Rockford, S. G. J. Mochrie, T. P. Russell, *Macromolecules* **34**, 1487 (2001)
9. X. M. Yang, R. D. Peters, P .F. Nealey, H. H, Solak and F. Cerrina, *Macromolecules* **33**, 9575 (2000); R. D. Peters, X. M. Yang, Q. Wang, J. J. de Pablo, P .F. Nealey, *J. Vac. Sci. Technol. B* **18,** 3530 (2000)
10. P. Lambooy, T. P. Russell, G. J. Kellogg, A. M. Mayes, P. D. Gallagher and S. K. Satija, *Phys. Rev. Lett.* **72**, 2899 (1994)
11. N. Koneripalli, N. Singh, R. Levicky, F.S. Bates, P. D. Gallagher and S. K. Satija, *Macromolec.* **28**, 2897 (1995)
12. R. G. H. Lammertink, M. A. Hempenius, J. E. van den Enk, V. Z. H. Chan, E. L. Thomas, G. J. Vancso, *Adv. Mater.* **12**, 98 (2000)
13. J. Y. Cheng, C. A. Ross, V. Z. H. Chan, E. L. Thomas, R. G. H. Lammertink, G. J. Vancso, *Adv. Mater.* **13**, 1174 (2001)
14. H. Yokoyama and E. J. Kramer, *Macromolecules*, **31**, 7871 (1998)
15. H. B. Eitouni, N. P. Balsara, H. Hahn, J. A. Pople, M. A. Hempenius, **35**, 7765, *Macromolecules* (2002)
16. M. Farhoud, J. Ferrera, A.J. Lochtefeld, M.L. Schattenburg, C.A. Ross, H. I. Smith, *J. Vac. Sci. Technol.* B **17**, 3182 (1999)
17. M. E. Walsh, Y. W. Hao, C.A. Ross, H. I. Smith, *J. Vac. Sci. Technol.* B **18**, 3539 (2000)
18. Y. Liu, W. Zhao, X. Zhang, A. King, A. Singh, M. H. Rafailovich, J. Sokolov, K. H. Dai, E. J. Kramer, S. A. Schwarz, O. Gebizlioglu and S. K. Sinha, *Macromolecules* **27**, 4000 (1994)
19. H. Yokoyama, T. E. Mates, E. J. Kramer, *Macromolecules* **33**, 1888 (2000)
20. L. H. Radzilowski, B. L. Carvalho, E. L. Thomas, *J. Poly. Sci. Poly. Phys.* **34**, 3081 (1996)
21. J. Klein, E. Kumachev, *Science,* **269**, 816 (1995); J. Gao, W. D. Luedtke, U. Landman, *Phys. Rev. Lett.* **79**, 705 (1997)
22. E. Kumacheva, R. K. Golding, M. Allard, E. H. Sargent, *Adv. Mater.* **14**, 221 (2002)
23. J.W. Matthews, *Epitaxial Growth*, edited by J. W. Matthews, Academic, New York (1975)

24. P. Yang, T. Deng, D. Zhao, P. Feng, D. Pine, B. F. Chmelka, G. M. Whitesides, G. D. Stucky, *Science*, **282**, 2244 (1998); H. Fan, Y. F. Lu, A. Stump, S. T. Reed, T. Baer, R. Schunk, V. Perez-Luna, G. P. Lopez, C. J. Brinker, *Nature* **405,** 56 (2000)
25. T.A. Taton and D.J Norris, *Nature* **416** 685 (2002); W. Lee, S. A. Pruzinsky and P. V. Braun, *Adv. Mater.* **14**, 271 (2002)

Chapter 6

CONCLUSIONS AND FUTURE WORKS

6.1 Conclusions

It is widely assumed that self-assembly will be the basis of an extensive range of applications in nanotechnology. This view is driven in part by the perception that self-assembly is dominant in living systems and achieves amazingly sophisticated structures. There are two fundamental challenges in utilizing self-organizing materials: how to develop functional structures from the self-assembled system and how to control the self-assembled system to meet the requirements for the applications. In this thesis, we tried to respond to these challenges in one particular case with our attempts to use self-assembled block copolymers to fabricate nanomagnet arrays.

The fabrication of nanoscale magnetic dot arrays has attracted considerable interest for possible applications in high-density magnetic data storage. Single-domain magnetic particles are ideal for applications such as patterned recording media, in which each particle stores one bit according to its magnetization direction. In addition to conventional lithographic methods, block copolymer thin films, which microphase-separate into a monolayer of nanoscale periodic domains, provide an alternative approach. Thin films of polystyrene-b-polyferrocenyldimethylsilane (PS-PFS) have been used as the lithographic templates to define the dimension and period of the nanostructures. Close-packed magnetic dot arrays with period of 56 nm and diameter of 35 nm were made from sphere-morphology PS-PFS (SF 91/21). Four RIE steps and one ion-beam etching step were employed to pattern magnetic thin films under Silica/W mask layers. This process can be applied very generally to pattern a variety of thin-film materials into high-density dot arrays. In addition, particle sizes and spacings can be controlled through the choice of the block copolymer template and etching conditions.

A series of single layer dots of Co, NiFe, and two layer dots of CoFe/Cu/NiFe pseudo-spin-valve were successfully made from PS-PFS templates. All dots are single domain particles. The hysteresis loops and time dependent coercivities were measured and compared to quantify the magnetic switching behavior of these arrays. As a result of in-plane shape anisotropy, the coercivity increases as the thickness of the dots increases. In addition, strong magnetostatic interaction between the dots was indicated by the fact that

the switching volumes are larger than the physical volumes of the dots. The patterned PSV dots show appreciable magnetoresistance and strong inter-particle and intra-particle magnetostatic interaction.

The self-assembly process is simple and low cost, however, the block copolymers typically have uncontrolled defects and lack long-range order. A topographically patterned substrate was used to guide the nanostructures in a subsequently deposited block copolymer film. Lateral dimension of the pattern substrates and interfacial interactions are key factors in the ordering mechanism. Well-ordered structures of block copolymer can be achieved under proper confinement condition. The number of rows of ordered block copolymers that forms within a groove is determined by the width of the groove. Small-scale, abrupt sidewall features can lead to defects such as missing spheres, which can be used to pin the lateral position of the array, while longer-range changes in groove width lead to dislocation formation. By utilizing this behavior, the position of polymer microdomains and dislocations can be purposefully controlled by the design of the topographical guiding features. Combining bottom-up self-organizing materials and top-down lithographic methods would allow self-assembled nanostructures to be fabricated in precise positions on a substrate. Such hierarchical structures can have applications in fields such as photonics or microfluidics, especially given the ability to precisely position engineered defects in the structures.

6.2 Future Works

Combing bottom-up self-assembled materials and top-down lithography process provides great opportunities not only to fabricate long-range ordered structures but also to explore novel confinement-induced phenomena. For example, confinement induces a liquid-to-solid transition in water or organic solvent when the confinement width of 6 or 7 times of the molecule dimension [1]. Both the packing and symmetry of colloid assemblies vary as the confinement width and confinement shape [2]. The switching properties of liquid crystals can be tuned by the substrate profile [3]. Block copolymers can be made with various kinds of material combinations and can be templated in various ways, therefore there are rich opportunities to study and compare the behavior of narrowly confined block copolymers with other self-assembled systems. With designed templates made using e-beam lithography, and well-controlled line-width roughness, it is possible to reveal details of the

defect generation and defect control through the topographic features. In addition, chemically heterogeneous substrates and soft-lithography methods [4] can be used as templates to guide the positions of the nanostructures of block copolymers.

Polystyrene-b-polyferrocenyldimethylsilane (PS-PFS) is very useful for structural characterization because it provides good etching contrast under an oxygen plasma and enables direct observation of the precise position and size of microdomains in the block copolymer thin films. PS-PFS combined with lithographically patterned templates offers a simple and clean model system to study the confinement behavior of block copolymers. It would be even better if PFS could be substituted with an amorphous ferrocenylsilane instead of a semicrystalline one, for crystallization of the PFS block may introduce additional complexity into the system.

For patterned media applications, it is required to have ordered uniaxial magnetic dot arrays. Future works will involve patterning a high-K perpendicular magnetic thin film media such as Co/Pt multilayer or Ti alloy-seeded CoCrPt layer. Templated block copolymers could provide the ordered nanostructures and servo marks for patterned media. The magnetostatic interaction between the particles can be tuned by the size and spacing of particle arrays by addition of homopolymers or changing the molar mass of the block copolymer templates. Moreover, there are many potential applications of block copolymers beyond high-density magnetic data storage, for example, integration of ordered block copolymers with silicon system as pillar arrays for vertical transistors or field emission display may be feasible in the future [5].

Reference

1. J. Klein, E. Kumachev, *Science,* **269**, 816 (1995) ; J. Gao, W. D. Luedtke, U. Landman, *Phys. Rev. Lett.* **79**, 705 (1997)
2. Y.-H. Ye, S. Badilescu, V. Truong, P. Rochon, A. Natansohn, *Appl. Phys. Lett.* **79**, 872 (2001); Y. Yin, Y. Lu, B.Gates, and Y. Xia, *J. Am. Chem. Soc.* **123,** 8718 (2001); D. K. Yi, E. Seo, D. Kim, *Appl. Phys. Lett.* **80**, 225 (2002); E. Kumacheva, R. K. Golding, M. Allard, E. H. Sargent, *Adv. Mater.* **14**, 221 (2002); I. Lee, H. P. Zheng, M. F. Rubner, P. T. Hammond, *Adv. Mater.* **14**, 572 (2002); H. P. Zheng, I. Lee, M. F. Rubner, P. T. Hammond, *Adv. Mater.* **14**, 569 (2002)
3. G. P. Bryan-Brown, C. V. Brown, I. C. Sage, V. C. Hui, *Nature*, **392**,365 (1998); P. Patricio, M. M. Telo da Gama, and S. Dietrich, *Phys. Rev. Lett.* **88**, 245502 (2002)
4. T. Deng, Y. H. Ha, J .Y. Cheng, C. A. Ross, E. L. Thomas, *Langmuir* **18**, 6719 (2002)
5. C. T. Black, K. W. Guarini,K. R. Milkove, S. M. Baker, T. P. Russell, M. T. Tuominene, *Appl. Phys. Lett.* **79**, 409 (2001); K. W. Guarini, C. T. Black, K. R. Milkove, R. L. Sandstrom, *J. Vac. Sci. Technol. B* **19**, 2784 (2001); K. W. Guarini, C. T. Black, Y. Zhang, H. Kim, E. M. Sikorski, I. V. Babich, *J. Vac. Sci. Technol. B* **20**, 2788 (2002)

Publications

1. Cheng JY, Jung W, Ross CA "Properties of magnetic dot arrays using block copolymer lithography" in preparation
2. Cheng JY, Ross CA, Thomas EL, Smith HI and Vancso GJ, "Templated self-assembly of block copolymers: effects of substrate topography" submitted
3. Cheng JY, Ross CA, Thomas EL, Smith HI and Vancso GJ, "Fabrication of nanostructures with long-range Order using block copolymer lithography" *Appl. Phys. Lett.* **81**, 3657 (2002)
4. Cheng JY, Ross CA, Thomas EL, Smith HI and Vancso GJ, "Magnetic properties of large-area particle arrays made by block copolymer lithography" *IEEE Trans. Magn.* **38**, 2541 (2002)
5. Deng T, Ha YH, Cheng JY, Ross CA, Thomas EL, et al. "Micropatterning of block copolymer solutions" *Langmuir* **18**, 6719 (2002)
6. Ross CA, Haratani S, Castano FJ, Hao Y, Hwang M, Shima M, Cheng JY, Vogeli B, Farhoud M, Walsh M, Smith HI, "Magnetic behavior of lithographically patterned particle arrays", *J. Appl. Phys.* **91**, 6848 (2002)
7. Ross CA, Hwang M, Shima M., Cheng JY et al. "Magnetic behavior of electrodeposited cylinder arrays" *Phys. Rev. B* **65**, 144417, (2002)
8. Cheng JY, Ross CA, Chan VZH, et al. "Formation of a cobalt magnetic dot array via block copolymer lithography" *Adv. Mater.* **13**, 1174 (2001)
9. Park C, Cheng JY, Fasolka MJ, et al. "Double textured cylindrical block copolymer domains via directional solidification on a topographically patterned substrate" *Appl. Phys. Lett.* **79**, 848 (2001)
10. Cheng YR, Lin HP, Mou CY "Control of mesostructure and morphology of surfactant-templated silica in a mixed surfactant system" *Phys. Chem. Chem. Phys.* **1**, 5051 (1999)
11. Lin HP, Cheng YR, Liu SB, et al. "The effect of alkan-1-ols addition on the structural ordering and morphology of mesoporous silicate MCM-41" *J. Mater. Chem.* **9**, 1197 (1999)
12. Lin HP, Cheng YR, Lin CR, et al. "The synthesis and application of the mesoporous molecular sieves MCM-41 - a review" *J Chin. Chem. Soc.* **46**, 495-507 (1999)
13. Lin HP, Cheng YR, Mou CY " Hierarchical order in hollow spheres of mesoporous silicates" *Chem. Mater.* **10**, 3772 (1998)
14. Chiang CC, Cheng JY, Cheng YR, et al. "Hole-burning structure and mechanism of acridine and aminoacridines doped in polyvinyl alcohol films" *Mol. Cryst. Liq. Cryst.* A **291**, 175 (1996)